

Experimental study of solar drying of Tunisian phosphate: in open sun, under greenhouse and by a parabolic concentrator

Abdelhamid Fadhel^{a,b}, Kais Charfi^b, Hassen Jallouli^b and Sami Kooli^a

^a*Research and Technology Center of Energy, Thermal Processes Laboratory, Hammam Lif, B.P. 95, 2050 Tunis, Tunisia*

^b*Gafsa Faculty of Sciences, Physics Department, Gafsa University, Sidi Ahmed Zarroug, Gafsa 2112, Tunisia*
fad_ham@yahoo.fr

Received date: February 29, 2016; revised date: April 04, 2016; accepted date: April 22, 2016

Abstract

This work is part of operating a parabolic concentrator for drying the phosphate. This study is to analyzing the drying of Tunisian phosphate by three separate solar processes. Two experimental devices have been implemented. Three drying kinetics were set up by a parabolic concentrator, under greenhouse and in open sun, respectively. Nine thin-layer drying models were fitted to the experimental data to select a suitable drying equation. The Midilli model was found to best describe the drying behavior of phosphate for open sun, parabolic concentrator and greenhouse drying. These tests show that the drying by the parabolic concentrator gives results whose perspectives are satisfactory compared with the drying in the open sun or under greenhouses.

Keywords: open sun drying; greenhouse drying; drying kinetics; parabolic concentrator; phosphate.

1. Introduction

During recent decades, the demand for energy in its various forms has been increasing, for the development and growth of industrial activity and demand for comfort in daily life. Solar energy is transmitted by the sun in the form of light and heat [1]. It is virtually inexhaustible on the scale of human time.

Given its position, Tunisia has a significant potential of solar energy. This favorable opportunity allows Tunisia to be a pioneer in the use of solar energy in the context of energy conservation strategy and the government management programs. Indeed, essentially the southern regions of Tunisia are equipped of huge solar energy opportunity, put to use, could participate in a meaningful way to sustainable development and provide handy solutions to socioeconomic problems in these regions. In Gafsa, where the relative humidity is less than 69% during most of the year, wherein the duration of sunshine is 3000 hours/year and where the global solar radiation

averages 5.4kWh/m²/day, the use of solar energy is a very important activity [2].

The exploitation of phosphates is fundamentally centered on the production of fertilizer and phosphoric acid which represents the most important economic targets [3]. Phosphate is a high demand material in international trade. The phosphates sector occupies an important place in the Tunisian economy, both in the employment and in the trade balance. Globally, the Tunisian phosphate industry occupies the 5th place among the largest international operators in this activity [4]. Generally, the phosphates can undergo special treatments including grinding to reduce its particle sizes.

Production of marketable phosphate in Tunisia could exceed 8 million tons in 2010. Tunisia is the second country in the world to develop a large percentage of its production of phosphate (nearly 80%). This activity is more than a century for the extraction to phosphate by the Gafsa Phosphate Company (CPG) and more than fifty years in the area of its valuation in various mineral fertilizers by the Tunisian Chemical Group (GCT). CPG currently

operates seven open pits and one undergrounds mine [4].

Nomenclature

a, b, c,	empirical constants in the drying models
g, h	solar radiation outside the greenhouse, (W/m ²)
Ge	solar radiation inside the greenhouse, (W/m ²)
Gi	empirical constants in the drying models
k, k ₁ , k ₂	mass of the material, (kg)
m	mass of the material water, (kg)
m _w	dry matter of the material, (kg)
m _d	number constants
n	number of observations
N	correlation coefficient
R ²	relative humidity of the air around the material (inside greenhouse), (%)
RHi	relative humidity of ambient air (outside greenhouse), (%)
RHe	root mean square error
RMSE	moisture content, (dry basis)
X	water content of phosphate placed at the focus of parabolic concentrator, (dry basis)
Xc	phosphate water content placed in open sun, (dry basis)
Xe	water content of phosphate placed inside the greenhouse, (dry basis)
Xi	initial moisture content, (dry basis)
X ₀	equilibrium moisture content, (dry basis)
X _{eq}	moisture ratio
XR	moisture ratio of phosphate placed at the focus of parabolic concentrator
XRc	moisture ratio of phosphate placed in open sun
XR _e	

XRi	moisture ratio of phosphate placed inside the greenhouse
XR _{exp}	experimental moisture ratio
XR _{pre}	predicted moisture ratio
t	time, (hr)
Tac	air temperature at the focus of parabolic concentrator, (°C)
Tae	ambient air temperature (outside the greenhouse), (°C)
Tai	air temperature inside the greenhouse, (°C)
Tp	phosphate temperature, (°C)
Tpc	phosphate temperature placed at the focus of parabolic concentrator, (°C)
Tpe	phosphate temperature in open sun, (°C)
Tpi	phosphate temperature inside the greenhouse, (°C)
Vae	ambient air velocity (outside the greenhouse), (m/s)
Vai	air velocity inside the greenhouse, (m/s)

Subscripts

Av	the average value
Max	the maximum value
Min	the minimum value
f	final

Greek symbol

χ ²	chi-square
----------------	------------

Note: 1US Dollar=2.031 TD.

Drying is economically expensive, given the price of energy highly elevated. For this reason, consulting energy audit reports provided by the National Renewable Energy Agency (ANER), a study of the energy consumption of drying in the field of industry

in Tunisia has allowed us to determine the weight of drying which is estimated to 266.578 kTep (1Tep = 42 10³J) primary energy or 5.92% of total energy consumption in Tunisia and 18.5% of energy consumption in the industrial sector [5]. It should be noted, first, that this study is carried out on a total

equal to 114 industries in various fields of activities. Indeed this number is according to statistics from the ANER over 90% of industrial energy consumption. The total energy consumption of mining is equal to 180.8 kTep/year; the consumption of drying in this sector is estimated at 66.896 kTep/year representing 37% of the total consumption [5].

Annually, CPG dried 1.2 million tones of phosphate, and consumes for such an operation around 17 kTep of fuel per year. This consumption weighs more and more heavily on the company's operating expenses, with an annual cost exceeding 4millionTD/year, to which must be added at least 1millionTD maintenance costs, maintenance and other expenses caused by the use of driers [6].

Faced to this serious energy situation, CPG launched in 2007 a solar drying project in the open air in the three industrial sites in the CPG, namely El M'dhila, Metlaoui and Moularès. From an initial cost of 3.3millionTD (mainly rolling stock), this project was started with semi-industrial test step during 2007, covering 25% for the production of dried phosphates, and in 2008 the project began the industrial phase with the solar treatment 60% of production (720 000 tons). In 2009, the solar drying of phosphates reached a significant rate with treating 70% of the production of dried phosphates (840 000 tons). In the coming years, the proportions to be processed in open sun will remain exactly in the same level [6]. However, there are several opportunities to dry phosphate using solar energy; there may be mentioned drying under greenhouse, drying by a parabolic concentrator and the traditional drying where the phosphate is exposed to sun and wind ... etc.

This experimental study is devoted to the determination of phosphate drying kinetics in uncontrollable conditions: outdoor, under greenhouse and by a parabolic concentrator. All three drying processes used allow enjoying free energy from the sun and constitute an economically profitable operation. It is therefore of great interest to study the various aspects of these drying processes and identify the most appropriate method.

2. Materials and methods

2.1. Sample preparation

During tests under greenhouse, outdoor and by the parabolic concentrator, we are placed in the same external conditions. In this study the phosphate used is brought from the launderette IV (CPG) in Metlaoui (a sector amongst of the five production of the phosphate

of the mining region of Gafsa in southern Tunisia). The wet phosphate is introduced into a parallelepiped block in plastic. Then, one obtains a phosphate sample of 10 mm thick, length 130 mm and width 65 mm. Subsequently, this sample is placed on a polystyrene plate covered with aluminum foil (Fig. 1 (a)). To measure the material temperature, three type K thermocouples were used. The phosphate temperature being obtained by averaging the temperatures of these three thermocouples, which are positioned in different places in the material (Figs. 1 (b) and 1 (c)).



Figure 1. Sample preparation: (a) the phosphate in the block, (b) the phosphate sample under greenhouse, (c) the phosphate sample in open sun

2.2. Experimental devices

In this subsection we will describe the various devices used to study experimentally the phosphates drying under greenhouse, by the parabolic concentrator and in open sun.

Fig. 2 (a) illustrates the entire experimental device used for drying phosphate under greenhouse and outdoors. This device consists mainly of a balance inserted into a wooden box. For tests in the open air, the tray covered by aluminum foil containing the phosphate was surrounded by these four sides by a bell formed of four pieces of thin ordinary glass, to avoid deterioration caused by excessive air currents (Fig. 2- (a)). The small greenhouse used for drying the phosphate is built in our Department in the Gafsa Faculty of Sciences, with ground surface of 2.25 m² (its base is a square of 1.5 m side), height 1,8 m from its base to its summit and its axis is parallel to the east-west direction (Fig. 2 (c)). To protect it the prevailing wind (North-West), we have installed this greenhouse in an internal space of the Faculty of Sciences of Gafsa. The greenhouse is coated with a plastic blanket (low density polyethylene of thick 180 μm) (Fig. 3 (b)).

The parabolic concentrator was built in the Physics Department of the Gafsa Faculty of Sciences operating with a manual tracking system in two axes vertical and horizontal. Both axes can track the sun in its racing

and also to maximize the concentrated solar radiation to the absorber. It has a rigid support posing on the ground. It consists of two parts, namely: the reflector and the receiver (Fig. 3- (a)). The opening of this solar concentrator is $\phi = 2.80$ m with a total surface (reflector) is 2.92 m². It is constituted by 1825 mirrors (the thickness of a mirror being 3 mm with surface is limited to $4\text{cm} \times 4\text{cm}$) which are bonded with silicone on the entire parabolic surface (Figure 3- (a)). All rays issued by sun is reflected by the mirrors and gathered in one point called the focus (Receiver: holder-sample of phosphate of $h = 60$ cm height from the center of the parabolic solar concentrator) for supporting the high temperature and thus the heat that will be used thereafter for drying the phosphate. To analyze and identify the receiver position, we have displaced a cardboard in different positions until the appearance of a flame that burns the card after 5 min, indicating at the focus.

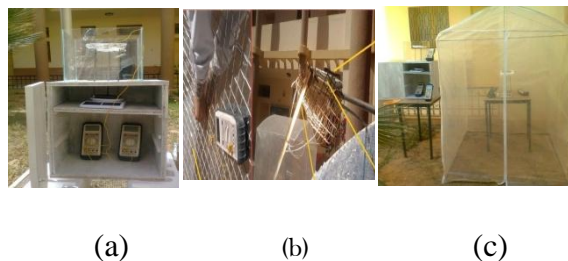


Figure 2. Phosphate drying: (a) in the open air, (b) by a parabolic concentrator (c) under greenhouse.

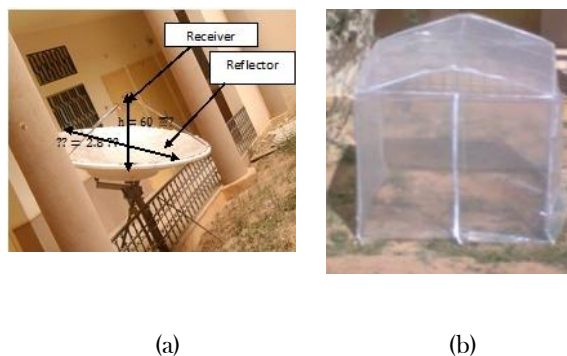


Figure 3. Experimental device: (a) parabolic concentrator (b) Greenhouse

2. 3. Drying procedure and data acquisition

In the drying tests, the drying parameters (incident radiation, air velocity, humidity and air temperature) are continuously variable in time (variable conditions). The incident radiation is measured using a calibrated photovoltaic solar panel with a pyranometer of type

Kipp-Zonen (Model CM3) and $\pm 5\%$ accuracy. The air speed is measured by an anemometer (TESTO 435) for the velocity measurements in the range of $0-15\text{m/s}$, with $\pm 0.1\text{ms}^{-1}$ accuracy. The relative humidity and the air temperature were measured by a sensor HMP35C (Vaisala Model HMP35C). The HMP35C errors are $\pm 0.1^\circ\text{C}$ of temperature and $\pm 3\%$ of humidity. The thermocouples were connected to the multimeters. The measurement error is $\pm 0.2^\circ\text{C}$. The sample mass during time is measured by a scale of capacity 7000 g and precision of ± 0.1 g. The sensitiveness was obtained from catalogs of the instruments.

The material temperature on the tray, air temperature, relative humidity of the air above the material surface and the sample mass were measured at intervals of 20 min during the experiments. The recordings were made manually.

Once the drying operation is complete, the sample was placed in an oven at 120°C for 12 hours, and then weighed to determine the corresponding dry matter (m).

3. Mathematical modeling of drying curves

Phosphates water content was estimated on dry basis. Dry matter value of the samples was calculated. The material water content at different drying stages was then expressed according to the following relation:

$$X = \frac{m_e}{m_s} = \frac{m - m_s}{m_s} \tag{1}$$

Where m_e is the mass of the material water, X the water content in dry basis, m the mass of the material and m_s the corresponding dry matter.

The moisture ratios (XR) of Phosphates during drying were calculated using the following equation:

$$XR = \frac{X - X_{eq}}{X_0 - X_{eq}} \tag{2}$$

Where X , X_0 and X_{eq} (kg water/kg dry matter) are, respectively, the moisture content at a specific time, the initial moisture content, the equilibrium moisture content.

The moisture ratio XR is simplified by some investigators [7- 9] to X/X_0 because the equilibrium moisture X_{eq} content is significantly less than the initial moisture content X_0 . In this case, Eq. (2) becomes:

$$XR = \frac{X}{X_0} = \frac{m - m_s}{m_0 - m_s} \tag{3}$$

Where m_0 is the water mass of the initial material.

For mathematical modelling, the thin layer drying equations in Table 1 were tested to select the best model for describing the drying curve equation of phosphate during drying by the parabolic concentrator, under greenhouse and in open sun. Regression analysis was performed using the Statistica computer program. The correlation coefficient (R^2) was the primary criterion for selecting the best equation to describe the drying curve equation. In addition to R^2 , the reduced χ^2 as the mean square of the deviations between the experimental and calculated values for the models and the root mean square error analysis (RMSE) were used to determine the goodness of the fit. Higher values of R^2 and lower

values of χ^2 and RMSE indicate better goodness of fit [8- 14]. These can be calculated as:

$$R^2 = 1 - \frac{\sum_{i=1}^N (XR_{exp,i} - XR_{pre,i})^2}{\sum_{i=1}^N (\overline{XR}_{exp,i} - XR_{pre,i})^2} \tag{4}$$

$$\chi^2 = \frac{\sum_{i=1}^N (XR_{exp,i} - XR_{pre,i})^2}{N-n} \tag{5}$$

$$RMSE = \left[\frac{1}{N} \sum_{i=1}^N (XR_{exp,i} - XR_{pre,i})^2 \right]^{\frac{1}{2}} \tag{6}$$

Where $XR_{exp,i}$ is the i th experimental moisture ratio, $XR_{pre,i}$ is the i th predicted moisture ratio, $\overline{XR}_{exp,i}$ the mean experimental moisture ratio, N the number of observations, and n the number of constants in each regression model.

Table 1. Mathematical models widely used to describe drying kinetics

Model no.	Model name	Model	Referen ce
1	Newton	$XR = \exp(-kt)$	[15]
2	Henderson and Pabis	$XR = a \exp(-kt)$	[16]
3	Page	$XR = \exp(-kt^n)$	[17]
4	Logarithmic	$XR = a \exp(-kt) + c$	[18]
5	Modified Page	$XR = \exp(-(kt)^n)$	[19]
6	Midilli et al.	$XR = a \exp(-kt^n) + bt$	[20]
7	Two-term	$XR = a \exp(-k_1t) + b \exp(-k_2t)$	[21]
8	Wang and Singh	$XR = 1 + at + bt^2$	[22]
9	Modified Henderson and Pabis	$XR = a \exp(-kt) + b \exp(-gt) + c \exp(-ht)$	[23]

4. Results and discussion

4.1. Drying conditions

The atmospheric conditions (solar radiation, ambient temperature, ambient humidity and wind speed) are factors that can drive and steer outstandingly the drying operation. The drying tests of phosphate in the open sun, by the parabolic concentrator and under greenhouse are realized jointly under the same weather conditions, on the same time of 04/29/2014.

4.1.1. Solar radiation

Climatic conditions during this day of 04/29/2014 are characterized by a perfect sunshine (Fig. 4). Solar radiation in open air reaches its maximum about 1050 W/m^2 at midday. However, the solar radiation under

the greenhouse is less intense than that outside. We recorded 20% reduction of radiation penetrating in the greenhouse. The maximum solar radiation reaches under greenhouse was about 850 W/m^2 .

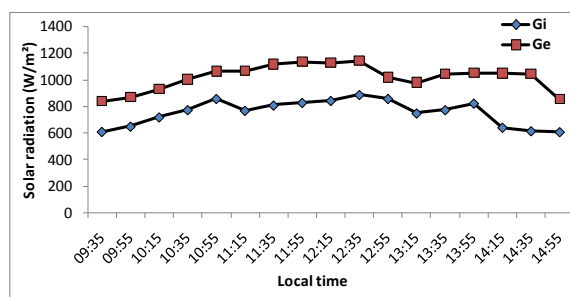


Figure 4. Evolution the outside solar radiation (Ge) and under greenhouse (Gi) versus time of 04/29/2014

4.1.2. Relative humidity

The relative humidity of the outside air and under the greenhouse are approximately the same, it is varied between 15.1 and 33.4% (Fig. 5). They are slightly reduced during time. Yet, the relative humidity of air under greenhouse is imperceptibly lower than outside. We recorded 7% decline in the relative humidity of the air in the greenhouse compared to outside.

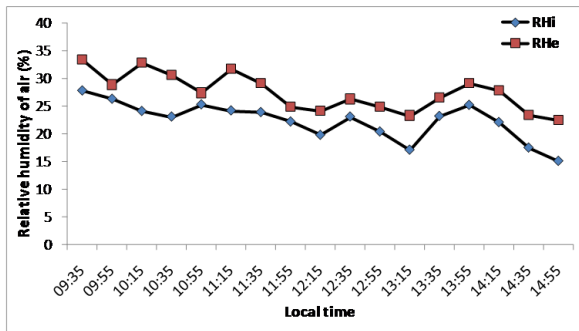


Figure 5. Evolution of relative humidity of the outside air (RHe) and under greenhouse (RHi) versus time of 04/29/2014

4.1.3. Air velocity

During the course of phosphate drying tests, the outside air velocity around the material samples is low enough; it ranges from 0.13 to 1.14 m/s. Nevertheless, air under greenhouse is almost stagnant (Fig. 6). Indeed the air velocity has little influence on the drying kinetics.

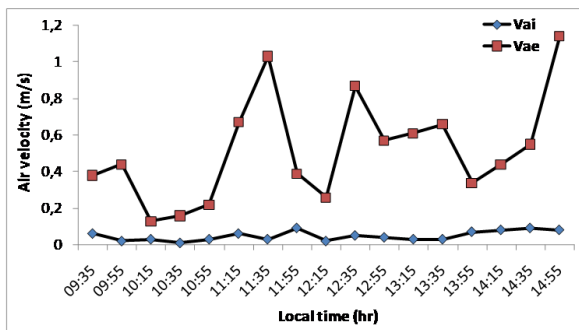


Figure 6. Evolution the outside air velocity (Vae) and under greenhouse (Vai) versus time of 04/29/2014.

4.1.4. The air and the material temperatures

During the day of 04/29/2014, the air temperature at the vicinity of the focus of the parabolic concentrator is considerably higher than that of the ambient air and the air inside the greenhouse; it reaches 484°C, while the air temperature inside the greenhouse reaches only a maximum of 50°C and ambient air temperature 40°C (Figs. 7a and 7b). However air temperature under greenhouse is higher than at outside (Fig. 7a).

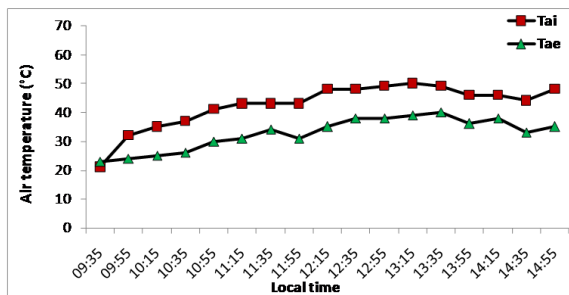


Figure 7a: Evolution of the air temperature at outside (Tae) and under greenhouse (Tai) versus time of 04/29/2014.

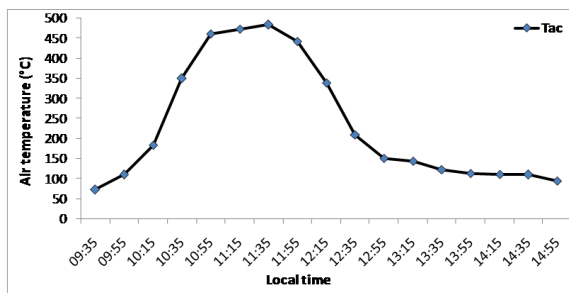


Figure 7b: Evolution of the air temperature at the focus of parabolic concentrator (Tac) versus time of 04/29/2014.

Thus, the phosphate temperature in open sun is greater than that of air; it reaches a maximum of 50°C. However, the phosphate temperature under the greenhouse reached a maximum of 59°C while that of the sample placed at the focus of the parabolic concentrator reached a maximum of about 102°C at solar noon (Table 2). Under direct solar radiation (in open air and under greenhouse) the material temperature exceeds that of the surrounding air. This result is in agreement with the researchers observations during drying of agricultural products [24-26].

Table 2: The air temperature and the phosphate temperature of 04/29/2014

Drying process	Air temperature			Phosphate temperature		
	Ta _{Min} (°C)	Ta _{Max} (°C)	Ta _{Moy} (°C)	Tp _{Min} (°C)	Tp _{Max} (°C)	Tp _{Moy} (°C)
Open sun	23	40	32,71	27	50	40,23
Greenhouse	21	50	42,53	27	59	49,19
Parabolic concentrator	73	484	234,18	26	102	66,15

Indeed, the phosphate temperature under greenhouse is consistently higher than that the phosphate dried outside (Fig. 8). However, the temperature curve of material placed at the focus of the parabolic concentrator in the course of time reaches a maximum of 102°C at midday-sun. Thus, the parabolic concentrator allows the phosphate reaching the air temperature of the artificial dryers drying used by CPG [27]. The phosphate temperatures at the end of the drying process are similar for the three methods (Fig. 8).

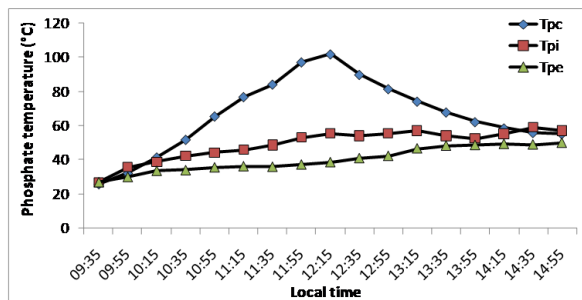


Figure 8. Evolution of the phosphate temperature (Tpe) in open air, at the focus of the parabolic concentrator (Tpc) and under greenhouse (Tpi) versus time of 04/29/2014.

4. 2. Drying kinetics

In Fig. 9 is shown the phosphate drying kinetics when it is placed respectively at the focus of parabolic concentrator, under greenhouse and in open sun. In fact, the phosphate dries faster when placed at the focus of the parabolic concentrator (Fig. 9).

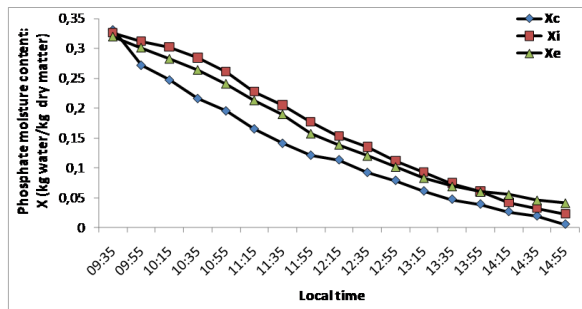


Figure 9. Variation of the water content of phosphate in open sun (Xe), by parabolic concentrator (Xc) and under greenhouse (Xi) versus time of 04.29.2014.

It accomplished 05 hr 20 min to dry to a water content $X_{c_f} = 0.006$ kg water/kg dry matter. However, the drying under greenhouse and in the open air does not reach to this value. We remark that phosphate

moisture content curve under greenhouse is nearly than that of the open sun (Fig. 9). Under greenhouse, the phosphate puts 05 hr 20 min to dry to a water content value $X_{i_f} = 0.022$ kg water/kg dry matter. However in the open air, the phosphate is dried to a water content value $X_{e_f} = 0.042$ kg water/kg dry matter. Drying the phosphate in the open sun is profitable. The phosphate drying kinetics in open sun and under greenhouse join and become assemblies.

In order to normalize the drying curves, the experimental data were transformed to a dimensionless parameter called the moisture ratio versus time (Fig. 10). The moisture ratios (XR) versus drying time were fitted to the nine drying models presented by previous workers (Table 1). The results of the statistical analysis undertaken on these models for solar drying by the parabolic concentrator, in open sun and under greenhouse are given in Tables 3, 4 and 5, respectively. The models were evaluated on the basis of R^2 , χ^2 and RMSE. The model that best predicts the drying process will have higher value of R^2 and lower values of χ^2 and RMSE. The Midilli model was found to be the most suitable model for describing drying curve of the thin layer of phosphate by the three drying process, as shown in Tables 3, 4 and 5. For the solar drying of phosphates by parabolic concentrator, the Midilli model gave $R^2=0.99858$, $\chi^2=1.48 \cdot 10^{-4}$, RMSE =0.01216. For the solar drying of phosphates in open sun the Midilli model gave $R^2 =0.99912$, $\chi^2=0.98 \cdot 10^{-4}$ and RMSE=0.00990. For the solar drying of phosphates under greenhouse the Midilli model gave $R^2=0.99969$, $\chi^2 =0.78 \cdot 10^{-4}$, RMSE =0.00886.

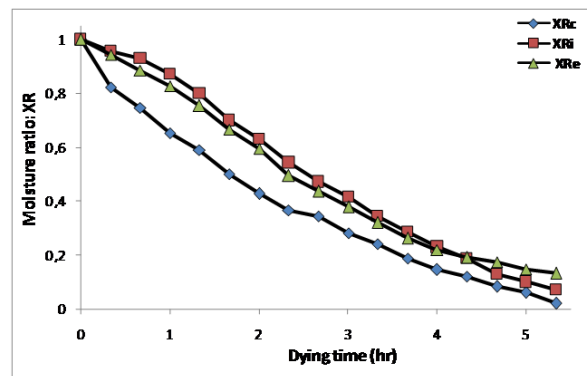


Figure 10. Variation of the moisture ratio in open sun (XRe), by parabolic concentrator (XRc) and under greenhouse (XRi) versus drying time of 04.29.2014.

Table 3: Modeling of moisture ratio according to drying time for thin layer parabolic concentrator drying of phosphates.

Model no.	Model constants	R ²	χ ²	RMS E
1	k=0.44603	0.987 30	10.8 10 ⁻⁴	0.032 89
2	a=1.00581, k=0.44877	0.987 36	11.5 10 ⁻⁴	0.033 89
3	n=1.0944, k=0.40851	0.989 95	9.13 10 ⁻⁴	0.030 21
4	a=1.16498, k=0.30313, c=-0.19832	0.997 24	2.69 10 ⁻⁴	0.016 40
5	k=0.44129, n=1.09498	0.989 95	9.13 10 ⁻⁴	0.030 21
6	a=0.9943, k=0.36939, n=0.82661, b=-0.03917	0.998 58	1.48 10⁻⁴	0.012 16
7	a=-40.29188, k ₀ =0.69413, k ₁ =0.68528, b=41.25687	0.992 41	7.95 10 ⁻⁴	0.028 20
8	a=-0.2402, b=0.01314	0.989 78	9.90 10 ⁻⁴	0.031 47
9	a=0.26964; k=0.4481; b=0.36808; g=0.44873; c=0.36808; h=0.44873	0.987 35	15.7 10 ⁻⁴	0.039 58

Table 4: Modeling of moisture ratio according to drying time for thin layer open sun drying of phosphates.

Model no.	Model constants	R ²	χ ²	RMSE
1	k=0.31942	0.9601 1	36.3 10 ⁻⁴	0.0602 4
2	a=1.09257, k=0.35403	0.9752 0	24.1 10 ⁻⁴	0.0490 6
3	n=1.43106, k=0.2013	0.9983 7	1.58 10 ⁻⁴	0.0125 9
4	a=1.51642, k=0.18643, c=-0.47126	0.9911 8	9.17 10 ⁻⁴	0.0302 8
5	k=0.32624, n=1.43078	0.9983 7	1.58 10 ⁻⁴	0.0125 9
6	a=0.98377, k=0.18825, n=1.5783, b=0.01079	0.9991 2	0.98 10⁻⁴	0.0099 0
7	a=0.54625, k ₀ =0.35402, k ₁ =0.35402, b=0.54631	0.9752 0	27.8 10 ⁻⁴	0.0527 0
8	a=-0.2402, b=0.01314	0.9897 9	9.90 10 ⁻⁴	0.0314 7
9	a=0.3642; k=0.35402; b=0.36419; g=0.35402; c=0.36417; h=0.354021	0.9752 0	32.8 10 ⁻⁴	0.0572 9

Table 5: Modeling of moisture ratio according to drying time for thin layer greenhouse drying of phosphates.

Model no.	Model constants	R ²	χ^2	RMSE
1	k=0.30671	0.923 29	79.6 10 ⁻⁴	0.0899 2
2	a=1.13055, k=0.35279	0.950 46	54.8 10 ⁻⁴	0.0740 5
3	n=1.70234, k=0.14136	0.998 91	1.21 10 ⁻⁴	0.0110 0
4	a=2.91269, k=0.08062, c=-1.86043	0.992 85	8.47 10 ⁻⁴	0.0291 1
5	k=0.31686, n=1.70216	0.998 90	1.21 10 ⁻⁴	0.0110 0
6	a=0.99698, k=0.13778, n=1.64228, b=-0.00842	0.999 69	0.78 10⁻⁴	0.0088 6
7	a=-53.61188, k ₀ =0.74239, k ₁ =0.72667, b=54.58721	0.995 94	5.17 10 ⁻⁴	0.0227 6
8	a=-0.19588, b=0.00246	0.989 01	12.2 10 ⁻⁴	0.0348 7
9	a=0.37684; k=0.35277; b=0.37684; g=0.35277; c=0.37684; h=0.35275	0.950 46	74.8 10 ⁻⁴	0.0864 8

5. Conclusion

This study extends to briefly explore the foundations of the combined Radiative-Convective drying of phosphate under uncontrolled and varying climatic conditions. This study is attended in part by the construction of a mini-greenhouse and a parabolic concentrator, on the other hand a series of measurements carried out on the drying of phosphate in open sun, under greenhouses and by a parabolic concentrator. Indeed, under continuous and intense solar radiation, the results of experimental tests have shown that the drying kinetics of phosphate in open sun and under greenhouse join and become assembly. The intensity of the radiation acts directly on the material temperature through the flow of heat conveyed by the radiation which accordingly promotes the mass internal transfers. Both of the solar drying process (open sun and greenhouse) puts a period of 05 hr 20 min to drying the phosphate.

Indeed, the air temperature at the focus of parabolic concentrator is much higher than that under greenhouse and than that in open air. The phosphate temperature under greenhouse is lower than with solar concentration at the focus of parabolic concentrator, accordingly this last phosphate dries more quickly. However, drying in open sun has advantages. It allows better productivity because large surface areas that

may be put in works and requires a very small investment compared to the price and the maintenance cost of parabolic concentrators.

The parabolic concentrator allows the phosphate reaching the air temperature of the artificial dryers drying used by CPG. The phosphate drying by a parabolic concentrator appears to us as one of the means to a greater availability over time and more economically profitable in the production of phosphate by the CPG. Indeed, a special search effort should be used to adopt new processes of solar drying of phosphate.

Acknowledgments

This research was supported by the Ministry of Higher Education, Scientific Research and Technology, Republic of Tunisia.

References

- [1] V. Belessiotis and E. Delyannis, Solar Drying, *Solar Energy*, 85 (2011) 1665-1691.
- [2] RETscreen plus 03/09/2013: Minister of Natural Resources Canada 1997-2013.
- [3] L. F. Gilles, The Development of Phosphate Materials with High added value: a Researcher Viewpoint, *Procedia Engineering*, 46 (2012) 45 - 53.
- [4] Safety Reports Series N°. 78: Radiation Protection and Management of Norm Residues in the

Phosphate Industry. International Atomic Energy Agency (IAEA), Vienna, 2013.

[5] K. Smida, *Aspects Technique et Énergétiques du Séchage : Réalisation et Mise au Point d'une Soufflerie. Chapitre III: Consommation énergétique du séchage* : 21-42. D.E.A. Tunis Faculty of Sciences, sustained December 7, 1999.

[6] Project of solar drying of phosphates of the Gafsa Phosphate Company (CPG). March, 2007.

[7] E. K. Akpınar, Drying of mint leaves in a solar dryer and under open sun: modelling, performance analyses, *Energy Conversion and Management*, 51 (2010) 2407-2418.

[8] A. Midilli and H. Kucuk, Mathematical modeling of thin layer drying of pistachio by using solar energy, *Energy Conversion and Management*, 44 (2003) 1111-1122.

[9] A. A. El-Sebaï and S.M. Shalaby, Experimental investigation of an indirect-mode forced convection solar dryer for drying thymus and mint, *Energy Conversion and Management*, 74 (2013) 109-116.

[10] E. K. Akpınar, Mathematical modelling and experimental investigation on sun and solar drying of white mulberry, *Journal of Mechanical Science and Technology*, 22 (2008) 1544-1553.

[11] T. Y. Tunde-Akintunde, Mathematical Modeling of Sun and Solar Drying of Chilli Pepper, *Renewable Energy*, 36 (2011) 2139-2145.

[12] İ. T. Toğrul and D. Pehlivan, Modelling of thin layer drying kinetics of some fruits under open-air sun drying process, *Journal of Food Engineering*, 65 (2004) 413-425.

[13] L. Ait Mohamed, C. S. Ethmane Kane, M. Kouhila, A. Jamali, M. Mahrouz and N. Kechaou, Thin layer modelling of *Gelidium sesquipedale* solar drying process, *Energy Conversion and Management*, 49 (2008) 940-946.

[14] G. Çakmak and C. Yildiz, The drying kinetics of seeded grape in solar dryer with PCM-based integrate collector, *Food and Bioproduct Processing*, 89 (2011) 103-108.

[15] A. S. Mujumdar, *Handbook of Industrial Drying*, New York: Marcel Dekker; 1987.

[16] S. M. Henderson and S. Pabis, Grain Drying Theory. II. Temperature Effects on Drying Coefficients, *Journal of Agricultural Engineering Research*, 6 (1961) 169-174.

[17] L. M. Diamante and P. A. Munro, Mathematical modelling of the thin layer solar drying of sweet potato slices, *Solar Energy* 51 (1993) 271-276.

[18] S. Singh, R. Sharma, A. S. Bawa and D. C. Saxena, Drying and Rehydration Characteristics of Water Chestnut (Trapanatans) as a Function of Drying Air Temperature, *Journal of Food Engineering*, 87 (2008) 213-221.

[19] D. G. Overhults, H. E. White, H. E. Hamilton and I. J. Ross, Drying soybeans with heated air, *Transactions of the America Society Agricultural Engineering*, 16 (1973) 112-113.

[20] A. Midilli, H. Kucuk and Z. Yapar, A new model for single layer drying, *Drying Technology*, 20 (7) (2002) 1503-1513.

[21] S. M. Henderson, Progress in Developing the Thin Layer Drying Equation, *Transactions of the America Society Agricultural Engineering*, 17 (1974) 1167-1172.

[22] C. Y. Wang and R. P. Singh, A single layer drying equation for rough rice, *American Society of Agricultural Engineers*, 1978, Paper n°3001.

[23] V. T. Karathanos, Determination of Water Content of Dried Fruits by Drying Kinetics, *Journal of Food Engineering*, 39 (1999) 337-344.

[24] S. Kooli, A. Fadhel, A. Farhat and A. Belghith, Drying of red pepper in open sun and greenhouse conditions: Mathematical modelling and experimental validation, *Journal of Food Engineering*, 55 (2007) 1094-1103.

[25] A. Fadhel, S. Kooli, A. Farhat and A. Belghith, Study of the solar drying of grape by three different processes, *Desalination*, 185 (2005) 535-541.

[26] A. Farhat, S. Kooli, C. Kerkeni, M. Maalej, A. Fadhel and A. Belghith, Validation of a Pepper Drying Model in a Polyethylene Tunnel Greenhouse, *International Journal of Thermal Sciences*, 43 (2004) 53-58.

[27] C. Rouissi, *Optimisation des sécheurs à la CPG (Séchage artificiel)*. Professional Master. Gafsa Faculty of Sciences, sustained November, 2007.

Removal of Zinc from water by adsorption on different adsorbent

Manal Larakeb , Leila Youcef and Samia Achour

*Research laboratory in Subterranean Hydraulics and of Surface - LARHYSS -
University of Biskra, POB 145, R.P., Biskra, Algeria*

manel.larakeb@yahoo.fr

Received date: January 30, 2016; accepted date: May 24, 2016

Abstract

The aim of this work is to study zinc removal possibility by adsorption on an Algerian bentonite (bentonite of Maghnia), goethite, powdered activated carbon (PAC) and kaolin. Various reaction parameter effects on process were tested. Experiments were carried out with synthetic distilled water solutions. Kinetic of adsorption results showed that after 20 minutes, zinc removal is maximal with 98.24 % efficiency for bentonite. Using Goethite, we obtained 18% efficiency after 30 minutes of equilibrium time. After 3 hours of stirring, zinc removal by PAC was maximal with 27.54% efficiency and after 1 hour for kaolin with 45.48%. Increasing in adsorbent dose (0.5 to 8 g/l) improves zinc removal efficiency for an initial 5mg/l concentration. Zinc removal efficiency by any adsorbent decreases with the increase of initial zinc concentration (2 to 20 mg/l). pH of treatment affects considerably zinc retention rate. Zn removal efficiencies are noticeable at basic pH. Order of efficiency of tested adsorbents for zinc removal in synthetic solution follows: bentonite > kaolin > PAC > Goethite.

Keywords: Zinc, adsorption, bentonite, goethite, powdered activated carbon, kaolin.

1. Introduction

Wastewater pollution by heavy metals is a major environmental hazard, since dissolved toxic metal ions may ultimately reach the highest food chain level and become a risk factor for human health. Unlike most pollutants, heavy metals are not biodegradable and tend to accumulate in living organisms causing various diseases [1]. Most commonly cited metals are copper, chromium, nickel and zinc for their numerous industrial applications [2].

In this study, we take the case of zinc is an essential element for all living organisms, including humans and modern life would be inconceivable without zinc, since it plays an essential role in human being metabolism. Major zinc sources in environment are copper and bronze alloys production and galvanization [3,4]. For example, it is vital for more than 200 enzymes correct operation, DNA stabilization, genes expression and signals transmission from nervous system. Human body contains 2 to 3 g of zinc (for 7 g of iron), which are found throughout the body, but with higher concentrations in muscles, liver, kidneys, bones and prostate [5]. It is also used in paints, rubber, plastics, cosmetics and pharmaceuticals

[3]. According to International Association of zinc; reduced sensations of taste and smell, skin disorders, mental lethargy and fertility decrease are the main symptoms associated with zinc deficiency in human body.

However, excessive zinc consumption can be toxic and cause nausea, stomach cramps, vomiting, and slow liver dysfunction... Zinc can also have adverse reactions on environment because it can cause several problems when released in very small quantities, since its toxicity grows by bioaccumulation. Some Algerian studies treated pollution hazards. Natural water reserves in certain regions near industrial areas, for which zinc is in their discharges composition, are contaminated [6, 7].

However, the allowable maximum zinc concentrations in drinking water are 3 to 5 mg/l according to the World Health Organization [8] and 5 mg/l by Algerian standards [9]. In order to meet this standard, several methods have been used to remove zinc as membrane filtration (ultrafiltration, reverse osmosis, nanofiltration, electrodialysis), chemical precipitation, ion exchange and electrochemical method [10]. Adsorption process on clays [11, 12, 13, 14,15,4], on hydroxides [16, 17] and activated carbon

[18, 19] has also proven its effectiveness in laboratory works.

Therefore, the objective of this work is to study bentonite of Maghnia (Algeria), goethite, powdered activated carbon powered and kaolin effectiveness for zinc removal from synthetic distilled water solutions.

Many reaction parameters were tested to optimize the process as contact time, effect of adsorbent dose, effect of initial zinc concentration and pH of treatment.

2. Materials and Methods

Solutions of zinc

A 1000 mg/l zinc stock solution was prepared in distilled water and stored away from light, while using zinc sulfate ($ZnSO_4 \cdot 7H_2O$) as salt. Then, we dilute in different ratios to prepare lower solution concentrations used in tests.

Tested adsorbent

- **Bentonite:** Used clay is a sodic bentonite, white colored, rich in montmorillonite. It is obtained from Hammam Boughrara deposit (Maghnia, N.E of Algeria). This bentonite has acidic pH (pH = 6.2) with a $80 \text{ m}^2/\text{g}$ specific surface.

- **Goethite :** Used goethite is a FLUKA product. It is an iron hydroxide which chemical formula is $Fe(OH)O$ and specific surface is of $20.5 \text{ m}^2/\text{g}$.

- **Activated Carbon :** Powdered activated carbon is a DARCO Aldrich lab product, which granulometry is 12 to 20 mesh (0.3 to 0.5 mm) and specific surface is $550 \text{ m}^2/\text{g}$.

- **Kaolin :** It is an Aldrich product which chemical formula is $(AlSi_2(OH)_4)$, and specific surface is $19.8 \text{ m}^2/\text{g}$.

pH measurement

To measure pH of water samples, a pH meter (HANNA pH 210) was used with a combined electrode (Bioblock Scientific). The pH-meter is calibrated before any measurement series using two buffer solutions of pH 4.01 and 9.18.

Determination of metal concentration

An atomic absorption spectrometer (Shimadzu AA-6200) with hollow cathode lamp and air acetylene flame, was used for determining Zinc concentrations in water samples, at a wavelength $\lambda = 213.86 \text{ nm}$.

Adsorption test description

Zinc removal tests were carried out discontinuously on a magnetic stirrer using synthetic zinc solution contact with a constant mass of each adsorbent.

Solid/liquid sample separation is achieved by vacuum filtration using membrane with $0.45 \mu\text{m}$ porosity. For each filtered sample, we measured pH and residual zinc concentration.

Several tests were performed to examine some parameters influence on zinc removal on any adsorbent such as stirring time (0 to 6 hr), initial Zn^{2+} content (2 to 20 mg/l), adsorbent dose (0.5 to 8 g / l) and pH of treatment (4 to 9). pH of solutions was adjusted to the desired value by adding HCl (0.1 N) or NaOH (0.1N) during adsorption test.

3. Results and discussion

Kinetics of adsorption

We followed zinc kinetics of adsorption for initial zinc content at 5 mg/l and for both adsorbents constant mass (1g/l). Residual zinc content and pH follow-up were achieved depending on stirring time (from 2 min to 6 hrs).

Obtained results (Fig 1) show that zinc removal efficiency varies with stirring time. We obtained maximum efficiency after 20 min, 30 min, 60 min and 180 min for bentonite, kaolin, goethite and PAC respectively. Maximal removal values corresponding to these times are 98.24 %, 45.48%, 27.54% and 18 % respectively.

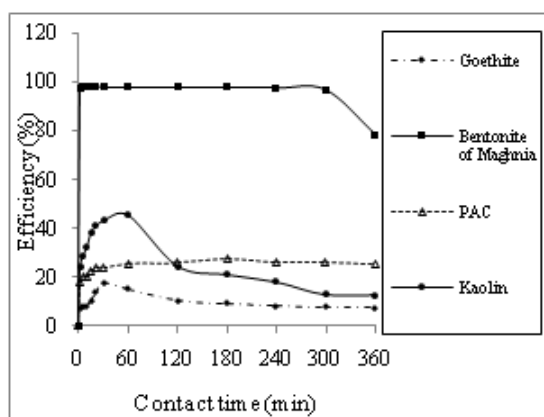


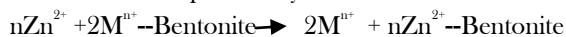
Figure 1: Kinetics curve for Zinc (5mg/l) removal using bentonite, goethite, kaolin and PAC.

Zinc fixation kinetics evolution on clays PAC or hydroxides mainly proved reversibility of exchange engaged and physical nature of adsorbent-zinc interactions.

We can differentiate two steps in zinc kinetics of adsorption for both clays. During first step, we have a rapid efficiency increase, explained by zinc ions quick fixation on both adsorbent surfaces, it is external mass transfer step. Kinetics second step shows that zinc residual content decreases progressively.

Veli and Alyuz [20] tested Zn^{2+} removal, using bentonite of Cankiri (Turkey), prove that pH is an important factor in adsorption process as it generates electrostatic changes in solutions, also showed that equilibrium is reached after very short time (0.5 min).

Bradl [21], supposed that adsorption mechanisms include ion exchanging (reaction and fixation). Reaction between Zn^{2+} and cation exchangeable at clay surface can be expressed by:



n: Exchangeable cation valence.

M: Exchangeable cation by Bentonite like Na, K, Mg and Ca.

Arias and Sen [4] studies indicate clearly that zinc metallic ion adsorption (Zn^{2+}) on kaolin goes through 02 steps: a very fast adsorption of zinc metallic ion at external surface, followed by intra-particle diffusion inside adsorbent. Equilibrium time is 60 minutes.

Madhava Rao and al [18], studied zinc removal by adsorption on activated carbon from Ceiba pentandra capsule (agricultural waste). Obtained kinetics expressed that equilibrium time is 50 min for initial zinc concentration of 50 mg/l and initial pH = 6.

Kouakou and al [22], tested zinc adsorption on commercial activated carbon, presented 20 ml of homogenized industrial water with 0.1g of activated carbon in a beaker of 250ml, applied many hours of

stirring time. Equilibrium time found was 01 hr at pH 6 and at 27°C.

Several studies also confirmed activated carbon effectiveness to remove zinc as Monser and Adhoum study [23], who produced steady bed column results on ions adsorption for Cu(II), Zn(II) and Cr(VI) on modified activated carbon with sodium-diethyl-dithiocarbamate (SDDC). They found that activated carbon modified with SDDC has an effective displacement capacity for Cu (II) (04-times), Zn (II) (04-times) and Cr (VI) (02-times) greater than unchanged activated carbon.

They reported also that SDDC is adsorbed on hydrophilic part of carbon surface.

Gräfe and Sparks [24] studied zinc and arsenic kinetics of adsorption on goethite. They found that 95 % and 72 % of zinc and arsenic were adsorbed in first 08hrs at pH 7.

Effect of adsorbent dose

The effect of adsorbent dose on the removal of zinc was studied for initial zinc concentration of 5mg/l. Dose of adsorbent was varied from 0.5 to 8 g/l and the solutions were kept under stirring for 20 min, 30 min, 01 hr and 03 hrs in presence of bentonite goethite, PAC and kaolin respectively. For each treated sample, residual zinc content and final pH was measured.

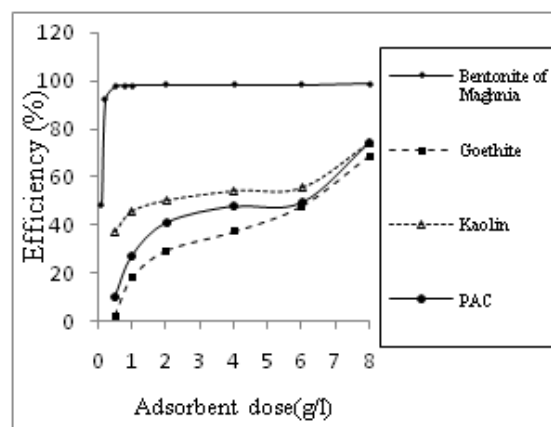


Figure 2: Effect of adsorbents dose on removal of zinc (5 mg/l)

Obtained results show that zinc removal efficiency increases with introduced adsorbent dose increasing (fig 2). At 8g/l of bentonite, efficiency reaches 98.68 % and all residual contents obtained in zinc are largely low than 3 mg/l potability standard [25]. Efficiency stability over bentonite dose of 1g/l is due to adsorption site saturations.

Goethite, Kaolin and PAC efficiencies increase with adsorbent dose increasing and reach 68.68, 74.4 and 74.2%, respectively, for 8g/l dose of each adsorbent.

We have obtained same result by treating distilled synthetic water solution, initially containing 5 mg/l Zinc and varying bentonite dose (Calcic Bentonite) from 0.1 to 8 g/l [14]. According Zhang and al [26], zinc removal efficiency (100 mg/l) increases with Bentonite dose increasing (0.2 to 2 g/l).

Madhava Rao and al [18] studied activated carbon dose (100 to 400 mg/l) effect, they found that efficiency get improved with adsorbent dose increasing until 300 mg/l, almost reaches 100%. Beyond this dose, efficiency remains nearly stable. Same result was found by Depci and al [19], who tested (VAAC) carbon dose effect on Pb (II) and Zn (II) removal, 0.01-0.2 g VAAC was added to test-tubes containing 40 mg/l of ion in solution. Obtained results showed efficiencies of 91.5 % and 78 % for Pb (II) and Zn (II) respectively with 0.1 g VAAC. Above this weight, efficiencies became almost constant.

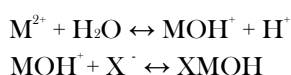
Mishra and Patel [27] found same result using kaolin (5 to 20 g/l) to treat distilled synthetic solutions initially containing 100 mg/l of zinc.

Table 1 show that pH equilibrium increase as increasing dose of each adsorbent tested.

Table 1 : pH evolution according to both adsorbent dose at equilibrium time.

Adsorbent dose (g/l)	0.5	2	4	6	8
Goethite	5.62	5.63	5.65	5.73	5.93
Bentonite	7.56	7.94	8.02	8.12	8.33
Kaolin	6.19	6.20	6.22	6.26	6.46
PAC	6.02	6.22	6.62	6.69	6.65

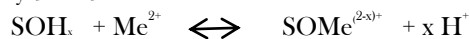
Basta and Tabatabai [28], proposed the following mechanism for metal adsorption on negative bentonite sites:



X : Bentonite surface ; **M :** Metal.

Also, regarding reached pH for increasing bentonite doses, a zinc precipitation phenomenon as hydroxide form, can also be generated [29].

Benjamin and Leckie [30], proposed the following mechanism to describe divalent metal adsorption at iron hydroxide surface :



x: Proton number free by adsorbed metal (**Me**).

SOH_x : Average site surface concentration, occupied by metal.

Effect of initial concentration of zinc

After using 1 g/l of adsorbent and varying initial ion metal concentration from 2 to 20 mg/l, solutions were stirred during contact time of 20 min, 30 min, 01

hr and 03 hrs contacts with bentonite, goethite, PAC and kaolin respectively.

According to results shown in Fig 3, we can notice that all curves represent same rate. Treatment efficiency decreases with initial zinc increasing

Efficiencies decrease may due to adsorption site saturation at each adsorbent surface.

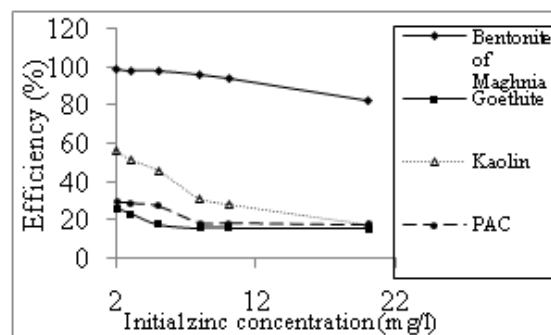


Figure 3: Effect of Initial concentration in removal of zinc

By varying initial zinc content from 2 to 20 mg/l and setting calcic bentonite dose at 1g/l, we also noticed zinc removal efficiency decreasing [14]. Same note was done by Zhang and al, [26], when varying Zn(II) initial content between 30 and 250 mg/l for same bentonite dose.

Shahwan and al [15], results confirmed that kaolin effectiveness in zinc removal is noticeable at low concentrations (1, 100 and 500 mg/l) of this metal. This effectiveness decreases progressively for initial zinc contents from 1 mg/l to 10000 mg/l. They also studied MgCO₃ - kaolin mixture to remove zinc. Initial zinc content was varied from 0 to 2500 mg/l and set kaolinite mass with variation in MgCO₃ content (5, 10, 25 and 60 %), noticed adsorptive capacity increasing with MgCO₃ percentage raising and with initial zinc content raising from 0 to 200 mg/g for 60 % of MgCO₃.

Balistreri and Murray [31] have tested goethite to remove zinc in synthetic solutions which initial zinc contents range from 0.037 to 1.9 mg/l. Results noticed that efficiencies decrease with initial zinc content whatever was pH treatment (5 to 8).

A same result was found by Theis and West [32], for solutions of 0.45 to 4.33 mg Zn/l treated in presence of 0.6 g/l of goethite.

According to Madhava Rao and al [18], efficiencies decrease with initial zinc content increasing from 40 to 200 mg/l at pH 6 and activated carbon fixed dose of 10g/l.

While Depci and al [19], tested the activated carbon (VAAC) prepared with local agricultural waste as apple-plup to remove lead and zinc, found that both metal adsorptive capacity increases when initial concentration increases (25, 30, 35 and 40 mg/l) at

fixed dose of adsorbant (4 g/l). Same result found by Ramos and al [33], who studied zinc removal on three carbon types (Carbon from Mexico, Carbon modified with HSL and Carbon modified with F-300 and F-400). Initial zinc content was ranged from 0 to 60 mg/l with 1g/l previous carbons at pH 7.

Zinc adsorption isotherm

Results operation according to Freundlich and Langmuir laws is made by considering a fixed adsorbent dose (1g / l) and varying concentrations of initial variable Zn concentrations from 2 to 20 mg/l. Linearized forms of these models are expressed by Weber and al [34] :

Freundlich isotherm equation:

$$\log \frac{x}{m} = \log k + \frac{1}{n} \log C_e$$

Langmuir isotherm equation:

$$\frac{m}{x} = \frac{1}{q_m} + \frac{1}{q_m \times b} \times \frac{1}{C_e}$$

C_e : Zinc concentration at equilibrium (mg/l)

$x = (C_0 - C_e)$: Fixed zinc quantity (mg/l)

m : Adsorbent mass (g)

q_m : Ultimate adsorption capacity (mg/g)

k, n, b : Adsorption constants

Through least-squares method adjustment, we obtain for each studied law and tested adsorbent, straight with correlation coefficients between 94.9% and 99.3% (Figure 4). Various constants deduced from obtained straight equations are summarized in Table 2.

Linearized forms application of Freundlich and Langmuir laws allowed verifying that these two models are appropriate and zinc removal efficiencies vary in same way with both models. Behavioral differences seem to appear because of maximum adsorption capacity q_m for each adsorbent. Best adsorption capacity is obtained for bentonite 13.89 mg/g, then 3.70., 3.29 and 2.91 mg/g for kaolin, PAC and goethite respectively.

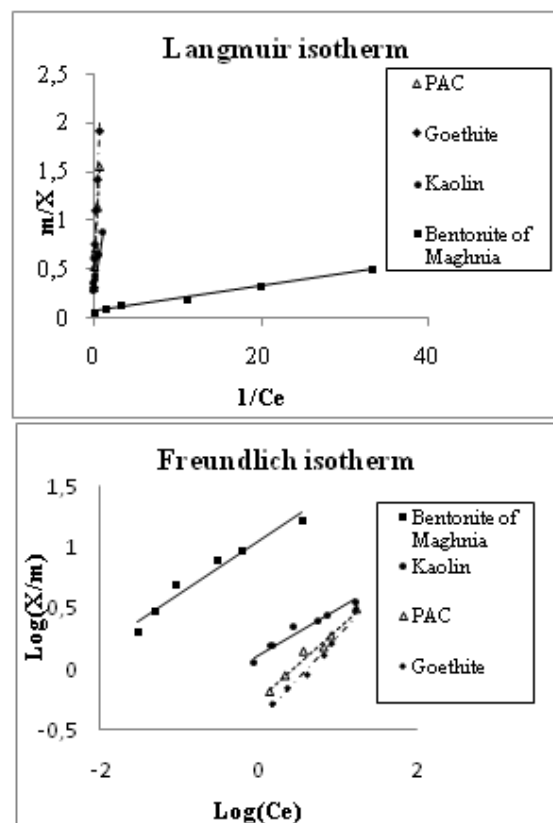


Figure 4: Freundlich and Langmuir isotherms for zinc removal on bentonite of Maghnia, goethite, PAC and kaolin.

Table 2 : Freundlich and Langmuir isotherm parameters.

Adsorbent	Freundlich			Langmuir		
	n	k	R ²	q _m (mg/g)	b (l/mg)	R ²
Bentonite	2,35	11,07	0,949	13,89	5,54	0,993
Kaolin	2,65	1,32	0,951	3,70	0,50	0,989
Powdered activated carbon	1,69	0,55	0,973	3,29	0,18	0,978
Goethite	1,41	0,37	0,980	2,91	0,14	0,961

Effect of pH

Zinc adsorption experiments were conducted in presence of 1g/l of adsorbent and 5 mg/l of zinc. pH was adjusted to 4, 6, 7 and 9 successively and maintained constant during stirring time about 20 min, 30 min, 01 hr and 3 hr and 01 hr for bentonite, goethite, kaolin and PAC, respectively, using NaOH (0,1N) and HCl (0,1N) solutions.

Experiments results (Fig 5) shows a gradual increase in adsorption with increase of pH.

For bentonite, kaolin, PAC and goethite, best efficiencies are obtained in basic medium while best one is at pH 9, with removal rates at 98.44%, 82.2%, 85.15% and 92.26 %, respectively.

Adsorption increasing with pH is due to adsorption site number increasing depending on pH (hydroxyl groups, oxydes and clay minerals) as well as H^+ ion competition reduction and preferential ($ZnOH$) hydrolyzed species adsorption.

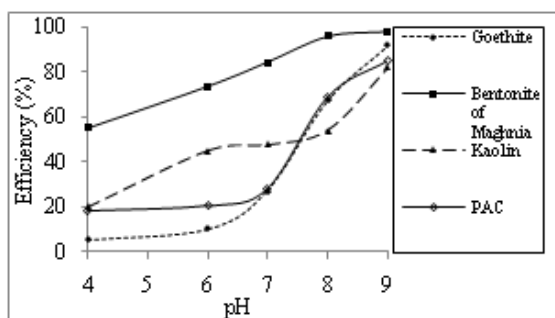


Figure 5 : Effect of pH on removal of zinc (5 mg/l) by adsorption on bentonite, goethite, kaolin and PAC.

Sen and Gomez, Larakeb and al, Mohammed Azizi and al [12, 14, 13], confirmed that zinc removal efficiency increase on bentonite with pH increasing. According to Abollino and al, Achour and Youcef, Youcef and Achour [28, 35, 36], metallic ions adsorption on sodic bentonite decreases with pH decreasing.

At low pH, hydrogen ions compete with heavy metals for surface sites. In addition, Si-O and Al-O groups are less deprotonated and hardly form complexes with divalent and trivalent ions.

Zhang and al, [26] showed that zinc removal by bentonite as adsorbent depends highly on pH. Removal percentage increases with pH increasing from 1 to 7. Low efficiencies at $pH < 2$ may be due to competition raise for adsorption sites between H^+ and Zn^{2+} . By pH increasing, negative charge site number increases which facilitates more Zn^{2+} ions adsorption. At $pH > 7$, $Zn(OH)_2$ precipitation plays the main role in Zn^{2+} removal.

The study of removal of copper, zinc and cadmium by adsorption on goethite enhanced that adsorption zinc efficiency increase from 15 to more than 90 % with pH increasing between 6 and 7 [37].

Arias and Sen [4] and Mishara and Patel [26] applied experiments confirmed that zinc removal efficiency on kaolin increases with pH increasing.

Madhava Rao and al, [18] indicated that best efficiency of removal of zinc by adsorption on carbon is founded at pH 6 for initial 50 mg/l zinc concentration, 300 mg/l carbon dose and 50 min stirring time. Ramos and al,[34] tested pH effect on adsorption phenomenon. They noticed that pH solution raised during Zn (II) adsorption on carbon F-400 and diminish during adsorption on carbon from Mexico. Consequently, both Zn^{2+} and H^+ ions were simultaneously adsorbed

on carbon F-400 surface and probably competed for same ions. For carbon from Mexico, Zn^{2+} ions were adsorbed while H^+ ions were desorbed on its surface. This last phenomenon, known as ions exchange, and H^+ was probably adsorbed from surface site where Zn^{2+} can be adsorbed.

The tests of pH effect on copper, zinc and cadmium adsorption on goethite, show that zinc adsorption efficiency increase from 15 to 80% for copper and lead at pH 7 and 8, respectively, 70% at pH 7 for zinc and from 50 to 60% at basic medium (pH 8 and 9) [38].

Conclusion

Our work aimed to study zinc removal possibilities by adsorption on clays (bentonite of Maghnia, kaolin), on an iron oxide (goethite) and on powdered activated carbon (PAC). Applied study, we achieved, allowed us to notice that:

- Equilibrium time is reached after 20 min of stirring solutions of zinc (5 mg/l) in presence of bentonite of Maghnia and 30 min, 60 min and 180min in presence of goethite, kaolin and powdered activated carbon respectively.

- Zn removal efficiency is improved with adsorbent dose increasing (0.1 à 8 g/l). For bentonite doses greater than 1g/l, zinc removal efficiency exceeds 98.68%. However, at 8g/l dose of kaolin, PAC and goethite, it only reaches 74.4, 74.2 and 68.68%, respectively.

- Zinc removal, by adsorption on above adsorbents, is more effective for water at low zinc contents, and treatment efficiency decreases with initial zinc content increasing (2 to 20 mg/l).

- Zinc adsorption is influenced by pH. Best efficiencies were obtained on basic mediums.

Tested adsorbent efficiency for zinc removal in synthetic solution follows the order:

bentonite of Maghnia > kaolin > PAC > goethite, independently from reaction parameter variations (contact time, adsorbent dose, initial zinc content and pH of treatment).

References

- [1] C.N .Sawyer,. P.L. Mccarty., G.F .Parkin., Chemistry for Environmental ,Engineering and Science, 5th ed. (2003). Mc-Graw Hill. 1-741.
- [2] L .Deroche., S.Devaux. Etude bibliographique , école des mines douai, (2009).p1-42.

- [3] C.H .Weng., C.P .Huang, *Colloids Surf. A: Physicochem. Eng. Aspects*, 247, (2004). 137-143.
- [4] F .Arias., T.K .Sen., *Revue Source Colloids and surfaces. A, Physicochemical and engineering aspects*, Vol. 348, n°1-3, (2009). pp. 100-108 .
- [5] IZA. *Le zinc dans l'environnement 2ème édition* .Document publié par l'Association Internationale du Zinc .(1997) ,p 1-18.
- [6] F .Derradji., N .Kherici., R .Caruba., M .Romeo., *Cahiers de l'ASEES*, Vol. 8, n° 1, (2003). 35-42.
- [7] A .Gaagai., L .Benchaiba., *science lib éditions Mersenne*, Vol. 4, ,(2012). n ° 120402. P1-6.
- [8] W.H.O.Guidelines for drinking-water quality, third edition, incorporating 1st and 2ndAddenda, Vol.1, .(2008) Recommendations. Geneva.
- [9] JORA *Journal officiel de la république algérienne* n°34 , Decret exécutif du 17 Rajab 1432 correspondant au 19 Juin (2011).
- [10] Degremont.*Mémento technique de l'eau*, 9^{ème} Ed., Ed, Lavoisier, . (1989). Paris.
- [11] C .Abdelouahab., H .Ait amar., T.Z .Obertenov., A. Gaid., *Rev. Sci. Eau.*, Vol. 13, n° 2, (1987).33-40.
- [12] T.K .Sen, D .Gomez. , *Desalination*, n° 267.(2011). 286-294.
- [13] F .Mohammed-Azizi., S .Dib., M .Boufatit ,*Desalination and Water Treatment*, (2013). 1-12.
- [14] M .Larakeb., L Youcef., S .Achour., *Quatrième Forum de l'Eau, Les ressources en eau : effets des changements climatiques et perspectives d'adaptation*, le 24, 25 et 26 Mars, .(2014). Université de Gabès, Tunisie.
- [15] T .Shahwan, B. Zumbul, A.E .Eroglu, S .Yilmaz, *Applied Clay Science*, n° 30, (2005). 209-218.
- [16] MDA. Bolland., AM .Posner., JP .Quirk. *Australian Journal of Soil Research*, Vol. 15, n° 3, (2008). 279 - 286 .Boston.
- [17] P. J .Swedlund., G. M .Miskelly. and A. J .Mcquillan . *Geochim. Cosmochim. Acta* 73, (2009) .4199-4214.
- [18] M .Madhava Rao , G.P .Chandra Rao , K .Seshaiah , N.V .Choudary., M.C .Wang , *Waste Management* 28 (2008). 849-858.
- [19] T .Depci , A.R .Kul., Y. Onal ,*Chemical Engineering Journal* ,(2012) .224- 236.
- [20] S .Veli., B . Alyuz., *Journal of Hazardous Materials*, Vol.149, n°1 ,(2007) 226-233.
- [21] H.B .Bradl.. *J.Colloid Interface Sci*, n° 277, (2004). 1-18.
- [22] U .Kouakou , A .Serge Ello., J .Aboua Yapo , A.Trokourey, *journal of environmental chemistry and ecotoxicology*, Vol 5, n°6.,(2013), pp 168-171.
- [23] L .Monser., N .Adhoum. *Sep. Purif. Technol.* 26, (2002). 137-146.
- [24] M .Gräfe., DL .Sparks. , *Geochimica et Cosmochimica Acta*, Vol. 69, n° 19, (2005). pp. 4573-4595.
- [25] W.H.O.Guidelines for drinking-water quality, third edition, Volume 1-.(2004).Recommendation, Geneva.
- [26] H .Zhang., Z .Tong., T .Wei., Y .Tang., *Desalination* n° 276, (2011). 103-108.
- [27] P.C .Mishra., R.K .Patel., *Journal of Hazardous Material*, n° 168, (2009). 319-325.
- [28] N. T .Basta., M. A .Tabatabai., *Soil Sci.*, Vol. 153, n°2, (1992). 108 - 114.
- [29] O .Abollino., M .Aceto., M .Malandrino., C. Sarzanini., E .Mentasti., *Wat. Res.*, n°37, (2003). 1619-1627.
- [30] M.M .Benjamin., J. O.Leckie..*Environ. Sci. Tech.* 15, (1981). 1050-1057.
- [31] L.S .Balistriero., J.W .Murray, *Geochimica ei Cosmochimico Acta* Vol. 46, (1982). 1253 - 1265
- [32] T. L .Theis., M. J .West , *Environmental Technology Letters*, 7:1-12, (1986) .309-318.
- [33] R.L .Ramos., L.A.B Jacome., J.M .Barron., L.F .Rubio., R.M.G .Coronado. *J. Hazard. Mater.* B90, (2002). 27-38.
- [34] W. J. Weber., P. M .Mc Ginley., L. E .Ktz. *Water Research*, Vol. 25 .(1991). 499-528.
- [35] S .Achour., l .Youcef. *LARHYSS Journal*, n°2, (2003). 69-81, Biskra, Algérie.
- [36] L .Youcef., S .Achour.. *Séminaire international sur les géosciences au service du développement durable*, 26-28 Novembre, (2006). Tébessa, Algérie.
- [37] E .Spathariotis , C .Kallianou. *Communications in Soil Science and Plant Analysis*, n°38, (2007).. 611-635.
- [38] D. P .Rodda., B.B. Johnson., J. D. Wells. *Journal of Colloid and Interface Science* , Vol. 161, n° 1, (1993).57-62.

Dependence of hardness to the applied load of the 42CrMo4 steel manufactured by MIM process

Ana Fudurić^a, Nikola Šimunić^{a,b} and Denis Kotarski^{a,b}

^aKarlovac University of Applied Science, 47 000 Karlovac, Croatia

^bFaculty of Mechanical Engineering and Naval Architecture, 10 000 Zagreb, Croatia

fuduric.ana@vuka.hr

Received date: May 19, 2016; revised date: June 03, 2016; accepted date: June 04, 2016

Abstract

For the purposes of this article the hardness of material 42CrMo4 steel which is manufactured by metal injection molding (MIM) process was measured by Vickers method. When determining hardness the following loads: 196,1; 294,1; 392,2; 490,2; and 980,4 N were used. The objective was to determine the unknown relationship between applied load and hardness. A numerical processing of the experimental data was performed in the software package MATLAB (v.R2012.a, The MathWorks, Inc., Natick, MA, USA). The impact of the load on the hardness was determined by regression analysis. In calculating the undetermined coefficients two mathematical models were used, Meyer's law and a model of resistance proportional to the properties of the sample (PSR). The results show that used mathematical models very well describe the effect of the load on the measured hardness.

Keywords: steel 42CrMo4, hardness, metal injection molding

1. Introduction

Metal injection molding (MIM) combines two technologies, plastic injection molding and powder metallurgy. MIM process is ideal for small production of complex parts with excellent mechanical properties. Compared to traditional manufacturing process MIM offers greater freedom of designing parts made from stainless steel, nickel-iron, copper, titanium and other metals [1]. A very important step in the MIM process is the production of raw materials which will be used. In order to achieve good flow, which is required in the metal injection molding process, the powder is mixed with thermoplastic polymers (also known as a binder) in a hot state to form a mixture in which all metal particles are equally coated with the binder. The result is a non-united sample which is then subjected to a binder removal process. Mixing metal or ceramic powders with organic binders in the production process is a critical step to ensure a quality product [2]. Research has shown that MIM improves product quality, reduces production time and achieves cost savings of up to 50%. Although new technology, MIM

process is becoming widely accepted as a standard procedure in the number of industrial sectors including medical, military applications, precision engineering and automotive industry.

2. Hypothesis

Numerous studies show that the hardness depends on the load. For most materials hardness reduces with increased load (normal impact load hardness), while some material hardness increases with load (reverse impact load for the hardness) [3]. In our case dependence of load to hardness is not defined because the properties of parts manufactured by MIM process are unknown. So, the main objective of this study is to determine the relationship between load and hardness of material manufactured by MIM process.

For the purposes of this paper material samples of 42CrMo4 steel hardness were measured by Vickers method. Hardness testing is probably the most commonly used test of mechanical properties. Despite the mechanical properties are determined by testing, the hardness is not physically unambiguously defined

size, and is correlated with other mechanical properties. This primarily refers to the tensile strength, resistance to abrasive wear and so on. For the test it is not required to make a special tube, but it is only appropriate to prepare the sample surfaces or mechanical parts. The most commonly applied method for measuring the hardness of metal materials are methods of Vickers (HV) and Brinell (HB).

For each of five specified loads 15 samples were measured (every load three prints), which resulted in total of 225 prints measured. The prints were taken on the random places of the samples. The dimensions of samples are 6x4x44 mm. The samples were hardened on 850°C for 30 minutes and cooled in oil. Prior to measuring, the surface of samples was prepared with 80 gritt sand paper.

All measurements were done on the device VEB Werkstoffprüfmaschine "Fritz Hecker" (Figure 1). The following loads were used: 196,1; 294,1; 392,2; 490,2 and 980,4 N.

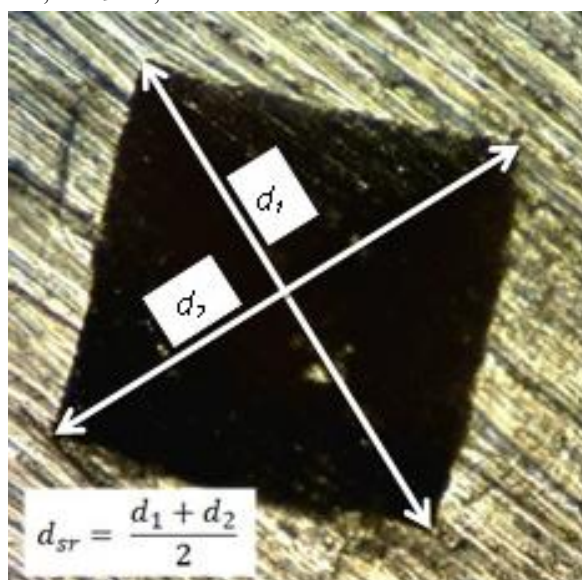


Figure 1. Vickers imprint of diamond pyramid

The microstructure of 42CrMo4 steel is homogeneous and has a very low share of non-metallic inclusions. Table 1 shows the chemical composition of 42CrMo4 steel which was measured by spectroscope Arun PolySpek model M.

Table 1. Steel chemistry 42CrMo4 [4]

C, %	Si, %	Mn, %	Cr, %	Mo, %
0,41	0,20	0,75	1,05	0,23

2.1. Regression analysis

When the mathematical model of behavior is not known, there are several methods to obtain it from

experimental results. One such method is regression analysis. Results are experimentally obtained for various levels of factors. From each level and appropriate results, couples of numerical values are formed [5]:

$$(x_i, y_i) = x_1y_1, x_2y_2, x_3y_3, \dots, x_ny_n \quad (1)$$

which in the case of the tests can be shown by table 2.

2.2. Regression analysis in Matlab

The regression of analysis was used to determine impact of the load on the hardness. There are several mathematical models that are used for the quantitative determination of dependence of the applied load and the size of the print like Meyer's law and model of resistance proportional to the properties of the sample [6,7].

Numerical processing of the experimental data was performed using the software package MATLAB (v.R2012.a, The MathWorks, Inc., Natick, MA, USA). As an input data for the calculations measured data was used (Table 2).

Table 2. Summary results

Load, N	d_{sr} , mm	Hardness, HV
196,1	0,3643 ± 0,0063	285,1
294,1	0,4480 ± 0,0046	278,3
392,2	0,5170 ± 0,0065	273,8
490,2	0,5808 ± 0,0118	204,4
980,4	0,8259 ± 0,0056	269,9

2.3. Polynomial regression - Meyer law

Meyer's law is mathematical model that describes connection between the applied force F and measured diagonal base print d of Vickers pyramid in the material. According to the literature value of Meyer index n is in the range from 1.5 to 2.0. If Meyer's index is $n < 2$ then the hardness depends on the applied load, and if $n = 2$ then the applied load has no effect on the measured hardness (Figure 2). The mathematical form of Meyer's law states [3]:

$$F = k \cdot d^n \quad (2)$$

where:

F [N] - applied force,

k - material constant,

n - Meyer's index

d [mm] - diagonal imprint.

The most commonly used regression models are those which meet the description of the regression line using a polynomial. In this case, polynomial regression was performed using Meyers law.

To be able to make a polynomial regression, function describing Meyer’s law must first be linearized.

$$F = k \cdot d^n \tag{3}$$

$$\log F = \log(k \cdot d^n) \tag{4}$$

$$\log F = \log k + \log d^n \tag{5}$$

$$\log F = \log k + n \cdot \log d$$

(6)

$$y = \log F$$

(7)

$$b = \log k$$

(8)

$$n \cdot \log d = n \cdot x$$

(9)

$$y = nx + b \tag{10}$$

Once the function is linearized it is necessary to adapt the measured data, to the new linearized model. Adjusted data for Meyer’s law are shown in table 3.

Table 3. Example of coding data for Meyer’s law

Log(F)	Log(d)
5.2786	-1.0099
5.6839	-0.8029
5.9718	-0.6598
6.1948	-0.5434
6.8880	-0.1913

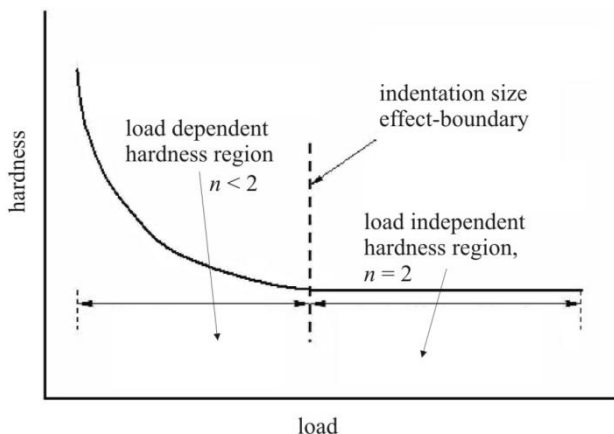


Figure 2. Meyer index [3]

2.4. Results - Meyer law

The most common interpretation of the load on the hardness, according to the professional literature, is directly connected with the structural factor of the material. Meyer proposed an empirical relationship between the applied load F and the size of the print d . This relationship is commonly called Meyer’s law. Measure of the impact of load on the hardness is the coefficient n . The parameters were obtained from the logarithmic dependency of hardness on the display diagonal (Figure 3). Figure 3 represents the slope of Meyer index n , and the ordinates axis intercept represents the $\log(k)$.

The resulting linear relationship indicates that Meyer’s model is suitable to describe the impact of load on the hardness of 42CrMo4 steel ($R^2 = 1.00$).

Parameter values k are determined by linear regression analysis and amount (Figure 3):

$$b = \log(k) = 7.1647 \tag{11}$$

$$n = 1.9662$$

(12)

$$R^2 = 1.00$$

(13)

The resulting function is:

$$y = 1.9662 \cdot x + 7.1647 \tag{14}$$

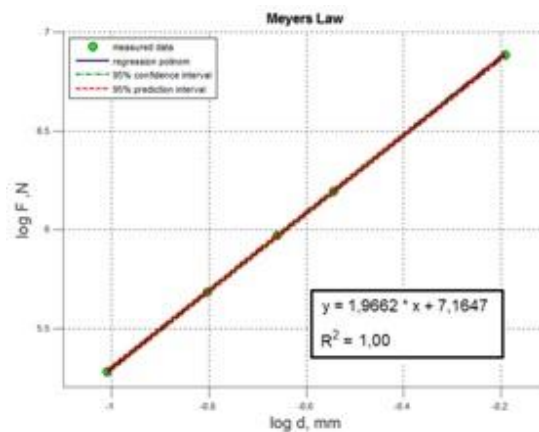


Figure 3. F-d correlation according to Meyer’s law

The resulting value of Meyer’s index n is less than 2 ($n=1.9662$) and therefore indicates that the applied load affects the hardness of the tested material (Figure 2).

2.5. Polynomial regression - PSR model

As an alternative to Meyer's law we also used model of resistance proportional to the properties of the sample (PSR) model.

PSR model was developed by the researchers Li and Bradt [3]. In this model, applied load F and print size d are connected in mathematical expression of the form:

$$F = a_1 d + a_2 d^2 \quad (15)$$

In the above equation a_1 and a_2 are coefficients that are related to the apparent hardness of the sample hardness (plasticity). a_1 is in the unit of N/mm, and a_2 in N/mm². The parameters a_1 and a_2 can be assessed from the linear - regression analysis of the relationship $F-d$, but it is necessary to linearize the mathematical function:

$$F = a_1 d + a_2 d^2 \quad (16)$$

$$F/d = a_1 + a_2 d \quad (17)$$

$$y = \frac{F}{d} \quad (18)$$

$$b = a_1 \quad (19)$$

$$a \cdot x = a_2 \cdot d \quad (20)$$

$$y = ax + b \quad (21)$$

Once the function is linearized it is necessary to code the measured data, or adjust them to the new linearized model as well as in the application of Meyer's law.

Table 4. Example of coding data for PSR model

$F/d, \text{N/mm}$	d_{SR}, mm
1.5656	0,3643 ± 0,0063
0.8499	0,4480 ± 0,0046
0.9566	0,5170 ± 0,0065
1.0569	0,5808 ± 0,0118
1.5563	0,8259 ± 0,0056

2.6. Results - PSR model

The parameters a_1 and a_2 are obtained from the display depending on the size of the Vickers pyramid diagonal (Figure 4). The slope represents the parameter a_2 and section on the vertical axis is represented by the parameter a_1 .

The resulting linear relation indicates that the PSR model is suitable for describing the impact of load on the hardness of 42CrMo4 steel ($R^2 = 0.99$).

The values of the parameters a_1 and a_2 are determined by linear regression analysis (Figure 4):

$$a_1 = 28.7069 \quad (22)$$

$$a_2 = 1403.9693 \quad (23)$$

$$R^2 = 0.99 \quad (24)$$

The resulting function is:

$$y = 1403.9693 \cdot x + 28.7069 \quad (25)$$

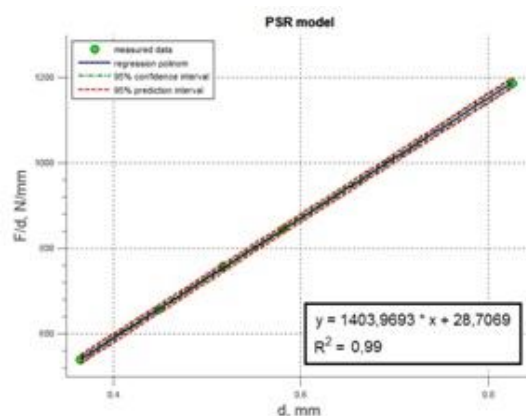


Figure 4. $F-d$ correlation according to PSR model

Conclusion

For the quantitative determination of the load impact on the hardness, two suitable mathematical models were used - Meyer's law and a model of resistance proportional to the properties of the sample. The calculated value of correlation coefficient $R^2 = 1.00$ clearly indicates that Meyer's law can be applied for the purpose of quantitative determination of the impact load on the hardness of 42CrMo4 steel manufactured by metal injection molding process. The resulting value of Meyer's index is $n = 1.9662$, and is less than 2, which indicates that the applied load affects the measured hardness of the material.

References

- [1] D. F. Heaney, "Handbook of metal injection molding", Woodhead Publishing Limited, 2012.

[2] A. Islam, N. Giannakas, D.M. Marhöfer et al. Proceedings of the 4M/ICOMM2015 Conference, March 30- April 2nd, 2015 Milano, Italy.

[3] H. Li, R. C. Bradt, J. Mater. Sci. 28 (1993) 917.

[4] <http://www.steelnumber.com>, 05.05.2016.

[5] I. Pantelić, "Uvod u teoriju inženjerskog eksperimenta" "Introduction to the Theory of Engineering Experiment" Prosveta, Novi Sad 1976.

[6] S. Sebastian, M. A. Khadar, J. Mater. Sci. 40 (2005) 1655.

[7] O. Sahin, O. Uzun, U. Kolemen, N. Ucar, Mater. Characterization, 58 (2007) 197.

Study of PVDF/PMMA blend resistance to artificial aging and neutral spray

F. Z. Benabid ^{a,*} and F. Zouai ^b

^a*LMPMP, Faculté de Technologie, Université Sétif-1, Algérie*

^b*Unité de Recherche Matériaux Emergents, Université Sétif-1, Algérie*

fzbenabid@yahoo.fr

Received date: Mars 21, 2016; accepted date: June 25, 2016

Abstract

The resistance of poly (vinylidene fluoride)/poly (methyl methacrylate) (PVDF/PMMA) blends was investigated using the artificial aging and neutral salt spray tests. The solution of each polymer was prepared using the N, N-dimethylformamide (DMF) as a solvent for the two polymers. The PVDF/PMMA blend is a compromise of a great development in the field of architectural preservation, since it is the best method in term of quality and price to make new polymeric materials having enhanced properties. The addition of PVDF to PMMA enhances the properties of this last to know the exhibition in the natural and artificial ageing and to the saline fog. The results showed that the exposure of coatings to artificial aging and to the salt water vapors showed a high resistance of the blend at compositions ≥ 70 of PVDF/PMMA.

Keywords: PVDF, PMMA, coating, artificial aging, neutral salt spray.

1. Introduction

Materials have always defined the level of development of our civilization [1], among other polymeric materials that have shaken much the habits of industry and those of consumers that the time since the eighties, the global production of plastics exceeds in volume that of metals.

Today, polymeric materials are present in all areas of human activity [2], from the packaging to the interplanetary rocket; among their various applications include the restoration and preservation of historical monuments (ruins, sculptures, paintings...).

In general, the fluorine substitution of the hydrogen atoms present in a macromolecular chain improves the heat resistance and chemical resistance, delays or inhibits flame propagation, lowering the critical surface tension and exalts the dielectric characteristics.

However, the stability of fluoropolymers is the key factor in their usual performance [3]. Acrylic resins undergo deterioration face conditions under UV radiation [4]; therefore their use as agents for the protection of stone is limited. Their climatic exposure

causes degradation of their structure as well as serious damage to the stone.

For this reason, acrylic resins are now less used in the conservation of historic structures exposed to atmospheric agents. However, their physical characteristics and their low price always consider an important research topic in the protection of the stone. On the other hand, the fluoropolymers present a good chemical inertness and well UV resistance [5].

In our work, the focus was on the development of films based blends of PVDF and PMMA who underwent exposure to artificial weathering and salt spray. The PMMA has a good optical property and rigidity; this is the best organic glass. It can easily be colored, as used as safety glass for aircraft (transparent domes) and as optical glass [6].

2. Experimental

PVDF designated Hylar 5000, special coating as a white powder, manufactured by Ausimont, Italy was used as received. PMMA designated Vedril ® Spa (Resina Metacrilica) made by Mont Edison, Italy was used as received. The PVDF/PMMA films were obtained by casting each polymer separately in the

DMF at 70°C at different weight contents (0, 10, 20, 30, 40, 50, 60, 70, 80, 90 and 100 wt %).

Exposure of coatings to artificial aging (fluorescent UV and water) according to standard ISO 11507: 1997 (E):

Artificial aging of the paint coating and subjected to condensation to ultraviolet fluorescent lamps is performed to obtain a degree of modification of one or more properties, after a light exposure or a mutually agreed upon total number of hours test. An accelerated Weathering Tester Q. PANEL COMPANY as test chamber was used. Ultraviolet light is emitted from a UV mercury arc lamp, low pressure with wavelengths between 270 and 400 nm, alternating cycles and 4 hours. Knowing that a cycle contains 500 hours and is equivalent to an outdoor exposure (natural aging) a year; and a temperature of up to 50 ° C.

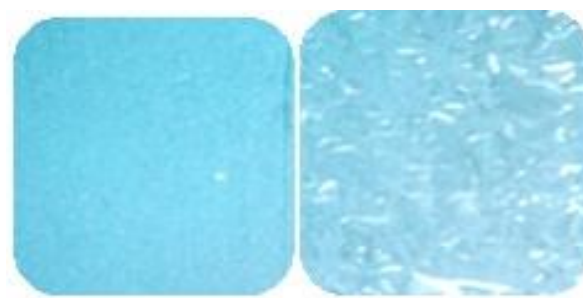
Resistance determination to neutral salt spray test according to ISO7253: 1996(E):

The test solution should be prepared by dissolving sodium chloride in water as defined in ISO 3696 to give a concentration of (50 ± 5) g.m⁻³. The measured temperature inside the spray chamber should be (35 ± 2) ° C; with a heating temperature of 55 ° C. The average recovery rate of the sprayed solution, measured over a minimum period of 24 h is 1 ml per hour to a horizontal collector surface area of 80 cm².

3. Results and discussion

Coatings Exposure to the artificial aging

The table 1 shows the variation the artificial aging resistance of the different compositions of the PVDF / PMMA blend, it is noted that the PVDF (100/0) film exhibits an excellent resistance to accelerated aging on a period of two years (> 17,000 hours) at 50 ° C and an UV radiation between 270 and 400 nm; and the same for 90 /10, 80/20 and 70/30 compositions. The PMMA (0/100) film has cracked and the resistance of the other of compositions was good, medium and bad one.



(a)

(b)

Figure1. Artificial aging resistance of the different compositions of the PMMA; (a) Reference film, (b) Film after exposure to artificial ageing.



(a)

(b)

Figure2. Artificial aging resistance of the different compositions of the PVDF; (a) Reference film (b) Film after exposure to artificial ageing

Table 1. Artificial aging resistance of various compositions of PVDF /PMMA blends

PVDF (%)	0	10	20	30	40	50	60	70	80	90	100
Film resistance	5	4	4	2	2	2	3	1	1	1	1

1 Excellent film resistance, 2 Good film resistance, 3 Medium film resistance, 4 Bad film resistance and 5 Film cracking.

Coating exposure to the neutral saline fog

Table 2 shows the variation of neutral saline fog as a function of different compositions of PVDF/PMMA blends, it is observed that pure PVDF samples give an excellent film resistance to the saline vapors under a pressure of 70 to 170 KPa at 35°C. The same results are also available for 90/10, 80/20 and 70/30 PVDF/PMMA fractions.

Pure PMMA films (0/100) present a medium resistance. Regarding the remaining compositions, the

resistance evaluation varies between good, medium, bad and total corrosion of the plate.

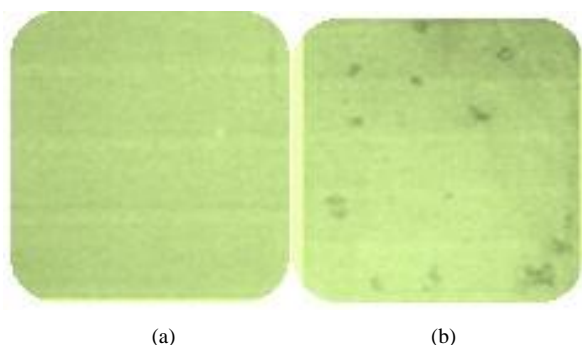


Figure3. Neutral saline fog resistance of the different compositions of the PMMA; (a) Reference film, (b) Film after exposure to neutral saline fog

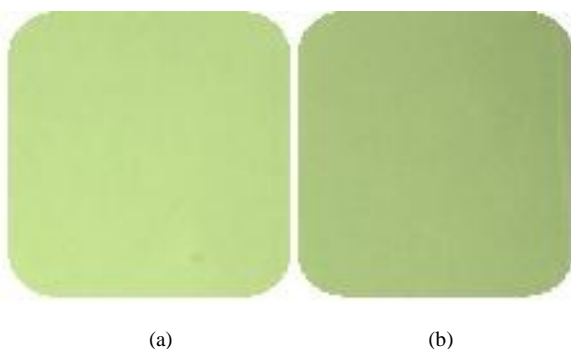


Figure4. Neutral saline fog resistance of the different compositions of the PVDF; (a) Reference film, (b) Film after exposure to neutral saline fog

Table 2. Resistance to neutral saline fog at different compositions of PVDF/PMMA blends.

PVDF (%)	0	10	20	30	40	50	60	70	80	90
Film resistance	3	4	5	4	3	2	3	1	1	1

1 Excellent film resistance, 2 Good film resistance,
 3 Medium film resistance, 4 Bad film resistance
 (plate corrosion) and 5 Total plate corrosion.

Conclusion

From the different results obtained, it can be concluded that:

- The exposure of coatings to artificial aging (fluorescent UV and water) showed a high resistance of the blend at compositions ≥ 70 of PVDF/PMMA.
- The coating exposure to the neutral saline fog showed that the PVDF has an excellent resistance to salt water vapors at compositions ≥ 70 of PVDF/PMMA.

References

[1] Lu, D. R., Xiao, C. M. and Xu, S. J., Starch-based completely biodegradable polymer materials, *eXPRESS Polymer Letters*, 2009, 3, 366-375.
 [2] Pawar, P.A. and Purwar, A.H., Biodergradable Polymers in Food Packaging, *American Journal of Engineering Research (AJER)*, 2013, 2, 151-164.
 [3] Boz, E., Nemeth, A. J. and Wagener, K. B., Well-Defined Precision Ethylene/Vinyl Fluoride Polymers: Synthesis and Crystalline Properties, *Macromolecules*, 2008, 41, 1647-1653
 [4] Radvan, R., Cortea, I. M., Ene, D. and Radvan, A., Contemporary Art Materials Tests, *International Journal of Conservation Science*, 2013, 4, 613-620.
 [5] Teng, H., Overview of the Development of the Fluoropolymer Industry, *Appl. Sci.*, 2012, 2, 496-512.
 [6] Dorrnian, D., Abedini, Z., Hojabri, A. and Ghoranneviss, M., Structural and Optical Characterization of PMMA Surface Treated in Low Power Nitrogen and Oxygen RF Plasmas, *Journal of Non-Oxide Glasses*, 2009, 1, 217 - 229.

Electronic structure and Fano's antiresonance study of Cr³⁺ doped BIGaZYTZr fluoride glass

Hajer Souissi¹, Olfa Taktak¹, Olfa Maalej² and Souha Kammoun¹

¹Laboratoire de Physique Appliquée, Groupe de Physique des Matériaux Luminescents, Université de Sfax, Faculté des Sciences de Sfax, BP 1171, 3000, Sfax, Tunisia.

²Laboratoire de Chimie Inorganique, Université de Sfax, Faculté des Sciences de Sfax, BP 1171, 3000, Sfax, Tunisia.
souissi_hajer_fss@yahoo.fr

Received date: May 06, 2016; revised date: June 28, 2016; accepted date: June 28, 2016

Abstract

The absorption spectrum of Cr³⁺ in BIGaZYTZr (30BaF₂-18InF₃-12GaF₃-20ZnF₂-10YF₃-6ThF₄-4ZrF₄) fluoride glass is characterized by the presence of features on the ⁴T_{2g}(F) absorption band. These features result from interaction of the ²E_g(²G) and ²T_{2g}(²G) sharp levels with the vibrationally broadened ⁴T_{2g}(F) quasi-continuum via spin-orbit coupling. We have analyzed this phenomenon in the frame of the Fano's antiresonance model. This analysis permits us to determine the electronic structure of the chromium ion Cr³⁺ by the crystal field theory. A good agreement between the theoretical and the experimental energy levels are obtained. The fitted parameters by Fano's antiresonance model and the crystal field parameters obtained in this work are compared with those of homologous fluoride glasses.

Keywords: Crystal field, transition-metal, fluoride glass, interference dip, Fano's antiresonances.

1. Introduction

Considerable interest has been devoted to fluoride glasses, particularly heavy metal fluoride glasses. The optical properties of fluoride glasses are important for accurately designing optical systems, optical fiber waveguides, fiber lasers and amplifiers [1-5]. Furthermore, the ease of preparation, high concentrations of transition-metal ions can be incorporated into these matrices. These doping ions present favorable spectroscopic properties. Cr³⁺ doped glasses have attracted much attention over the past few years because of applications to lasers [6] and solar concentrators [7]. The states of transition metals in host glasses are known to be influenced by several parameters such as type and glass composition.

The optical absorption spectrum of Cr³⁺ doped BIGaZYTZr (30BaF₂-18InF₃-12GaF₃-20ZnF₂-10YF₃-6ThF₄-4ZrF₄) fluoride glass was measured by Elejalde *et al.* [8]. This spectrum consists of broad absorption bands with the presence of features which are attributed to the d-d transitions of the active center Cr³⁺

with 3d³ configuration. It is approved that in most glasses, Cr³⁺ ions occupy sites having nearly perfect octahedral symmetry because of the strong ligand field stabilization energy of Cr³⁺ in six-fold coordination [9].

In this paper, we are interested in studying the absorption spectrum of Cr³⁺ doped BIGaZYTZr fluoride glass. In the first part, we give a qualitative study of the interaction between quartet ⁴T_{2g}(F) and doublet ²E_g(²G) excited levels via spin-orbit coupling by using the notion of adiabatic potential energy surfaces. In the second part, we concentrated our study on the features observed at the long wavelength ⁴A_{2g}(F) → ⁴T_{2g}(F) absorption band of Cr³⁺ doped BIGaZYTZr. These features have been analyzed by Fano's antiresonance model [10-11]. Finally, we present a detailed crystal-field analysis of the electronic energy levels of Cr³⁺:BIGaZYTZr based on the Racah theory. This theoretical analysis leads to the Racah and crystal-field parameters for this ion. The splitting of the Stark levels under spin-orbit interaction is also considered. By comparison with other fluoride glasses, we tried to deduce informations such as the intensity of the crystal-field on Cr³⁺ ion (from Dq parameter) as a

function of the glass composition, the disorder in these glasses, etc....

2. Experimental Support

The spectroscopic properties of Cr^{3+} in BIGaZYTZr ($30\text{BaF}_2\text{-}18\text{InF}_3\text{-}12\text{GaF}_3\text{-}20\text{ZnF}_2\text{-}10\text{YF}_3\text{-}6\text{ThF}_4\text{-}4\text{ZrF}_4$) fluoride glass has been investigated by Elejalde *et al.* [8]. The optical absorption spectra measured by these authors will be used for the theoretical study of this article.

Figure 1 presents the room temperature absorption spectrum of Cr^{3+} (0.2 mol%) doped BIGaZYTZr fluoride glass. The absorption spectrum is characterized by two spin-allowed broad bands centered at 15391 and 22423 cm^{-1} , which are attributed respectively to the vibronically broadened transitions ${}^4\text{A}_g(\text{F}) \rightarrow {}^4\text{T}_g(\text{F})$ and ${}^4\text{A}_g(\text{F}) \rightarrow {}^4\text{T}_1(\text{F})$. The ${}^4\text{A}_g(\text{F}) \rightarrow {}^4\text{T}_g(\text{F})$ absorption band shows a fine structure due to the spin-forbidden ${}^4\text{A}_g(\text{F}) \rightarrow {}^2\text{E}_g(\text{G})$ and ${}^4\text{A}_g(\text{F}) \rightarrow {}^2\text{T}_1(\text{G})$ transitions.

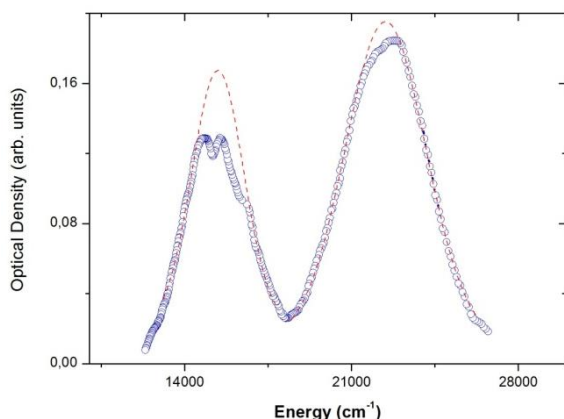


Figure 1. Optical absorption spectra of Cr^{3+} doped BIGaZYTZr fluoride glass (plotted line) at room temperature and fits to a Gaussian function (dashed line) [8].

3. Theoretical Background

The fine structure observed on the ${}^4\text{A}_g(\text{F}) \rightarrow {}^4\text{T}_g(\text{F})$ absorption band of Cr^{3+} doped BIGaZYTZr fluoride glass will be analyzed following the Fano's antiresonance model. Then, the electronic structure is determined by the crystal field theory which reposes on the Racah tensor algebraic methods. In this section, we remember briefly the Fano's antiresonance and crystal field theories.

3.1. Fano's antiresonance method

Antiresonances features are analyzed by means of the Fano's profile function $R(\omega)$. This function is obtained from the ratio of the experimental absorption spectrum to the background spectrum, the latter being obtained by fitting the wings of the experimental absorption spectrum with a Gaussian function. In the notation of Sturge *et al.*, the Fano's theory is provided as [12]:

$$R(\omega) = 1 + \sum_i \rho_i^2 \frac{q_i^2 + 2q_i\xi_i^2 - 1}{1 + \xi_i^2} \quad (1)$$

where:

$$\xi = \frac{\omega - \omega_{ri}}{\gamma_i}, \quad q_i = \frac{\langle \phi_i | z | \psi_0 \rangle}{\sqrt{\pi \gamma_i} \rho_i \langle \psi_{E_i}^{(d)} | z | \psi_0 \rangle}$$

$$\gamma_i = \pi \left| \langle \psi_{E_i}^{(a)} | H_i | \phi_i \rangle \right|, \quad \rho_i = \left| \langle \psi_{E_i}^{(a)} | \psi_{E_i}^{(d)} \rangle \right|$$

The index i ranges over the number of sharp levels (two in our case, $i=1$ for ${}^2\text{E}_g$ (${}^2\text{G}$) and $i=2$ for ${}^2\text{T}_1$ (${}^2\text{G}$)). Interactions between these sharp levels and the vibrationally broadened ${}^4\text{T}_g$ (F) are neglected. ϕ_i is the wave function of the sharp level in the absence of the interaction H_i with the continuum (spin-orbit in our case). Φ_i represents a modification of ϕ_i by the continuum and ψ_0 the ground state. z is the optical operator (electric or magnetic dipole). $\psi_{E_i}^{(a)}$ and $\psi_{E_i}^{(d)}$ arise, respectively, by auto-ionisation of ϕ_i and by direct transition from ground state ψ_0 .

The four parameters ρ_i^2 , γ_i , q_i and ω_{ri} are to be fitted. The parameter ρ_i^2 gives the fraction of the band states that take part in the interference process. γ_i indicates the spectral width of the sharp state (${}^2\text{E}_g$ or ${}^2\text{T}_1$). q_i is a numerical index which characterizes the line profile. A value of q_i close to zero corresponds to a "true" antiresonance. Finally ω_{ri} is the resonance energy which is slightly shifted due to the interaction with the continuum, compared to the resonance energy for the unperturbed sharp absorption line.

3.2. Crystal field study of the Cr^{3+} in phosphate glasses

The total Hamiltonian of a $3d^N$ ion in an arbitrary symmetry site is written as [13,14]:

$$H = H_0 + H_{\text{free}} + H_{\text{CF}} + H_{\text{so}} \quad (2)$$

H_0 is the Coulomb interaction including electron-electron repulsions. This Hamiltonian gives the $2s+1L$ terms: two quartet terms (4F ground state and 4P excited state) and six doublet excited terms (2H , 2G , 2F , 2D , 2D and 2P) for Cr^{3+} with a $3d^3$ configuration. The eigenvalues of Hamiltonian H_0 are expressed as a function of the Racah parameters B and C [13,15]. H_{Tres} is the Trees correction describing the two-body orbit-orbit polarization interaction (α is the Trees parameter) [16,17]. H_{so} is the spin-orbit (SO) coupling (ζ is the one electron SO parameter). H_{CF} is the crystal field Hamiltonian, which is represented for octahedral symmetry O_h in the Wybourne's notation by the following [18,19]:

$$H_{CF} = B_4^{oct} \left[C_0^{(4)} + \sqrt{\frac{5}{14}} (C_0^{(4)} + C_{-4}^{(4)}) \right] \quad (3)$$

B_4^{oct} is the octahedral CF parameter and C_q^k are the Racah tensor operators. The matrix elements of C_q^k operators are calculated numerically by the Racah algebraic methods [20], whereas the Racah parameters B and C, the Trees parameter α , the crystal field parameter B_4^{oct} , and the one electron SO parameter ζ have to be determined from the optical spectra. The parameter Dq , characteristic of transition metals, shows the crystal field strength and is related to the B_4^{oct} parameter by the relation: $10Dq = 21 B_4^{oct}$.

The spin-orbit coupling term ζ is related to racah parameters B and C by the relation [21]:

$$\zeta = N^2 \zeta_0 \quad \text{with} \quad N^2 = \frac{1}{2} \left(\sqrt{\frac{B}{B_0}} + \sqrt{\frac{C}{C_0}} \right) \quad (4)$$

$B_0 = 918 \text{ cm}^{-1}$ and $C_0 = 3850 \text{ cm}^{-1}$ are the Racah parameters and $\zeta_0 = 273 \text{ cm}^{-1}$ is the spin-orbit coupling coefficient of the free Cr^{3+} ion [22].

Since, the crystal-field is of the intermediate strength for $3d^N$ transition ions of the first series in crystals, [13,15,18] the basis functions $\{d^N L S M_L M_S\}$ in the LS-coupling scheme have been adopted in our computer package. As a part of a larger project, we have set to develop a crystal field analysis computer program based on MAPLE software to calculate the energy levels and state vectors for any transition metal ion with the $3d^N$ configuration ($N = 2, 3, 7, 8$) located at sites with symmetry given by any of the 32 crystallographic point groups. This computer program has been tested and has given the same results as the one of Y. Yeung and C. Rudowicz [23].

4. Results And Discussion

The absorption spectrum of Cr^{3+} in BIGaZYTZr glass shows features due to the interaction between the ${}^3E_g(G)$ and ${}^3T_{1g}(G)$ sharp levels and the vibrationally ${}^3T_{2g}(F)$ quasicontinuum. The interactions between states of different spin multiplicities lead to interference dips. In this section, we first explain the origin of these dips in the model of adiabatic potential energy surface. Then, we analyze these features according to the Fano's antiresonance theory. Finally, we determine the electronic structure of Cr^{3+} in BIGaZYTZr by using the crystal field theory.

4.1. Adiabatic potential energy surface used to explain the interference dips

To explain the origin of the interference dips, we use the notion of adiabatic potential energy surfaces. In this model, we characterize the interference between the quartet ${}^3T_{2g}(F)$ and the doublet ${}^3E_g(G)$ excited states because it is an obvious dip in the absorption spectrum of Figure 1. We have not taking into account the interaction with the ${}^3T_{1g}(G)$ excited state because the values of the parameters that describe the interference dip for this state are more inaccurate due to the contribution from the ${}^3T_{1g}(F)$ excited state. The origin of the Fano's antiresonance is explained by the spin-orbit coupling between the two states ${}^3T_{2g}(F)$ and ${}^3E_g(G)$ [10-11]. In this qualitative study, each harmonic potential is defined along a single normal coordinate Q with its frequency \mathbf{k} in wavenumber units. The position of the potential minimum and the vibrational frequency for the ${}^3E_g(G)$ state are identical to the ground state potential minimum ${}^4A_g(F)$, set to $Q=0$. This doublet state is not displaced along the normal coordinate because the electronic transition corresponds to an intra-configurational d-d excitation [24-27]. The position of ${}^3T_{2g}(F)$ minimum is displaced along Q by an amount ΔQ and we consider its vibrational frequencies to be identical to those on the ground and doublet excited states. This quartet state surface is displaced to longer metal-ligand bond distances because the d-d excitation populates metal-ligand antibonding molecular orbitals [24-27]. The magnitude of the displacement ΔQ is determined from the width of the spin-allowed absorption band in the experimental spectrum. $E({}^3E_g)$ and $E({}^3T_{2g})$ are the energy of the potential minimum for ${}^3E_g(G)$ and ${}^3T_{2g}(F)$ states respectively. The potentials for the two excited states in the absence of spin-orbit coupling are given by :

$$V(^2E_g) = V_1 = \frac{1}{2}(k Q^2) + E(^2E_g) \quad (5)$$

$$V(^4T_{2g}) = V_2 = \frac{1}{2}(k(Q - \Delta Q)^2) + E(^4T_{2g}) \quad (6)$$

If we take into account the spin orbit coupling, the quartet excited state ${}^4T_{2g}(\text{F})$ is split into four levels ($2G$, E_+ and E_-) and the doublet excited state just undergoes a displacement (G). The corresponding uncoupled potentials are called diabatic potentials. The interaction between the same symmetry levels (G) deriving from electronic states of different multiplicities leads to the observed spin-forbidden transition from ${}^4A_{2g}(\text{F})$ ground state to ${}^2E_g(\text{G})$ excited state. Effectively, the ${}^4T_{2g}(\text{F})$ and ${}^2E_g(\text{G})$ diabatic potentials are coupled by a constant V_{12} which its magnitude is on the order of the spin-orbit coupling constant ζ . These coupled potentials are called adiabatic potentials and are obtained by diagonalizing the following 2×2 potential matrix:

$$V(^2E_g, ^4T_{2g}) = \begin{pmatrix} V(^2E_g) & V_{12} \\ V_{12} & V(^4T_{2g}) \end{pmatrix} \quad (7)$$

The adiabatic potentials are given by the following expression [34]:

$$V_+ = \frac{1}{2} \left[(V_1 + V_2) + \sqrt{(V_1 - V_2)^2 + 4V_{12}^2} \right] \quad (8)$$

$$V_- = \frac{1}{2} \left[(V_1 + V_2) - \sqrt{(V_1 - V_2)^2 + 4V_{12}^2} \right] \quad (9)$$

where V_+ and V_- are the upper and lower adiabatic potentials. The adiabatic excited state surfaces are shown as solid lines and the dotted curves corresponding to the diabatic excited state potential energy as illustrated in Figure 2. The consideration of the spin orbit coupling between ${}^2E_g(\text{G})$ and ${}^4T_{2g}(\text{F})$ leads to the adiabatic excited state potential energy curves V_+ and V_- which are responsible of the spin-allowed

${}^4A_{2g}(\text{F}) \rightarrow {}^4T_{2g}(\text{F})$ and the spin-forbidden ${}^4A_{2g}(\text{F}) \rightarrow {}^2E_g(\text{G})$ transitions and permit us to explain the interference dip.

4.2. Fano's antiresonance study of ${}^4T_{2g}(\text{F})$, ${}^2E_g(\text{G})$ and ${}^2T_{1g}(\text{G})$ states

The study of the interference dips can be made according to the Fano's antiresonance theory presented by Sturge *et al.* and Lempicki *et al.* [12,28].

The Fano's profile function $R(\omega)$ is obtained from the ration of the experimental absorption spectrum to the background spectrum, the latter calculated by fitting the wings of the spectrum by a single Gaussian function. Figure 1 shows the results of the Gaussian fit. The $R(\omega)$ curve and its fit from Eq. 1 is represented in Figure 3. The fitted parameters ρ_i^2 , q_i , γ_i and ω_i ($i=1$ for ${}^2E_g(\text{G})$ state and $i=2$ for ${}^2T_{1g}(\text{G})$ state) listed in Table 1. It can be observed that the Fano's antiresonances parameters obtained in this study are compatible with the result obtained by Illaramendi *et al.* for homologous fluoride glasses [29].

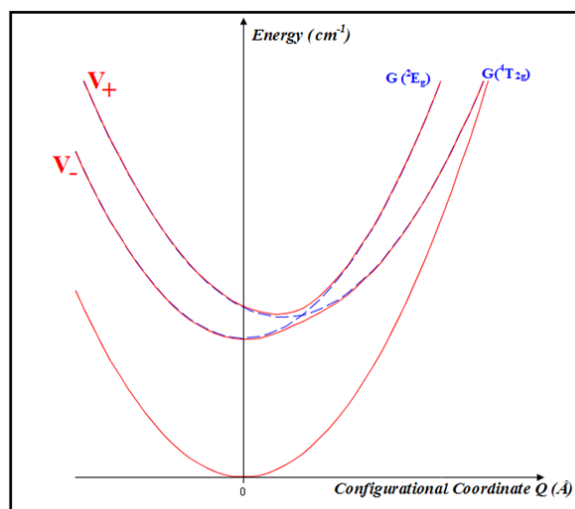


Figure 2. Potential energy curves for the ${}^4T_{2g}(\text{F})$ and ${}^2E_g(\text{G})$ excited states. The diabatic and adiabatic potentials for these electronic states are shown by dashed and solid lines respectively.

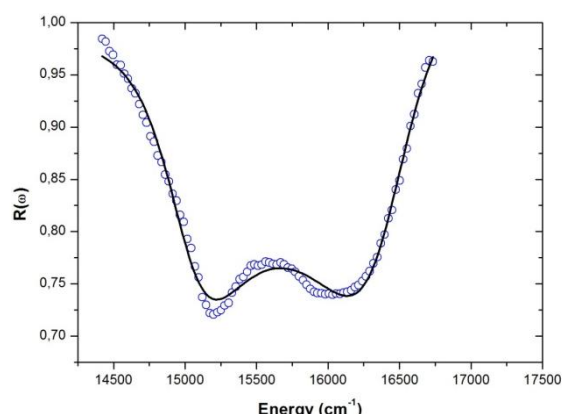


Figure 3. Experimental Fano's antiresonances profile (plotted line) and fits to Eq.1 (solid line) for Cr^{3+} doped BIGaZYTzr fluoride glass.

Table 1. Parameters of ${}^2E_g(^2G)$ and ${}^2T_{1g}(^2G)$ antiresonances for Cr^{3+} : BiGaZYTZr and comparison with homologous glasses.

	Parameter	Cr^{3+} : BiGaZYTZr	Cr^{3+} : BiGaZYT [31]	Cr^{3+} : BIZYT [31]
2E_g	ρ_1^2	0.17	0.28	0.23
	q_1	-0.39	-0.219	-0.148
	$\gamma_1(\text{cm}^{-1})$	376	336	292
	$\omega_{1r}(\text{cm}^{-1})$	15 036	15 245	15 227
${}^2T_{1g}$	ρ_2^2	0.20	-	-
	q_2	0.52	-	-
	$\gamma_2(\text{cm}^{-1})$	450	-	-
	$\omega_{2r}(\text{cm}^{-1})$	16 406	-	-

Table 2. Crystal field, Racah, trees and spin-orbit coupling parameters values for Cr^{3+} -doped BiGaZYTZr fluoride glass.

Material	Dq (cm^{-1})	B (cm^{-1})	C (cm^{-1})	B_4^{oct} (cm^{-1})	α	ζ (cm^{-1})
Cr^{3+} : BiGaZYTZr ^a	1540	787	3 045	32 340	70	248

The value obtained for ρ^2 parameter can be related to the larger disorder in glasses [28] which produces a more complete mixing of the spin-orbit components of the ${}^2T_{2g}(^2F)$ with components of ${}^2E_g(^2G)$ and ${}^2T_{1g}(^2G)$. The q parameter, ranging from $-\infty$ to $+\infty$, characterizes the line shape. The small value obtained for q indicates that the antiresonance is produced by a sharp forbidden transition overlapping with a broad allowed band. The value of γ indicates an inhomogeneous broadening of the transition due to the presence of several environments in the glass. The last fitted parameter, ω_r , quantifies the position of the antiresonance in absorption and permits an estimation of the shift of the sharp levels due to coupling with the quasi-continuum. If we compare the values of ρ^2 , it can be seen that the BiGaZYTZr fluoride glass has the smallest value and consequently should be the most ordered glass. The values of the antiresonance linewidths γ are influenced by the inhomogeneous broadening due to the presence of several environments in the glasses. The last fitted parameters,

ω_{r1} and ω_{r2} , quantify the position of the antiresonances in absorption.

From the energy position of ${}^2T_{2g}(^2F)$, ${}^2E_g(^2G)$, ${}^2T_{1g}(^2G)$ and ${}^2T_{1g}(^2F)$ levels obtained by the Fano's antiresonance study we can performed the crystal field analysis on Cr^{3+} doped in BiGaZYTZr.

4.3. Crystal field study of the absorption spectrum of Cr^{3+} : BiGaZYTZr

The theoretical energies chromium Cr^{3+} : BiGaZYTZr are obtained by diagonalizing the full 120×120 matrix associated to the Hamiltonian of Eq. 1 in the free ion eigenstates $|LSM_LM_S\rangle$ within the quartet terms (4F ground state and 4P excited state) and doublet excited terms (2H , 2G , 2F , 2D_a , 2D_b and 2P). These energies are function of the B, C, α , B_4^{oct} and ζ parameters. From the absorption spectrum of Figure 1, we determine the $10Dq$ crystal field strength, it represents the difference between the excited state ${}^2T_{2g}(^2F)$ and the ground state ${}^4A_g(^2F)$. The crystal field

parameter B_4^{oct} is then deduced from the value of $10Dq$ [13,30]. The Racah parameters B is obtained from the observed quartet state ${}^4T_{1g}({}^4F)$.

The spin-orbit coupling term ζ is calculated from the Racah parameters B and C by Eq. 5. The Racah parameter C , the Trees correction α and parameters are adjusted using the Newton Raphson method to minimize the difference between the calculated and the observed ${}^3E_g({}^3G)$ energy levels. The spin orbit parameter ζ is introduced in our computer package in order to obtain the splitting of the Stark levels of the O_h site symmetry. The set of calculated parameters B , C , B_4^{oct} , Dq , α and ζ listed in Table 2 permit as to deduce the calculated energy levels reported in Table 3. The calculated and the experimental energies are in good agreements.

The electrostatic crystal field theory deals only with the d orbitals. The molecular orbitals are in reality influenced by the interaction between the ligand's s and p orbitals and the d orbitals of the central ion. The admixture of these orbitals leads to the s, σ and π bondings between the Cr^{3+} impurity ion and F ligands. Thus, the $10Dq$ parameter obtained from absorption spectra of Figure 1 contains the two contributions : the crystal field measure and also comprises the admixture of the antibonding e_g and t_{2g} orbitals with s and p ligand orbitals. The $10Dq$ parameter strongly depends upon the metal-ligand distance. The Racah parameters B and C are reduced compared to the free ion due to covalency effects.

The Tanabe-Sugano diagrams for Cr^{3+} ion in octahedral symmetry site of Figure 4 is drawn with the Racah parameters B and C of Table 1 ($C/B=3.88$). It indicates the general behavior of Cr^{3+} ion energy levels as a function of the local field strength measured in terms of Dq/B . The vertical line represents the appropriate value for Dq/B found for Cr^{3+} in BiGaZYT. From this diagram, we remark also that the ${}^4T_{2g}({}^4F)$ quartet state and the $({}^2E_g({}^2G), {}^2T_{1g}({}^2G))$ doublet states are near for the calculated parameters Dq , B and C . This shows a strong coupling between the electronic states of different multiplicities. All these excited states are subdivided into E_1 , E_2 and G states by spin-orbit coupling (Figure 5).

The interaction between the same symmetry levels (E_1 , E_2 or G) deriving from electronic states of different multiplicities leads to the observed spin-forbidden transitions from the ${}^4A_{2g}({}^4F)$ ground state to the ${}^2E_g({}^2G)$ and the ${}^2T_{1g}({}^2G)$ excited states (O_h symmetry) with lower intensity compared to a spin-allowed transition (Figure 5).

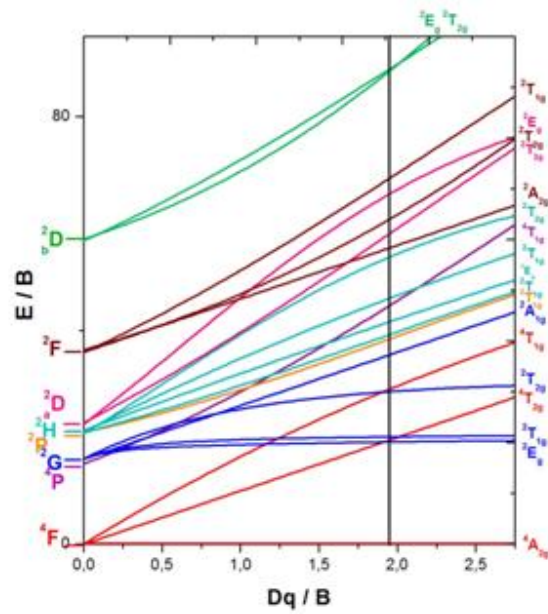


Figure 4. Tanabe-Sugano diagram for octahedrally coordinated Cr^{3+} ion with $C/B=3.88$. The vertical line represents the case of Cr^{3+} in BiGaZYTzr fluoride glass.

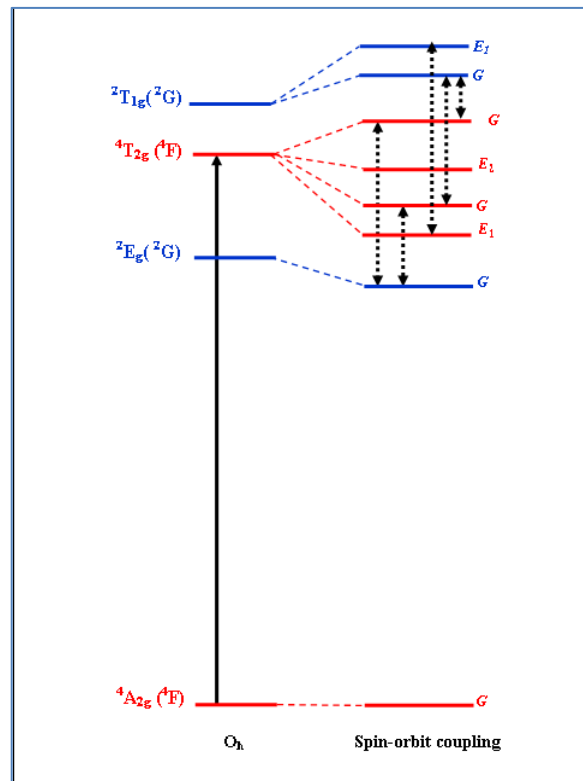


Figure 5. Electronic states of ${}^4T_{2g}({}^4F)$, ${}^2E_g({}^2G)$ and ${}^2T_{1g}({}^2G)$ of Cr^{3+} in BiGaZYTzr fluoride glass. Solid arrows denote spin-allowed transition. Dotted arrows connect pairs of interacting levels under spin-orbit coupling.

Table 3. Experimental and calculated energies (cm⁻¹) of Cr³⁺ occupying a O_h symmetry in BiGaZYTZr fluoride glass (the "-" signifies that the states are not visible).

O _h	Cr ³⁺ : BiGaZYTZr			mul*
	E _{obs}	E _{cal} * [this work]	E ^a _{cal} * [this work]	
⁴ A _{2g} (⁴ F)	0	0	0	4
² E _g (² G)	15 036	15 268	15 036	4
⁴ T _{2g} (⁴ F)	15 391	15 400	15 303	2
			15 365	4
			15 422	2
			15 653	4
² T _{1g} (² G)	16 406	16 029	16 030	4
			16 122	2
			16 122	2
² T _{2g} (² G)	-	22 193	22 048	2
			22 050	4
⁴ T _{1g} (⁴ F)	22 423	22 422	22 454	4
			22 514	2
			22 530	4
			22 637	2
			22 637	2
² A _{1g} (² G)	-	28 243	28 262	2
² T _{1g} (² P)	-	30 887	30 853	2
			30 908	4
² T _{1g} (² H)	-	31 239	31 112	2
			31 292	4
² E _g (² H)	-	32 777	32 776	4
⁴ T _{1g} (⁴ P)	-	34 883	34 882	4
			34 887	2
			34 908	4
			34 913	2
			34 913	2
² T _{1g} (² H)	-	36 151	36 130	2
			36 240	4
² T _{2g} (² H)	-	41 529	41 527	2
			41 548	4
² A _{2g} (² F)	-	43 423	43 435	2
² T _{2g} (² D _a)	-	46 661	46 610	2
			46 718	4
² T _{2g} (² F)	-	47 945	47 845	2
			48 024	4
² E _g (² D _a)	-	51 132	51 147	4
² T _{1g} (² F)	-	53 659	53 596	2
			53 711	4
² E _g (² D _b)	-	69 234	69 239	4
² T _{2g} (² D _b)	-	69 280	69 262	4
			69 416	2

* mul: multiplicity

*E_{cal}: means the energies without spin orbit coupling.

*E^a_{cal}: means the energies taking into account the spin-orbit coupling.

By comparing the crystal field strength Dq of Cr³⁺: BiGaZYTZr with those of homologous fluoride glasses of literature, we notice the decrease of the 10Dq parameter in the sense Dq(BIZYT) = 1550cm⁻¹ [31] > Dq(BiGaZYT) = 1548 cm⁻¹ [31] > Dq(BiGaZYTZr) = 1540 cm⁻¹. The intensity of the crystal field Dq depends on the distortion of the polyhedron formed glass structural network. As the distortion is important then the distance between Cr³⁺-F becomes large. Consequently, the crystal-field strength decreases. It is obvious that the value for Dq in glasses is determined primarily by the network structure glasses. In another way, the 10Dq parameter decreases as the number of fluoride ions increases. This suggests that this decrease results in larger Cr³⁺-F distances.

For transition metal, the spin orbit constant λ is related to the effective g factor obtained from Electron Paramagnetic Resonance (EPR) by the expression [32] :

$$g_{eff} = g_e - \frac{8\lambda}{\Delta} \quad (10)$$

Where : g_e = 2.0023 is the free electron factor, Δ is the gap between the excited and the ground levels (Δ = E(⁴T₂) - E(⁴A₂) = 10Dq).

The S-O coupling constant λ is connected to the one-electron S-O coupling constant ξ by the following relation [33]

$$\lambda = \pm \frac{\xi}{2S} \quad (11)$$

The sign + is valid for a layer less than half full and the sign - to a more than half-complete layer. For 3d³ electronic configuration (S=3/2), so we have ξ = 3λ.

From the theoretical values obtained by crystal Field analysis (Δ = 15400 cm⁻¹ and λ = ξ/3=83cm⁻¹), we find g_{eff} = 1.95918

5. Conclusion

The features observed on the ⁴T_{2g}(⁴F) absorption band of Cr³⁺ in BiGaZYTZr glass are due to the interaction between the ⁴E_g(⁴G) and ⁴T_{1g}(⁴G) sharp levels and the vibrationally ⁴T_{2g}(⁴F) quasicontinuum. The model of the adiabatic potential energy surfaces explain the origin of interaction between different spin multiplicities states via spin orbit coupling. These features leading to the interference dips have been analyzed by the Fano's antiresonance model exposed by Sturge et al and Lempicki et al. The fitted parameters involved in this model give information about the fraction of the quasicontinuum which takes part in the interference

process and the line shape profile of the antiresonance. From these parameters and by comparison with other fluoride glasses: BIZYT and BIGaZYT, we deduce that the most order glass is the BIGaZYTZr fluoride glass. The electronic structure of Cr^{3+} occupying O_h site symmetry in the BIGaZYTZr glasses has been analyzed using the crystal field theory. The estimated parameters B, C, Dq, α and ζ lead to a good agreement between the calculated and observed levels.

Acknowledgments

The authors are indebted to Prof. Brigitte Boulard from «**Institut des Molécules et Matériaux de Mans**» for her scientific support and her constructive recommendations.

References

- [1] M. M. Broer and L. G. Cohen, *J. Lightwave Technol.* 4 (1986) 1509-1513.
- [2] L. Reekie, R. J. Mears, S. B. Poole, and D. N. Payne, *J. Lightwave Technol.* 4 (1986) 956-960.
- [3] R. S. Quimby, M. G. Drexhage, and M. J. Suscavage, *Electron. Lett.* 23 (1987) 32-34.
- [4] D. C. Yeh, W. A. Sibley, M. Suscavage, and M. G. Drexhage, *J. Appl. Phys.* 62 (1987) 266-275.
- [5] M. G. Drexhage, in *Treatise on Materials Science and Technology*, edited by M. Tomozawa and R. H. Doremus (Academic, New York, 1985), pp. 151- 243.
- [6] P. T. Kenyon, L. J. Andrews, B. C. McCollum, and A. Lempicki, *IEEE J. Quant. Electron.* 18, (1982) 1189-1197.
- [7] R. Reisfeld, *Mater. Sci. Eng.* 71 (1985) 375-382.
- [8] M. J. Elejalde, R. Balda, J. Fernandez, and E. Macho, *Phys. Rev. B* 46 (1992) 5169-5182.
- [9] C. BenHamideche, A. Boutarfaia and M. Poulain, *J. of non-oxide glasses* 1 (2009) 261-265.
- [10] U. Fano *Phys. Rev.* 124 (1961) 1866-1878.
- [11] U. Fano and J. W. Cooper 1965 *Phys. Rev.* 137 A1361.
- [12] M. D. Sturge, H. J. Guggenheim, M. H. Pryce, *Phys. Rev. B* 2 (1970) 2459-2471.
- [13] S. Sugano, Y. Tanabe, H. Kamimura, *Multiplets of transition-metal ions in crystals* (Academic Press, New York, 1970).
- [14] J. S. Griffith, *The Theory of transition-metal ions* (Cambridge University Press, Cambridge, 1961).
- [15] R. C. Powell, *Physics of Solid-State Laser Materials* (1stEd. Springer-Verlag, New York, 1998) pp.215-233.
- [16] Z. Y. Yang, C. Rudowicz, and Y. Y. Yeung, *Physica B* 348 (2004) 151-159.
- [17] C. Rudowicz, Z. Y. Yang, Y. Y. Yeung, and J. Qin, *J. Phys. Chem. Solids* 64 (2003) 1419-1428.
- [18] D. J. Newman and B. Ng, *Crystal field Handbook* (1stEd. Cambridge University Press, 2000) pp.28-36.
- [19] B. G. Wybourne, *Spectroscopic Properties of Rare Earth*(1stEd. Wiley, New York, 1965)pp.48-234.
- [20] J. P. Elliott, B.R. Judd, W.A. Runciman, *Proc. R. Soc. London, Ser. A* 240 (1957) 509-523.
- [21] M. G. Zhao, J. A. Xu, G. R. Bai and H. S. Xie, *Phys. Rev. B* 27 (1983) 1516-1522.
- [22] Y. Tanabe and S. Sugano, *J. Phys. Soc. Japan.* 9 (1954) 766-779.
- [23] Y. Y. Yeung, C. Rudowicz, *Comput. Chem.* 16 (1992) 207-216.
- [24] J.I. Zink, *J. Am. Chem. Soc.* 94 (1972) 8039-8045.
- [25] J.I. Zink, *J. Am. Chem. Soc.* 96 (1974) 4464-4470.
- [26] L.G. VanQuickenborne and A. Ceulemans, *Coord. Chem. Rev.* 48 (1983) 157-202.
- [27] J.I. Zink and K.K. Shin, « *Molecular distortions in Excited Electronic States determined from Electronic and Resonance Raman Spectroscopy* », in *Advances in Photochemistry* (Wiley, New York, 1991), pp119-214.
- [28] A. Lempicki, L. Andrews, S. J. Nettel, B. C. McCollum and E. I. Solomon, *Phys. Rev. Lett.* 44 (1980) 1234-1237.
- [29] M. A. Illarramendi, R. Balda, and J. Fernandez, *Phys. Rev. B* 47 (1993) 8411- 8417.
- [30] Y. Tanabe and S. Sugano, *J. Phys. Soc. Japan* 9 (1954) 766-779.
- [31] J. Fernández, M. A. Illarramendi and R. Balda, *J. Non-Cryst. Solids* 131-133 (1991) 1230-1234.
- [32] Fuxi, G. *Optical and Spectroscopic Properties of Glass*; Springer: Berlin, 1992.
- [33] Condon, E. U. and Shortley, G. H. *The Theory of Atomic Spectra*, University press, Cambridge and New York, 1935(reprinted 1951).

Synthesis and Characterization of Aliphatic-Aromatic Copolyesters PET-PLA From PET Waste and Lactide

M. Ben Gara^a, W. Kammoun^a, C. Delaite^b and S. Abid^a

^a *Laboratoire de chimie appliquée HCGP, Faculté des sciences, Université de sfax, 3000 Sfax, Tunisie*

^b *Laboratoire de Photochimie et d'ingénierie macromoléculaire, Université de Haute Alsace, Cedex, France*

myriambengara@gmail.com

Received date: May 06, 2016; revised date: June 28, 2016; accepted date: June 28, 2016

Abstract

Copolyesters containing aliphatic units in the main chain were obtained by reacting Bis(2-hydroxy ethyl terephthalate) (BHET) with Lactide at a high temperature in bulk in presence of tin (II)octoate as the catalyst. Various copolyesters were synthesized by using BHET/Lactide mass ratio ranging from 70/30 to 40/60. Thermal properties were studied by DSC and TGA, and structural characterization was carried out by ¹H NMR spectroscopy. These techniques confirm the insertion of lactide units in PET chains. All copolyesters exhibit some block copolymer character.

Keywords: Copolymerization, Melt polycondensation, Bis(2-hydroxy ethyl terephthalate), Lactide, Random microstructure.

1. Introduction

Poly(ethylene terephthalate) (PET) is a thermoplastic polymer, which is used as fibres, sheets and soft drink bottles. (1)

PET is strong and durable, chemically and thermally stable, has low gas permeability and is easily processed and handled. (2, 3) This combination of properties makes PET a desirable material for a wide range of applications and a significant component of worldwide plastic consumption.

As a result of the diversity of this applications in a high volume of consumer products, large amount of PET waste is also generated, which includes polymer manufacturing waste as well as the products after the end of their useful life. With the increasing pressure of keeping the environment clean, recycling the PET waste in an ecofriendly manner is the only solution.

Post-consumer PET can be recycled into new items or into monomers or oligomers which are generally hydroxy-terminated and can be used for the synthesis of derived polyesters of PET such as PET - poly(lactide), PET - poly(glycolide), or PET - poly(ϵ -caprolactone). (3)

Chemical recycling of PET by glycolysis has been the focus of many research studies. (4-7)

In the recent years, the synthesis of biodegradable copolyesters of PET has received a growing interest.

A number of aliphatic-aromatic copolyesters have thus been produced e.g. poly(butylene succinate)/poly(butylene terephthalate) (8-11), poly[(butylene adipate)-co-(butylene succinate)]/poly(butylene terephthalate) (12), poly(butylene succinate)/poly(ethylene terephthalate) (13), poly(ethylene terephthalate)/poly(ethylene succinate) (14), poly(ethylene adipate)/poly(ethylene terephthalate) (15), poly(ethylene terephthalate)/poly(ϵ -caprolactone) (4,16-18), poly(ethylene terephthalate)/polylactide (19-21) and poly(ethylene terephthalate)/Polyglycolide. (22)

Some methods have been reported for the synthesis of PET-PLA copolymers such as (i) the melt transesterification reaction between bis-hydroxyethyl terephthalate and PLA oligomers (19) and (ii) the reaction between DMT, EG and lactic acid (20) or bis-hydroxyethyl terephthalate with lactic acid. (21)

The reaction of commercial BHET with Lactide has been much less investigated. However, this reaction *presents two major advantages*: (i) no release of by-products, (ii) obtaining of copolyesters with high molecular weight. (23)

In this paper, we describe the synthesis of novel biodegradable copolyester PET- PLA prepared by melt polycondensation from bis-2-hydroxyethyl terephthalate (BHET) and Lactide. Their structure, microstructure and degradation were investigated.

2. Experimental Part

a. Materials

Lactide (99%) was obtained from Sigma aldrish, Stannous Octoate((Oct)₂Sn), Ethane-1,2-diol (EG-99,8%) and cobalt(II) acetate tetrahydrate(+98%) were purchased from Sigma-Aldrich (Germany) and used without further purification.

b. Synthesis

Synthesis of bis(2-hydroxyethyl terephthalate) (BHET) by glycolysis of poly(ethylene terephthalate). (4)

Bottles of mineral water were washed, cut into slices and finely ground. In a reactor equipped with a magnetic stirring, 80 g of PET flakes (0.42 mol of ethylene terephthalate units), 160 g (2.57mol) of EG and 0.249 g (0.001 mol) of cobalt acetate tetrahydrate as catalyst were charged at T = 190 ° C. After 3 hours of reaction, 400 ml of boiling water was added to the reactor and the mixture was stirred vigorously.

The obtained product was filtered to separate the oligomers from PET of high mass. The filtrate was placed at 4°C for 48 h. The white crystalline flakes of BHET were filtered and dried. A yield of 90% BHET with high purity was attained.

Synthesis of BHET-Lactide copolyesters by ring-opening polymerization.

BHET (0.0118mol,3.00g), Lactide (0.0208 mol,3.00g) and 0,1 % (mass) Stannous Octoate((Oct)₂Sn) were placed in a 50-mL glass reactor equipped with a mechanical stirrer and a nitrogen inlet. The reactor was heated gradually from 160 to 180°C under nitrogen (3 h). After cooling to 160°C, vacuum (0.01mbar) was applied and temperature was raised again gradually to 180°C for 1 h. The reaction was continued for 4 h to carry out the reaction of polytransesterification. All copolymers were characterized without any purification.

c. Measurements

¹H NMR spectra were recorded on a Bruker DRX 400 spectrometer. BHET/Lactide copolyesters were dissolved in CDCl₃ solvent. Chemical shifts were referenced to residual CHCl₃ at 7.26 ppm. The infrared spectrum ...

Molecular weight (M_n) and molar mass dispersity (Đ_n) of all copolyesters were determined using size exclusion chromatography (SEC) analyses performed on a Shimadzu LC-20AD liquid chromatography equipped with two Varian PL gel 5 μm MIXED-C columns (column, injection and refractometer temperature: 30°C; injection volume: 100 μL) and a refractive index detector (Shimadzu RID-10A). THF was used as the eluent at a flow rate of 1.0 mL/min. The molecular characteristics were determined relative to linear polystyrene calibration standards. All polymers were dissolved in THF (10 mg mL⁻¹).

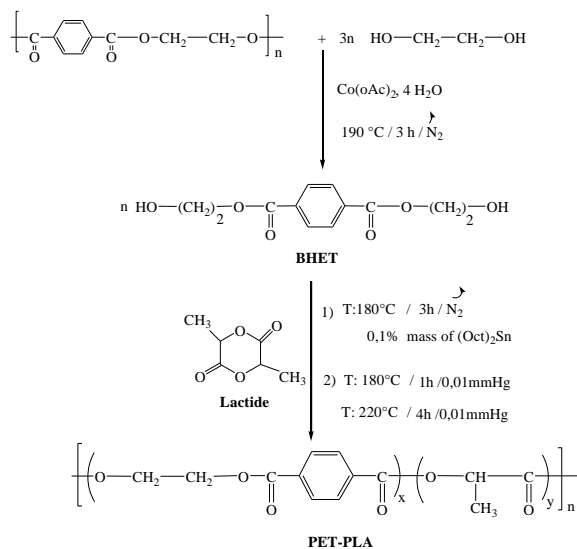
Differential Scanning Calorimetry (DSC) was carried out on a DSC Q2000-Modulated TA Instruments apparatus equipped with a liquid nitrogen cooling accessory, at cooling and heating rates of 20 °C. min⁻¹. Non hermetic aluminum capsules containing about 10 mg of polymer were subjected to two successive temperature ramps under nitrogen from -80°C to 360°C. Melting temperatures (T_m) were taken at the minima of the melting endotherms and glass transition temperatures (T_g) at the inflection point.

Thermogravimetric Analysis (TGA) was carried out on a TA Instruments Q500 thermogravimetric analyzer system at a heating rate of 10°C.min⁻¹ under a nitrogen atmosphere.

The inherent viscosity [η_{inh}] of the copolyesters samples in chloroform was measured at 25 °C in a constant-temperature bath using a UBBELOHDE viscometer. From the time flow of solvent and solution, the inherent viscosity [η_{inh}] was calculated.

3. Results and discussion

The reaction between BHET and Lactide was carried out at 160°C and 220°C for 8h in the bulk, in the presence of Stannous Octoate((Oct)₂Sn) as a catalyst (0,1% mass) (scheme1). A possible reaction mechanism could involve the homopolymerization of lactide and the formation of copolymer by PET-poly lactide ester interchange.



Scheme 1. synthesis of BHET-Lactide copolyesters.

The infrared spectrum of BHET/Lactide copolymer is shown in Fig. 1. It can be clearly seen that the spectrum contains aliphatic CH at 2961 cm^{-1} , aromatic CH at 1452 and 1409 cm^{-1} , C-O single bond and ester carbonyl at 1244 cm^{-1} and at 1714 cm^{-1} respectively.

Depending on composition and reaction time, these copolyesters may be random or may exhibit some block copolymer character. The structure and microstructure of these copolyesters were, therefore, investigated by ^1H NMR spectroscopy.

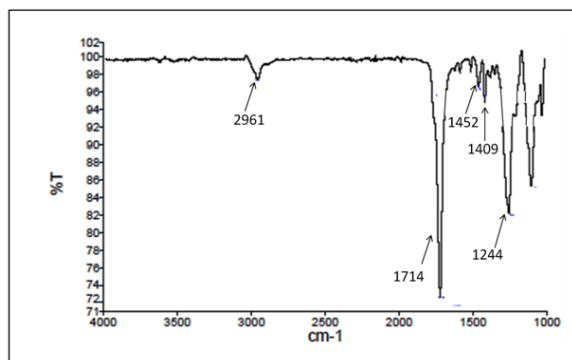
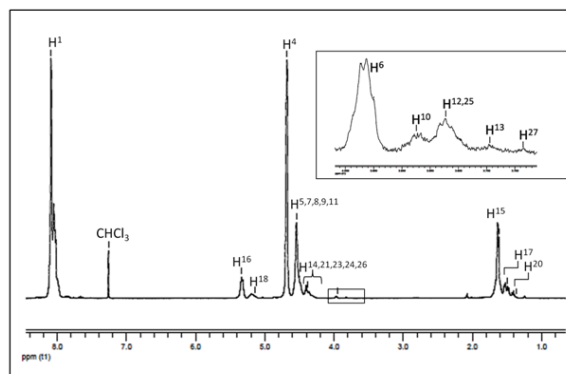


Figure 1. FTIR spectrum of BHET/lactide copolymer (50/50).

^1H NMR study of BHET-Lactide copolyesters

In addition to PET signals, the ^1H NMR spectra of copolyesters obtained using various initial (BHET/Lactide) ratios displayed a series of peaks in the 4.2–4.8 ppm region, which can be assigned to the

species depicted in table 1. As an example, the ^1H NMR spectrum of the 50/50 PET/PLA copolyester was given in Fig. 2.

Figure 2. ^1H NMR spectrum of copolyester BHET-Lactide (50/50) (in CDCl_3).

TET (H^1 , 4.67 ppm); TEL+LET ($\text{H}^{7,8}$, 4.54 ppm) and LEL (H^{23} , 4.38 ppm) triads are easily identified in the spectrum (T=Terephthalate, L=Lactide, E=1,2-ethylene). (Table 1)

The existence of TEL triads, is evidence of Lactide insertion in PET chains.

The number-fractions F_{E} (TET), F_{E} (TEL+LET) and F_{E} (LEL) of TET, TEL and LEL E-centered triads in PET-PEL copolyesters were determined by integrating the corresponding NMR peaks. F_{E} (TET), F_{E} (TEL+LET) are proportional to $I_{\text{T}}/4$ and $(I_{\text{T}}+I_{\text{L}})/4$ respectively, where I is the integration of the H_n resonance

The actual terephthalate (T)/lactate (L) mol ratio was easily determined from the total integrations of aromatic protons (H^1 at 8.1 ppm) and lactate methyl resonances ($\text{H}^{15,17,20}$ at 1.3–1.8 ppm). Due to sublimation of lactide, the T/L mol ratio final in copolyesters is significantly lower than the starting one, $(\text{T/L})_0$ (Table 2).

The new signal at 1.63 ppm (H^{15}) corresponds to T-L diads. The signal at 5.32 (H^{16}) and 5.19 ppm (H^{18}) correspond to L-T and L-L diads, respectively.

The peak at 4.67 ppm is assigned to T-E-T triads (H^5). A number of signals are superimposed at ca. 4.54 ppm: $\text{H}^{7,8}$ of T-E-L triads and methylenes in β -position to OH endgroups (H^9) and to ether oxygens (H^{11}). In the same way, the signal of L-E-L triads at 4.38 ppm (H^{23}) overlaps with a series of peaks corresponding to groups linked to lactate units ($\text{H}^{12,25}$) and to $-\text{CH}(\text{CH}_3)-\text{OH}$ end-groups (H^{27}). (T=terephthalate, L=Lactide, E=1,2 ethylene).

Table 1. Atom numbering in BHET -Lactide copolyesters.

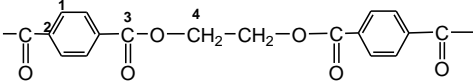
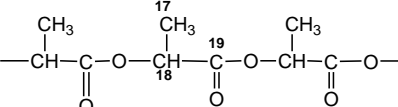
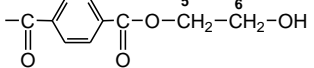
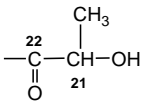
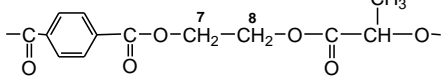
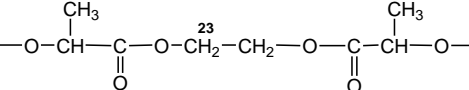
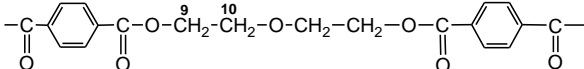
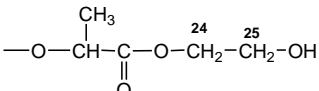
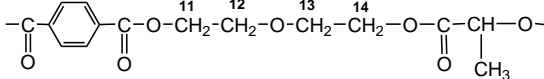
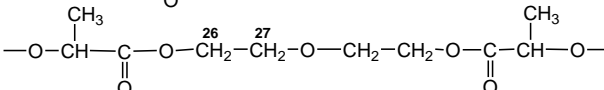
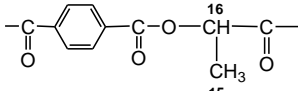
PET units	Lactate units
	
	
	
	
	
	

Table 2. Chain microstructure in BHET/Lactide copolymers: Number-fractions of TET, TEL, LEL triads, F_E (TET), F_E (TEL+LET) and F_E (LEL).

Samples	F_E (TET) ^{b)}	F_E (TEL) ^{b)}	F_E (LEL) ^{b)}	F_T/F_L ^{c)}	F_T/F_L ^{d)}
BHET/Lactide(70/30) ^{a)}	0.571	0.369	0.058	56.89/43.10	62.5/37.5
BHET/Lactide(60/40) ^{a)}	0.577	0.378	0.043	45.92/54.07	55.5/44.4
BHET/Lactide(50/50) ^{a)}	0.591	0.343	0.066	36.19/63.80	62.0/37.9
BHET/Lactide(40/60) ^{a)}	0.539	0.380	0.079	26.47/73.52	56.4/43.5

a) (m_1/m_2) represents the initial BHET/Lactide mass ratio.

b) fraction of TET, TEL and LEL in final copolymers

c) Initial mole fraction of T and Lactide units in initial reaction mixture.

d) Mole fraction of T and Lactide units in final copolymer.

Moreover, hydroxy end group and oxydiethylenemoieties linked to different neighboring entities can also be identified.

The "degree of randomness", R , introduced by Yamadera (24) as a parameter for characterizing the extent of randomization in condensation copolymers, was used to characterize the extent of randomization in these copolymers.

$$R = \frac{F(TEL)}{2F_L} + \frac{F(LET)}{2F_T} = P_{LT} + P_{TL}$$

F_T and F_L represent the molar fraction of terephthalate and lactide units in copolymer and are determined from NMR spectra.

P_{TL} and P_{LT} are the probability of finding an ET repeating unit next to a Lactide repeating unit, and a Lactide repeating unit next to an ET repeating unit when going from one chain end to the other, respectively.

Table 3. Chain microstructure of BHET-Lactide copolyesters: number-average block length of T and L units in ethylene terephthalate and Lactide blocks, $\overline{L}_{n,T}$ and $\overline{L}_{n,L}$, degree of randomness, R.

Sample	$\overline{L}_{n,T}$	$\overline{L}_{n,L}$	R
BHET/Lactide(70/30) ^{a)}	3.38	2.03	0.787
BHET/Lactide(60/40) ^{a)}	2.94	2.35	0.765
BHET/Lactide(50/50) ^{a)}	3.62	2.21	0.728
BHET/Lactide(40/60) ^{a)}	2.97	2.29	0.772

a) (m₁/m₂) represents the initial BHET/lactide mass ratio.

The degree of randomness R is equal to 0 for blends, to 1 for random copolymers and varies between 0 and 1 for block copolymers. $1 < R < 2$ for copolymers having a tendency to form alternating structure.

The R values and the number-average block lengths calculated from NMR spectra are reported in Table 3. All copolyesters exhibit some block copolymer character ($R < 1$) due to the sublimation of the lactide. Therefore final Lactide fraction in the copolymer is lower than of terephthalate fraction.

Table 4. Inherent viscosity and molecular weight data of BHET/Lactide copolyesters.

Samples	$[\eta]_{inh}$ (dl/g) ^{b)}	M_n (g/mol) ^{c)}	M_w (g/mol) ^{c)}	\overline{D}_M ^{c)}
BHET/Lactide (40-60) ^{a)}	0.227	13.900	39.100	2.8
BHET/Lactide (50-50) ^{a)}	0.262	17.000	54.200	3.1
BHET/Lactide (60-40) ^{a)}	0.210	14.500	38.500	2.6
BHET/Lactide (70-30) ^{a)}	0.187	* d)	* d)	* d)

a) (m₁/m₂) represents the initial BHET/Lactide mass ratio.

b) 1.5g/l of polymer in CHCl₃ at 25°C.

c) Determined by SEC using polystyrene calibration standards.

d) Insoluble in THF.

Thermal properties

BHET/Lactide(70/30) semi-crystalline copolyester is and exhibit one glass transition temperature (T_g) and one melting temperature (T_m) which are lower than those of PET ($T_g = 83^\circ\text{C}$, $T_m = 255^\circ\text{C}$) (4) but higher

SEC study of BHET-Lactide copolyesters

The SEC analysis was therefore carried out on BHET-lactide 60/40 to 40/60, which exhibits good solubility in THF. The values of the average molar masses determined by SEC and by using polystyrene calibration are reported in Table 4.

The number-average molar masses of this copolyesters were $M_n = 13.900$ to 17.000 g/mol

M_n values are more interesting than those obtained by E. Olewnik ($M_n = 6100$ for 50/50 copolyester), (19) the synthesis of aliphatic-aromatic copolyesters from a cyclic ester allows the obtaining of high molar mass copolyesters.

\overline{D}_M is significantly higher to 2 because of the presence of side reaction such as etherification and formation of cyclic species which are inevitable in polycondensation reactions.

The M_w of these copolyesters could not be determined from NMR spectra due to (i) the very low amount of end groups and (ii) the partial overlapping of the resonances of end groups ($H^{6,20}$) and ether groups (H^{12}) arising from etherification side reactions during the second reaction step.

than those of PLA homopolymers ($T_g = 52^\circ\text{C}$, $T_m = 156^\circ\text{C}$) (19), which reflects the insertion of lactate units in the copolyesters chains. (Figure 3).

BHET/Lactide 60/40 to 40/60 copolyesters are amorphous, which can easily be understood in view of their very short sequence length (Table 5).

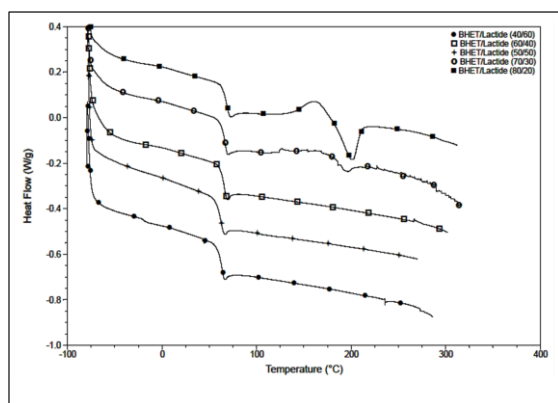


Figure 3. DSC curves of PET-PLA copolymers

Table 5. Thermal analysis data of copolyesters.

Samples	T _g ^{°C} (a)	T _m ^{°C} (a)	T _{d, 5%} ^{°C} (b)
PET ⁽¹⁹⁾	83.0	255.0	360
BHET/Lactide (70/30)	66.78	194.43	341
BHET/Lactide (60/40)	66.29	*	325
BHET/Lactide (50/50)	62.52	*	293
BHET/Lactide (40/60)	58.73	*	310
PLA ⁽¹⁹⁾	52	156	221

The TGA analysis showed a good thermal stability for all copolyesters. (Fig.4).

The temperature of degradation of copolyesters is slightly above that of PLA, but much lower than that of PET homopolymer.

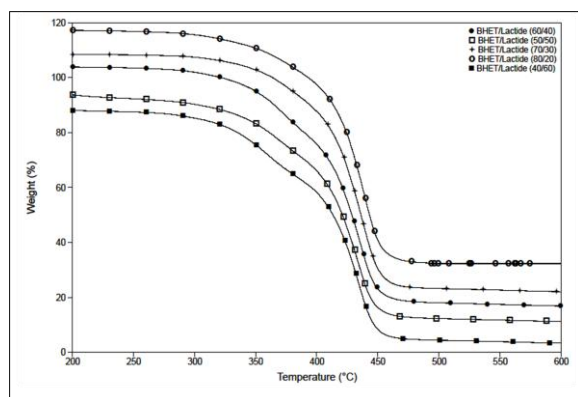


Figure 4. TGA curves of PET-PLA copolymers

Conclusion

This work showed that the insertion of lactate units into PET chains by a reaction between bis (2-hydroxy ethyl terephthalate) and Lactide in both easy and efficient, leading to high molar mass copolyesters.

As expected, ¹H NMR spectra also reflect the insertion of lactate units in PET polymer chains and allows the study of chain microstructure.

The degree of randomness of copolyesters is significantly lower than unity, indicating that they present some block copolymer character. This appears rather surprising in view of the high reaction temperature.

Copolyesters thermal properties were studied by DSC and TGA. The thermogravimetric analysis reveals fairly good thermal stabilities for all PET/PLA copolyesters.

The glass transition and melting temperatures of all copolyesters are lower than those of PET but higher than those of high molar mass PLA and are relatively higher than those of PET/PLA copolyesters synthesized from a mixture of homopolymer (19).

References

- (1) Webb, HK, Arnott, J, Crawford, RJ, Ivanova, EP (2013) *Polymer*, 54: 1-18.
- (2)
- (3) Awaja, F, Pavel, D (2005) *Eur. Polym. J.*, 41: 1453-1477.
- (4) Kint, D, Muñoz-Guerra, S (1999). *Polym. Int.* 48: 346-352.
- (5) Gara, M, Kammoun, W, Delaite, C, Abid, S, El Gharbi, R (2015) *J. Macro. Sci.*, 52: 454-464.
- (6) Chaudhary, S, Surekha, P, Kumar, D, Rajagopal, C, Roy, PK (2013) *J. Appl. Polym. Sci.*, 129: 2779-2788.
- (7) López-Fonseca, R, Duque-Ingunza, I, De Rivas, B, Flores-Giraldo, L, Gutiérrez-Ortiz, JI (2011) *Chem. Eng. J.*, 168: 312-320.
- (8) Yue, QF, Wang, CX, Zhang, LN, Ni, Y, Jin, YX (2011) *Polym. Degrad. Stabil.*, 96: 399-403.
- (9) Park, SS, Chae, SH, Im, SS (1998) *J. Polym. Sci. Part A: Polym. Chem.*, 36: 147-156.
- (10) Lee, SH, Lim, SW, Lee, KH (1999) *Polym. Int.*, 48: 861-867.
- (11) Nagata, M, Goto, H, Sakai, W, Tsutsumi, N (2000) *Polymer*, 41: 4373-4376.
- (12) Honda, N, Taniguchi, I, Miyamoto, M, Kimura, Y (2003) *Macromol. Biosci.*, 3: 189-197.

- (13) Kang, HJ, Park, SS (1999) *J. Appl. Polym. Sci.*, 72:593-608.
- (14) Kint, DPR, Alla, A, Deloret, E, Campos, JL, Munoz- Guerra, S, (2003) *Polymer*, 44: 1321-1330.
- (15) Salhi, S, Tessier, M, Blais, JC, El Gharbi, R, Fradet, A (2004) *Macromol. Chem. Phys.*, 205: 2391-2397.
- (16) Heidary, S, Gordon, B (1994) *J. Polym Environ*, 2:19-26.
- (17) Ma, D, Zhang, G, Huang, Z, Luo, X (1998) *J. Polym. Sci. Part A: Polym. Chem.* 36: 2961-2969.
- (18) Tang, W, Murthy, NS, Mares, F, McDonnell, ME, Curran, SA (1999) *Appl. Polym. Sci.*, 74: 1858-1867.
- (19) Tillier, D, Lefebvre, H, Tessier, M, Blais, JC, Fradet, A (2004) *Macromol. Chem. Phys.*, 205: 581-592.
- (20) Olewnik, E, Czerwinski, W, Nowaczyk, J, Sepulchre, MO, Tessier, M, Salhi, S, Fradet, A (2007) *Eur. Polym. J.*, 43:1009-1019
- (21) Buasri, A, Chaiyut, N, Jenjaka, T, Weerasunthorn, S, Juengrunghaiwattana, S (2011) *J. Sci.*, 38(4): 619-624
- (22) Sriromreun, P, Petchsuk, A, Opaprakasit, M, Opaprakasit, P (2013) *Polym. Degrad. Stabil.*, 98: 169-176.
- (23) Olewnik, E, Czerwinski, W (2009) *Polym. Degrad. Stabil.*, 94: 221-226.
- (24) Dorure, DK, Reed, AM (1979) *Polymer*, 20: 1459-1464.
- (24) Yamadera, R, Murano, M (1967) *J. Polym. Sci. Part A: Polym. Chem.*, 5: 2259-2268.

Synthesis and Characterization of L-alanine based Poly(ester-amide)s

Abbes Marwa^a, Salhi Slim^a, Delaite Christelle^b, Abid Souhir^{a*} and EL-Gharbi Rachid^a

^a *Laboratoire de Chimie Appliquée HCGP, Faculté des Sciences, Université de Sfax, 3000 Sfax, Tunisie*

^b *Laboratoire de Photochimie et d'Ingénierie Macromoléculaire, Université de Haute Alsace, Cedex, France*

marwa.abbestrigui@gmail.com

Received date: May 06, 2016; revised date: June 28, 2016; accepted date: June 28, 2016

Abstract

Novel biomaterials L-alanine based poly(ester-amide)s (PEAs) differing in the amide/ester ratio have been directly synthesized by direct melt copolycondensation of Adipic acid, L-alanine and various aliphatic and heterocyclic diols. PEAs were systematically characterized with intrinsic viscosity, FTIR, ¹H-NMR, ¹³C-NMR, DSC and SEC measurements. The resulting copolymers are amorphous and present increasing glass transition temperatures at increasing L-Alanine contents. L-Alanine-PEAs proved to be materials having high molecular weights that could reach 41800 g/mol.

Keywords: Adipic acid/ L-alanine/ melt polycondensation/ microstructure/ NMR/ Poly(ester-amide).

1. Introduction

In the past few decades, poly(ester-amide)s (PEAs) based on natural amino acids have attracted much attention in terms of their special and distinctive characteristics, they combine the interesting properties of conventional PEAs with those resulting from the presence of the amino acids (1). These polymers possess good thermal stability and good mechanical and processing properties like tensile strength and modulus, due to the strong hydrogen-bonding interactions established between amid groups. The use of amino acids in PEAs synthesis can be also justified by many reasons; in addition to their abundant availability from natural resources, they confers to their derivatives potential susceptibility to biodegradation under certain enzymatic catalyzed conditions, in the opposite of their counterparts based on other types of monomers like diamines (2).

In this context, biocompatibles amino acids based PEAs find a wide range of medical applications (3), like drug delivery systems; indeed microspheres or electrospun nanofibers based on PEAs could perform good controlled drug release (4,5). In tissue engineering, it has been proved that amino acid based

PEAs could be used as cardiovascular biomaterials, they were able to support the attachment, spreading and proliferation of smooth muscle cells of the human coronary artery, which make them good candidates for vascular tissue engineering scaffolds (6-8). Drug charged hydrogels can be also elaborated by photopolymerization of amino acids based PEA and the appropriate drug (9,10).

Different synthesis methodologies of PEAs from amino acids were reported in literature. Ring opening polymerization of morpholine-2,5-dione derivatives which are cyclic dimers resulting from α -hydroxyacids and α -aminoacids, is a very old technique. It can be elaborated in the presence of metallic or enzymatic catalysis (11-14). The ring opening polymerization of ϵ -caprolactone with different amino acids was reported recently and leads to PEAs with high molecular weights and high Young's modulus and tensile strength (15-18).

These polymers can be also obtained by solution polycondensation of an amino acid with a diol and a dicarboxylic acid, this method followed by Chu et coll (19-26) is advantageous because it is carried out in mild operating conditions and accomplished in high yields and molecular weights, but in return, it requires very high monomers purity and extensive polymer purification to eliminate solvent and toxic by-products

generated. Puiggali et coll synthesized regular PEAs by interfacial or thermal polycondensation. Interfacial polycondensation consist on the preparation of di-p-toluenesulfonic acid salts by Fischer esterification between amino acids like L-alanine (27-31), Glycine (30-33), β -alanine (34) or L-phenylalanine (35), and diols, in the presence of p-TSA, and its reaction with diacyl chlorides. The thermal polycondensation involves the reaction of a diol with a diester-terminated diamide, previously obtained from the condensation of a diacyl chloride with an amino acid methyl ester (36-40).

Melt direct polymerization is a very advantageous method for industrial use because it is carried on in one step, it avoids the prior preparation of the intermediates mentioned previously for other synthesis routes, and because no post-treatment of resulting polymers is necessary. Our group performed the melt polycondensation of β -alanine and glycolic acid (41); random amorphous PEAs were obtained with high thermal stability and high glass transition temperatures. We reported in a previous work the synthesis of β -alanine based PEAs, amorphous PEAs were obtained (42). In order to improve the glass transition temperatures and the solubility of resulting polymers, we study the substitution of β -alanine by L-alanine. In fact, L-alanine based polymers have particular properties; methyl side groups increases glass transition temperatures, they also improves the solubility in organic solvents such as chloroform, in this way it is possible to obtain microspheres that can be used as drug delivery systems (31). Moreover, polymers based on L-alanine show better enzymatic degradation than their counterparts based on other types of monomers like glycine (30).

To the best of our knowledge, L-alanine was never used in direct melt polycondensation, we proposed in the present paper to synthesize novel PEAs by direct melt polycondensation between L-alanine, adipic acid and different aliphatic or heterocyclic diols and to study the effect of amide percentage on microstructure and thermal properties of resulting copolymers.

2. Experimental Part

2.1 Materials

L-Alanine (L) (purchased from Aldrich), Adipic acid (A) (purchased from Acros Organics), Ethylene glycol (E); 1,3-Propanediol (P); 1,4-Butanediol (D); 1,6-Hexanediol (H); Isosorbide (I) (purchased from Aldrich), Tetrabutoxytitanium (Ti(BuO)₄) (purchased

from Aldrich) were high purity compounds used as received without further purification.

2.2 Synthesis of PALD copolymers: PALE, PALP, PALB, PALH and PALI

A series of poly(ester-amide)s were synthesized according to scheme 1 and table 1. A reactor equipped with a magnetic stirrer was charged with L-Alanine (L) (1 mol), Adipic acid (A) (1 mol), and an excess of a diol (3 mol) (Ethylene glycol (E); 1,3-Propanediol (P); 1,4-Butanediol (B); 1,6-Hexanediol (H) or Isosorbide (I)). Tetrabutoxytitanium (0.3 wt %) was added as a catalyst for the condensation reaction. The reactor was heated in an oil bath at 210 °C in order to melt the mixture under nitrogen atmosphere and to help eliminate water and the excess of diol. After one hour, the temperature was raised to 220 °C for 4h. After cooling the reactor to room temperature, vacuum was applied (0.01 mmHg) while the temperature was raised progressively to 190°C for 2h, and then to 220 °C for 6h. The resulting polymers were analyzed without further purification.

2.3 Synthesis of PALB-x/y copolymers

The Poly(ester-amide)s are denoted PALB-x/y, where x/y represents the Amide/ester ratio and varied from 50/50 to 10/90 (table 1). A typical PALB-50/50 copolymer was prepared as follows: A mixture of Adipic acid (1mol), L-alanine (2 mol) and 1,4-Butanediol (2 mol) was heated at 210 °C for 2 h under nitrogen atmosphere in a reactor fitted with a magnetic stirrer. Tetrabutoxytitanium (0.3 % mol) was carefully added. The reactor was then heated to 220 °C and kept at this temperature under vacuum (0.01 mmHg) for 4 h. The resulting product was analyzed without further purification. L-alanine has a very high melting temperature (295°C), we could not exceed 50% of initial amide percentage because of the difficulty of the solubility of amino acid (L-Ala) in reaction medium.

2.4 Characterization

Infrared absorption spectra were recorded with a Perkin-Elmer spectrum 100 spectrometer in the 4000-700 cm⁻¹ range. NMR spectra of polymers were registered from deuterated chloroform. Chemical shifts were referenced to the peak of residual CHCl₃ at 7.26 ppm. A Bruker AC-300 spectrometer operating at 300 MHz and a Bruker AC 400spectrometer operating at 400 MHz were used for ¹H and ¹³C-NMR investigations respectively.

Molecular weight (M_n and M_w) and molar mass dispersity (D_n) of all copolymers were determined using size exclusion chromatography (SEC) analyses performed on a Shimadzu LC-20AD liquid chromatography equipped with two Varian PL gel 5 μ m MIXED-C columns (column, injection and refractometer temperature: 30°C; injection volume: 100 μ L) and a refractive index detector (Shimadzu RID-10A). THF was used as the eluent at a flow rate of 1.0 mL/min. The molecular characteristics were determined relative to linear polystyrene calibration standards. All polymers were dissolved in THF (10 mg mL⁻¹).

Thermal analyses were performed by differential scanning calorimetry (DSC) using a TA Instrument DSC calorimeter Q 2000. The samples (10 mg) were subjected to two successive temperature ramps under nitrogen from -70 °C to 180 °C at a rate of 20°C/min.

Thermogravimetric analyses were performed with a TA Instrument TGA Q500. Between 3 and 8 mg of sample were placed in a platinum crucible and subjected to a temperature ramp from 20°C to 800 °C with a rate of 10 °C / min under nitrogen flow.

Intrinsic viscosity $[\eta_{int}]$ measurements were performed by using an Ubbelohde viscometer at 25°C in chloroform. All copolymers were dissolved at room temperature in order to prepare solutions of 1.5 g/dl concentration.

Intrinsic viscosity was calculated using the Solomon-Ciuta equation (43, 44). $[\eta_{int}] = [2 ((t/t_0) - \ln(t/t_0) - 1)]^{1/2} / C$. Where C is the concentration of the solution; t, the flow time of solution and t_0 is the flow time of pure solvent.

Table1. Chemical formulas of different synthesis Poly(ester-amide)s (PALD)

Copolymer	Chemical formula
PALE	$\left[\left[\text{O}-(\text{CH}_2)_2-\text{O} \right]_x \left[\text{C}(=\text{O})-(\text{CH}_2)_4-\text{C}(=\text{O}) \right]_y \left[\text{HN}-\overset{\text{CH}_3}{\text{C}}-\text{C}(=\text{O}) \right]_z \right]_q$
PALP	$\left[\left[\text{O}-(\text{CH}_2)_3-\text{O} \right]_x \left[\text{C}(=\text{O})-(\text{CH}_2)_4-\text{C}(=\text{O}) \right]_y \left[\text{HN}-\overset{\text{CH}_3}{\text{C}}-\text{C}(=\text{O}) \right]_z \right]_q$
PALB	$\left[\left[\text{O}-(\text{CH}_2)_4-\text{O} \right]_x \left[\text{C}(=\text{O})-(\text{CH}_2)_4-\text{C}(=\text{O}) \right]_y \left[\text{HN}-\overset{\text{CH}_3}{\text{C}}-\text{C}(=\text{O}) \right]_z \right]_q$
PALH	$\left[\left[\text{O}-(\text{CH}_2)_6-\text{O} \right]_x \left[\text{C}(=\text{O})-(\text{CH}_2)_4-\text{C}(=\text{O}) \right]_y \left[\text{HN}-\overset{\text{CH}_3}{\text{C}}-\text{C}(=\text{O}) \right]_z \right]_q$
PALI	$\left[\left[\text{O}-\text{C}_5\text{H}_8\text{O}_2-\text{O} \right]_x \left[\text{C}(=\text{O})-(\text{CH}_2)_4-\text{C}(=\text{O}) \right]_y \left[\text{HN}-\overset{\text{CH}_3}{\text{C}}-\text{C}(=\text{O}) \right]_z \right]_q$

3. Results and discussion

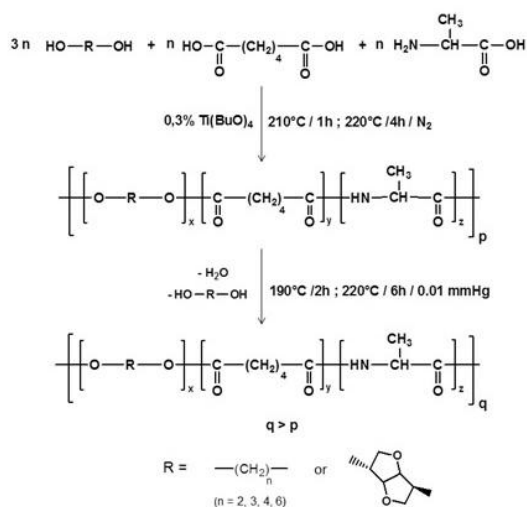
Various Poly(ester-amide)s copolymers denoted PALD were synthesized from Adipic acid (A), L-alanine (L) and different diols (D) by direct melt copolycondensation according to Scheme 1. The mixture of monomers was first heated to perform the formation of a dicarboxy-terminated amide dimers from L-alanine and adipic acid, then the esterification of generated dimers by the appropriate diol. Titanium butoxide catalyst is added to activate the carbonyl of the dicarboxylic acid and facilitate its attack by amino

or hydroxyl functions. The resulting oligomer mixture was then reacted under vacuum to yield high molar mass copolymers.

3.1 Influence of the nature of dihydroxy monomer unit

Five poly(ester-amide)s synthesized from adipic acid, L-alanine and ethylene glycol, 1,3-Propanediol, 1,4-Butanediol, 1,6-Hexanediol and Isosorbide respectively were selected for this study. The major difference between these PEAs is the length of the dihydroxy monomer unit.

The $^1\text{H-NMR}$, $^{13}\text{C-NMR}$ and FTIR spectroscopic data of resulting PEAs were in total agreement with their anticipated chemical constitution.



Scheme1. Synthesis of PALD copolymers

FTIR spectra of PALD copolymers exhibit the expected features. A typical infrared spectrum of PALE is shown in Figure 1, with absorptions corresponding to amide NH (amide A), amide carbonyl (amide I) and amide C-N (amide II) at 3315, 1642 and 1550 cm^{-1} respectively, to aliphatic CH at 2922 cm^{-1} , ester carbonyl at 1739 cm^{-1} , and C-O simple bond at 1154 cm^{-1} .

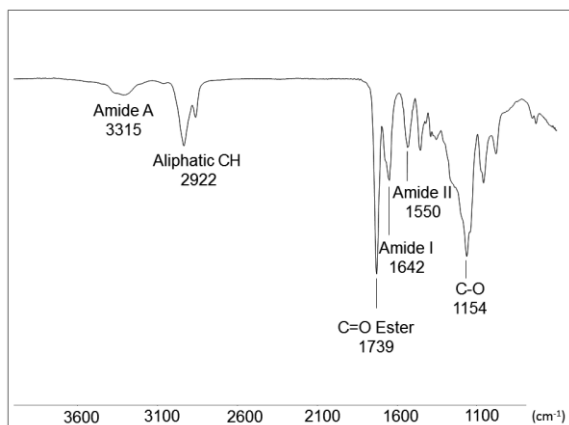


Figure 1. Infrared spectrum of PALE copolymer

Typical $^1\text{H-NMR}$ spectrum of PALE copolymer is shown in Figure 2. We show the presence of L-L dyads of poly(L-alanine) sequence (1^{LL} and 2^{LL} at 4.57 and 1.40 respectively), the presence of E-A dyads of poly(ethylene adipate) sequence (3^{AE} , 4^{AE} and 5^{EA} at 2.35, 1.66 and 4.26 respectively). We observe also the presence of the mixed ester-amide E-L and A-L dyads

(5^{EL} and 3^{AL} at 4.29 and 2.23 respectively). The proton resonances of the $-\text{CH}-$ and $-\text{CH}_3$ of L-alanine units are not affected by the nature of neighboring units, and are observed overlapped at 4.57 ($1^{\text{LL}} = 1^{\text{LE}} = 1^{\text{LA}} = 1^{\text{L}}$) and 1.40 ($2^{\text{LL}} = 2^{\text{LB}} = 2^{\text{LA}} = 2^{\text{L}}$). (See Table 3 for dyads structures and atom numbering).

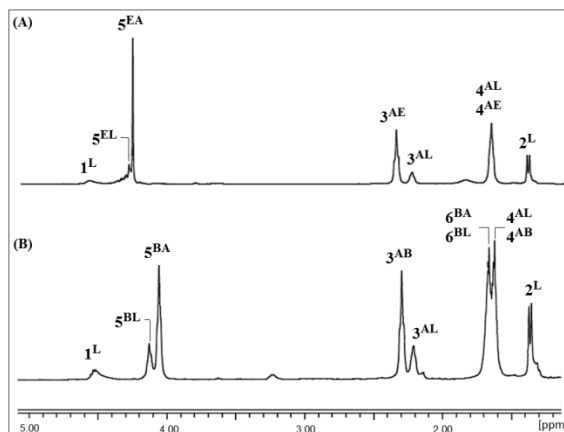


Figure 2. $^1\text{H-NMR}$ spectra of a PALE (A) and PALB-50/50 (B) copolymers (300 MHz, CDCl_3 , ref δ (CHCl_3) = 7.26 ppm)

The experimental proton chemical shifts of all PALD copolymers are listed in table 3 and 4. In addition to the signals present in PALE spectrum, another signal that appears at 1.96 ppm is observed when we use propane-diol corresponding to the methylene (6^{P}) in β position relative to the hydroxyl group, this signal denoted 6^{B} in PALB spectrum appears less deshielded (at 1.69 ppm) when we use butane-diol. In $^1\text{H-NMR}$ spectrum PALH, the aliphatic sequence of the diol becomes longer and therefore the signal 6^{H} appears at 1.59 ppm, preceded by another signal (7^{H}) at 1.47 ppm attributed to the methylene in γ position relative to the hydroxyl group.

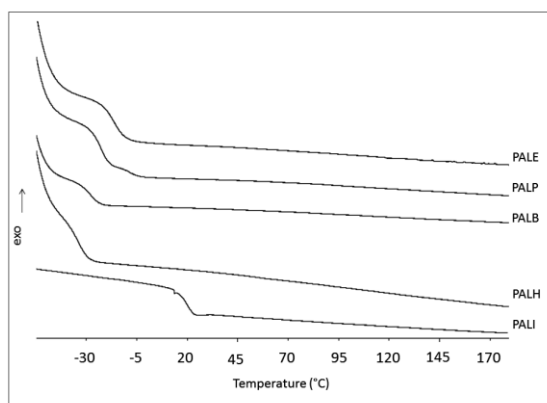


Figure3. DSC curves of PALD poly(ester amide)s

Table2. Dyads present in copolymers (adipic acid (A), L-alanine (L) and diol (D))and the corresponding atom numbering.

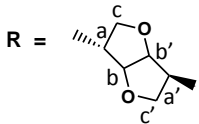
L-L	$\begin{array}{c} \text{CH}_3 \\ \\ -\text{C}-\text{CH}-\text{NH}-\text{C}-\text{CH}-\text{NH}- \\ \quad \quad \quad \\ \text{O} \quad \text{O} \quad \text{O} \quad \text{O} \\ 1^{\text{LL}} \quad 2^{\text{LL}} \end{array}$
D-A	$-\text{O}-\text{R}-\text{O}-\text{C}-\text{CH}_2-(\text{CH}_2)_2-\text{CH}_2-\text{C}- \\ \quad \quad \quad \\ \text{O} \quad \text{O} \quad \text{O} \quad \text{O} \\ 3^{\text{AD}} \quad 4^{\text{AD}}$
A-L	$\begin{array}{c} \text{CH}_3 \\ \\ -\text{C}-\text{CH}_2-(\text{CH}_2)_2-\text{CH}_2-\text{C}-\text{NH}-\text{CH}-\text{C}- \\ \quad \quad \quad \quad \quad \\ \text{O} \quad \text{O} \quad \text{O} \quad \text{O} \quad \text{O} \quad \text{O} \\ 4^{\text{AL}} \quad 3^{\text{AL}} \quad 1^{\text{LA}} \quad 2^{\text{LA}} \end{array}$
D-L	$\begin{array}{c} \text{CH}_3 \\ \\ -\text{O}-\text{R}-\text{O}-\text{C}-\text{CH}-\text{NH}- \\ \quad \quad \\ \text{O} \quad \text{O} \quad \text{O} \\ 1^{\text{LD}} \quad 2^{\text{LD}} \end{array}$
<p>R =  or $-(\text{CH}_2)_n-$: $\left(\begin{array}{cc} 5^{\text{E}} & 5^{\text{P}} \quad 6^{\text{P}} \quad 5^{\text{P}} \\ -\text{O}-\text{CH}_2-\text{CH}_2-\text{O}- & -\text{O}-\text{CH}_2-\text{CH}_2-\text{CH}_2-\text{O}- \\ 5^{\text{B}} \quad 6^{\text{B}} \quad 5^{\text{B}} & 5^{\text{H}} \quad 6^{\text{H}} \quad 7^{\text{H}} \quad 6^{\text{H}} \quad 5^{\text{H}} \\ -\text{O}-\text{CH}_2-(\text{CH}_2)_2-\text{CH}_2-\text{O}- & -\text{O}-\text{CH}_2-\text{CH}_2-(\text{CH}_2)_2-\text{CH}_2-\text{CH}_2-\text{O}- \end{array} \right)$</p>	

Table 3. Chemical shifts and assignments of the ¹H-NMR spectra of PALE, PALP, PALB and PALH based on adipic acid (A), L-alanine (L) and diols (D); ethylene glycol(E), propanediol (P), butanediol (B) and hexanediol (H)

Proton	1 ^L	2 ^L	3 ^{AL}	3 ^{AD}	4 ^{AD} 4 ^{AL}	5 ^{DA}	5 ^{DL}	6 ^{DA} 6 ^{DL}	7 ^{DA} 7 ^{DL}
	δ (ppm)								
PALE	4.57	1.40	2.23	2.35	1.66	4.26	4.29	*	*
PALP	4.57	1.40	2.23	2.32	1.65	4.14	4.21	1.96	*
PALB	4.57	1.40	2.23	2.32	1.65	4.08	4.16	1.69	*
PALH	4.57	1.38	2.23	2.32	1.65	4.05	4.13	1.59	1.47

Table 4. Chemical shifts and assignments of the ¹H-NMR spectra of PALI, based on Adipic acid (A), L-alanine (L) and Isosorbide (I)

Proton	1 ^L	2 ^L	3 ^{AL}	3 ^{AI}	4 ^{AI} 4 ^{AL}	a, a'	b	b'	c	c'
	δ (ppm)									
PALI	4.65	1.40	2.22	2.38	1.65	5.17	4.82	4.44	3.93	3.90

Monomer composition can be evaluated from ¹H-NMR spectra taking into account the area of signals corresponding to **-CH₂-CO** protons of adipic acid units (3^{AD} and 3^{AL}), **-CH-** protons of L-alanine units (1^L) and **-CH₂-O** protons of diol units (5^{DA} and 5^{DL}).

In this way, diol (*f*D), adipic acid (*f*A) and L-alanine (*f*L) molar fractions were calculated according to the equations 1, 2 and 3 respectively:

$$F(D) = \frac{\frac{I(5^{\text{DA}}+5^{\text{DL}})}{4}}{\left[\frac{I(5^{\text{DA}}+5^{\text{DL}})}{4}\right] + \left[\frac{I(3^{\text{AD}}+3^{\text{AL}})}{4}\right] + \left[\frac{I(1^{\text{L}})}{1}\right]} \quad (1)$$

$$F(A) = \frac{\frac{I(3^{\text{AD}}+3^{\text{AL}})}{4}}{\left[\frac{I(5^{\text{DA}}+5^{\text{DL}})}{4}\right] + \left[\frac{I(3^{\text{AD}}+3^{\text{AL}})}{4}\right] + \left[\frac{I(1^{\text{L}})}{1}\right]} \quad (2)$$

$$F(L) = \frac{\frac{I(1^{\text{L}})}{1}}{\left[\frac{I(5^{\text{DA}}+5^{\text{DL}})}{4}\right] + \left[\frac{I(3^{\text{AD}}+3^{\text{AL}})}{4}\right] + \left[\frac{I(1^{\text{L}})}{1}\right]} \quad (3)$$

The experimental ester bond molar content (EB) in the resulting polymer can be calculated according to the equation 4:

$$EB(\%) = 100 \times \frac{2f(D)}{(2f(D)+f(L)} \quad (4)$$

The initial Amide/ester ratio of PALE, PALP, PALB and PALH polymers is 25/75, experimental determination of this ratio from the intensities of resonances of NMR spectra shows that these polymers possess very close experimental ester bond percentage (77.5%) and final monomer composition (38.3% of diol, 39.3% of Adipic acid and 22.2% of L-Alanine). In the same way for PALI, in which the final ester bond percentage is 72.9%, and it contains 35.3% of Isosorbide, 38.3% of Adipic acid and 26.2% of L-Alanine.

Differential scanning calorimetry and thermogravimetric data of these PEAs are summarized in table 5. The polymers are obtained in a totally amorphous state. It should be noted that the transition temperature (T_g) decreases when the aliphatic diol sequence becomes longer. This result is expected

since the aliphatic chain length in the polymer structure provides some flexibility which facilitates segmental rotations thus leads to human falls in (T_g) values.

While, the presence of cyclic units in the polymer PALI gives it some rigidity which is manifested by an increase in its glass transition temperature (20°C). DSC curves of these polymers are shown in figure 3. All PEAs are thermally stable and exhibit 5% mass loss temperatures ($T_{d,5\%}$) that can reach 320°C.

The intrinsic viscosities of all Poly(ester amide)s are evaluated in chloroform at 25°C, the results shown in table 5 indicate that these samples possess good intrinsic viscosities, that can reach 0.5 dl/g for PALP.

Table 5 presents also the values of M_w and \bar{D}_M of different copolymers. All polymers possess important molar masses (for PALB, M_w can reach 22680 g/mol) in the exception of PALI copolymer. The moderate molecular weight and intrinsic viscosity of this sample can be explicated by the difficulty of eliminating the excess of Isosorbide during the reaction, which has a high boiling temperature.

Table 5. Size exclusion chromatography (SEC), Intrinsic viscosity $[\eta_{int}]$ and thermal analyses (DSC, TGA), of PALD polymers: Mass-average molar mass (M_w), molar-mass dispersity (\bar{D}_M), glass transition temperature (T_g) and 5% mass loss temperature ($T_{d,5\%}$).

Polymer	M_w^* (g/mol)	\bar{D}_M^*	$[\eta_{int}]^{**}$ (dl/g)	T_g (°C)	$T_{d,5\%}$ (°C)
PALE	19080	2.0	0.36	-16	304
PALP	19450	2.1	0.50	-22	309
PALB	22680	2.4	0.40	-27	320
PALH	15580	2.2	0.22	-34	234
PALI	2780	1.8	0.09	20	224

3.2 Influence of Amide/Ester ratio

PALB-x/y poly(ester-amide)s were synthesized by changing the amide ester ratio of initial monomers, this variety in their composition has a notable effect on spectroscopic data, thermal properties, viscosity and SEC measurement of resulting polymers.

In FTIR spectra of PALB-50/50 to 10/90 copolymers, we observe the characteristic absorption bands corresponding to amide NH (a), amide I (d), and amide II (e) at 3300, 1648, and 1532 cm^{-1} , to aliphatic CH (b) at 1941 cm^{-1} , ester carbonyl (c) and at 1727, and C-O simple bond (f) at 1164 cm^{-1} . Their relative intensities vary in the expected way when the amide/ester ratio changes. For instance, decreasing L-alanine content clearly leads to a decrease of the amide I absorption which appears at 1648 cm^{-1} (peak (d)). (Fig 4).

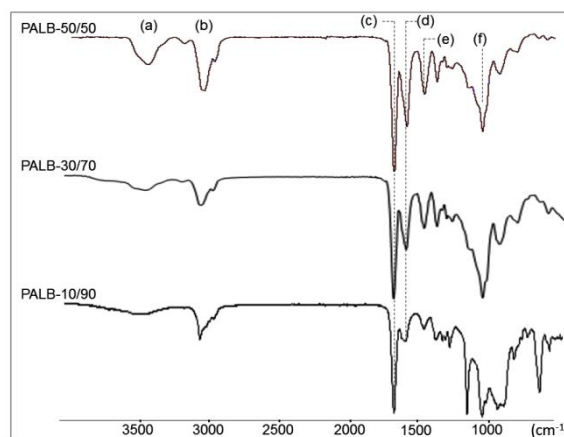


Figure 4. Infrared spectra of PALB-50/50, 30/70 and 10/90. See text for comments on absorptions (a)-(f)

All proton NMR spectra exhibit the expected signals relative to the different dyads mentioned in table 2, a typical spectrum of PALB-50/50 is shown in Fig.2-B. The resonances were assigned with the help of 2D $^1\text{H}/^1\text{H}$ (cosy 45) spectrum of PALB-50/50 shown in Fig. 5. In addition to 1^{L} and 2^{L} signals respectively at 4.56 and 1.40 ppm relative to amides sequences, and 3^{AB} and 5^{BA} signals respectively at 2.32 and 4.08 ppm relative to ester sequences, we observe also the expected signals related to mixed ester-amide dyads synonym of the good progress of the interchange reaction. The formation of these sequences is confirmed by the presence of 5^{BL} and 4^{AL} signals at 4.15 and 2.23 ppm respectively.

As mentioned above, the proton resonances of the $-\text{CH}-$ and $-\text{CH}_3$ of L-alanine units are not affected by the nature of neighboring units ($(1^{\text{L}} = 1^{\text{B}} = 1^{\text{A}} = 1^{\text{L}}$, observed at 4.56 ppm and $2^{\text{L}} = 2^{\text{B}} = 2^{\text{A}} = 2^{\text{L}}$, observed at 1.40 ppm)).

Monomer composition and ester bond percentage were calculated as previously from ^1H -NMR spectra following the equations 1, 2, 3 and 4. The summarized data in Table 6 show a good agreement between the

Table 6. Composition of PALB-x/y copolymers

Polymer	Composition			
	$f\text{B}$ (%)	$f\text{A}$ (%)	$f\text{L}$ (%)	EB (%)
PALB-50/50	33.3	36.3	30.3	68.7
PALB-40/60	34.3	35.3	30.3	69.3
PALB-30/70	37.3	38.3	24.2	75.5
PALB-20/80	40.4	42.4	17.1	82.4
PALB-10/90	43.8	45.9	10.2	89.5

Fig. 6 shows the ^{13}C -NMR spectrum of a representative polymer (PALB-50/50). Great complexity can be found, since multiple peaks are observed for each kind of carbon due to their sensitivity to the different neighbors, suggesting a non-block distribution of monomers.

Chemical shifts, and assignments related to the most significant carbons; $-\text{CO}$, $-\text{CH}_2\text{O}$, $-\text{CH}(\text{CH}_3)\text{-NH}$, $-\text{CH}_2\text{CO}$, $-\text{CH}_2\text{CHO}$, $-\text{CH}_2\text{CH}_2\text{CO}$ and $-\text{CH}_2$, are reported in table 7.

Signals near 65 ppm (attributed to the $\text{CH}_2\text{-O}$ carbon atom of a butanediol unit) appear split due to neighboring group effects. Four observed signals are attributed to four different sequences B-L-L, B-L-A, B-A-B and B-A-L. Note that these signals are split, since differences appear after only five or seven atoms for B-L and B-A dyads respectively.

final composition of PALB-x/y copolymers and the monomers feed ratio, with the exception of polymers PALB-50/50 and 40/60 having the higher L-Alanine fraction. In fact, they exhibit a slight increase in the final ester ratio, this is caused by the sublimation of L-alanine during the reaction.

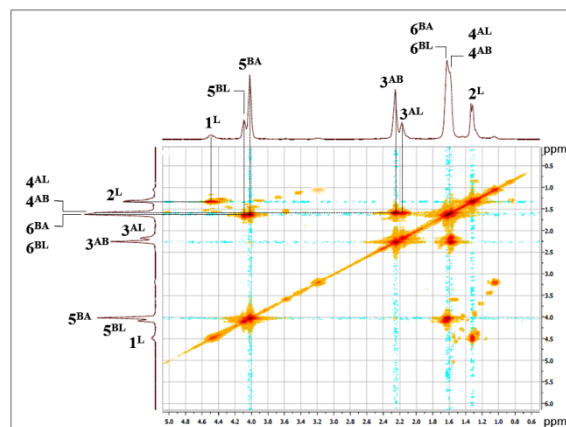


Figure 5. 2D ^1H - ^1H COSY NMR spectrum of PALB-50/50 copolymer (300 MHz, CDCl_3 , ref δ (CHCl_3) = 7.26 ppm)

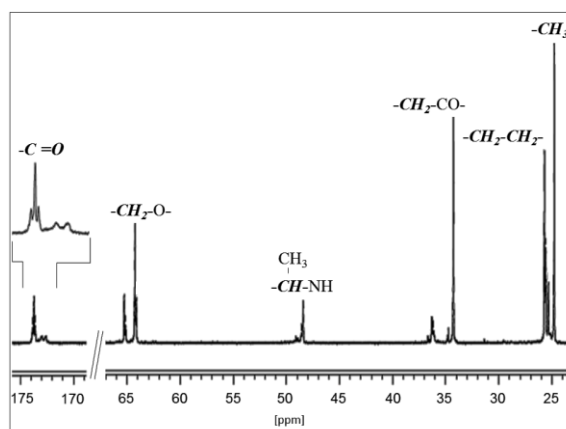


Figure 6. ^{13}C -NMR spectrum of PALB-50/50 showing zones associated to the $-\text{CO}$, $-\text{CHO}$, $-\text{CH}(\text{CH}_3)\text{-NH}$, $-\text{CH}_2\text{CO}$, $-\text{CH}_2\text{CH}_2-$ and $-\text{CH}_2$ carbons with their chemical shifts (ppm) (300 MHz, CDCl_3 , ref δ (CDCl_3) = 77.16 ppm)

The methylene adjacent to the CO group (Adipic unit) appears split into four signals. These signals are associated to the triads B-A-B, L-A-B, B-A-L or L-A-L, since chemical differences are found after only four atoms in the direction of the preceding monomer and one atom in the direction of the following monomer. As a general trend, sequences with ester groups move downfield with respect to similar ones constituted by amide groups. This fact, together with the displacements deduced from the reference polymers, allows the assignment given in table 7 to be proposed. Much more complicated is the assignment of signals corresponding to the methylene adjacent to other

methylene groups that appears near 25 ppm and that can belong either to a butanediol or an adipic unit. The observed signals are associated to seven possible triads taking into account the influence of adjacent units on the chemical shift value of the observed signal.

It should be noted that the resonances corresponding on L-Alanine methyl groups are not affected by the nature of neighboring units and appear at 24.77 ppm, while -CH- carbons are manifested by two signals at 48.41 and 48.59 ppm depending on the nature of the adjacent unit.

Table 7. Chemical shifts, and assignments of the ^{13}C -NMR spectrum of PALB-50/50

	Sequence	δ (ppm)
L-B	-CO-NH-CH(CH ₃) <u>CO</u> *-O-	173.85
B-A-B	-O-CO(CH ₂) ₄ <u>CO</u> -O-	173.72
L-A-B	-NH-CO(CH ₂) ₄ <u>CO</u> -O-	173.60
L-L-L	-CO-NH-CH(CH ₃) <u>CO</u> -NH-CH(CH ₃)CO-	173.00
A-L	-CO(CH ₂) ₄ <u>CO</u> -NH-CH(CH ₃)CO-	172.61
B-L-L	- <u>CH</u> ₂ O-CO-CH(CH ₃)-NH-CO-CH(CH ₃)NH-	65.28
B-L-A	- <u>CH</u> ₂ O-CO-CH(CH ₃)-NH-CO(CH ₂) ₄ CO-	65.15
B-A-B	- <u>CH</u> ₂ O-CO(CH ₂) ₄ CO-O-	64.27
B-A-L	- <u>CH</u> ₂ O-CO(CH ₂) ₄ CO-NH-	64.14
B-L-L	-O-CO- <u>CH</u> (CH ₃)-NH-CO-CH(CH ₃)NH-	48.59
B-L-A	-O-CO- <u>CH</u> (CH ₃)-NH-CO(CH ₂) ₄ CO-	48.59
L-L-L	-NH-CO- <u>CH</u> (CH ₃)-NH-CO-CH(CH ₃)NH-	48.41
L-L-A	-NH-CO- <u>CH</u> (CH ₃)-NH-CO(CH ₂) ₄ CO-	48.41
B-A-B	-O-CO(CH ₂) ₃ <u>CH</u> ₂ CO-O-	36.30
L-A-B	-NH-CO(CH ₂) ₃ <u>CH</u> ₂ CO-O-	36.14
B-A-L	-O-CO(CH ₂) ₃ <u>CH</u> ₂ CO-NH-	34.74
L-A-L	-NH-CO(CH ₂) ₃ <u>CH</u> ₂ CO-NH-	34.26
A-B-L	-CO-OCH ₂ CH ₂ <u>CH</u> ₂ CH ₂ O-COCH(CH ₃)NH-	25.70
L-B-A	-NHCH(CH ₃)CO-OCH ₂ CH ₂ <u>CH</u> ₂ CH ₂ O-CO-	25.70
A-B-A	-CO-OCH ₂ <u>CH</u> ₂ <u>CH</u> ₂ CH ₂ O-CO-	25.70
B-A-B	-O-COCH ₂ <u>CH</u> ₂ <u>CH</u> ₂ CH ₂ CO-O-	25.58
L-A-B	-NH-COCH ₂ CH ₂ <u>CH</u> ₂ CH ₂ CO-O-	25.58
B-A-L	-CH ₂ O-COCH ₂ CH ₂ <u>CH</u> ₂ CH ₂ CO-NH-	25.33
L-A-L	-NH-COCH ₂ <u>CH</u> ₂ <u>CH</u> ₂ CH ₂ CO-NH-	25.33
B-L-A	-O-COCH(<u>CH</u> ₃)NH-CO(CH ₂) ₄ CO-	24.77
B-L-L	-O-COCH(<u>CH</u> ₃)NH-COCH(CH ₃)-NH-	24.77
L-L-A	-NH-COCH(<u>CH</u> ₃)NH-CO(CH ₂) ₄ CO-	24.77
L-L-L	-NH-COCH(<u>CH</u> ₃)NH-COCH(CH ₃)NH-	24.77

(*) carbon attributed

As expected, the DSC results of PALB-x/y copolymers show a clear relationship of the T_g values with the Amide/ester ratio. Indeed, increasing the fraction of L-alanine in the polymer composition improves its glass transition temperature, due to the formation of intermolecular hydrogen bonds. These polymers are thermally stable and exhibit 5% mass loss temperatures ($T_{d,5\%}$) above 280°C (Table 8). They are totally amorphous, in the exception of PALB-10/90 which possesses a semi-crystalline structure with a melting temperature in the order of 28°C. This is clearly due to its very high ester ratio.

Very important intrinsic viscosities and molecular weights were obtained for PALB-x/y polymers (Table 8), however we noticed that the increase in L-alanine molar fraction in the initial mixture leads to a molar mass decrease of polymers. A similar negative effect of amino-acids on molar mass has been reported for the synthesis of glycine or β -alanine based PEAs and was interpreted by a partial catalyst deactivation due to interactions between titanium and amine and/or amide groups present during the reaction (15, 16).

Table 8. Size exclusion chromatography (SEC), Intrinsic viscosity $[\eta_{int}]$ and thermal analyses (DSC, TGA), and of PALB-x/y polymers: Mass-average molar mass (M_w), molar-mass dispersity (D_M), glass transition temperature (T_g), melting point (T_m), melting enthalpy (ΔH_m) and 5% mass loss temperature ($T_{d,5\%}$).

Polymer	M_w^* (g/mol)	D_M^*	$[\eta_{int}]^{**}$ (dl/g)	T_g (°C)	T_m (°C)	ΔH_m (J/g)	$T_{d,5\%}$ (°C)
PALB-50/50	6430	2.7	0.16	-10	-	-	284
PALB-40/60	9170	2.2	0.24	-14	-	-	281
PALB-30/70	11220	1.9	0.75	-14	-	-	311
PALB-20/80	32380	2.0	0.88	-27	-	-	320
PALB-10/90	41800	2.7	1.06	-42	28	2.6	330

*Determined by SEC using polystyrene standards.

** 1.5 dl/g of polymer in $CHCl_3$ at 25°C.

Conclusion

In this work we have studied the synthesis and characterization of a series of poly(ester-amide)s derived from L-Alanine, adipic acid and five different diols. The Infrared and NMR results are fully consistent with their anticipated chemical structures. Final monomer composition of all PEAs was evaluated from 1H -NMR spectra, the resulting data show a good agreement between the final composition and the monomer feed ratio. All resulting polymers are thermally stable to temperatures that could reach 330°C. We noticed the influence of the nature of used diol on the glass transition temperature values (T_g) of PALD polymers, indeed this temperature decreases when the aliphatic sequence of the diol is longer. The use of a diol having a heterocyclic structure (isosorbide) increases the T_g value, and hence improve the thermal properties of the resulting polymer. The impact of Amide/ester ratio on thermal properties was studied through PALB-x/y polymers. As expected, the increase in amino acid content leads to an increase in the glass transition temperature. These polymers possess very high inherent viscosities that could reach 1.06 dl/g for PALB-10/90, and therefore very important molecular weights ($M_w=41800$ g/mol).

References

- (1) Rodriguez-Galan, A., Franco, L. & Puiggali, J. Biodegradable poly(ester amide)s: Synthesis and applications. In Biodegradable polymers: Processing, degradation (ed. Gary P. Felton) Ch. 4, 207-271 (2011 Nova Science Publishers, Inc)
- (2) Armelin, E., Franco, L., Rodriguez-Galan, A. & Puiggali, J. Study on the Degradability of Poly(ester amide)s Related to Nylons and Polyesters 6,10 or 12,10. *Macromol. Chem. Phys.* **203**, 48-58 (2002).
- (3) Rodriguez-Galan, A., Franco, L. & Puiggali, J. Degradable Poly(ester amide)s for Biomedical Applications. *Polymers*, **3**, 65-99 (2011).
- (4) Ouchi, T., Hamada, A. & Ohya, Y. Biodegradable microspheres having reactive groups prepared from L-lactic acid-depsipeptide copolymers. *Macromol. Chem. Phys.* **200**, 436-441 (1999)
- (5) Li, L. & Chu, C.C. Nitroxyl radical incorporated electrospun biodegradable poly (ester amide) nanofiber membranes. *J. Biomater. Sci. Polym. Ed.* **20**, 341-361 (2009).

- (6) Knight, D. K., Gillies, E. R. & Mequanint, K. Strategies in Functional Poly(ester amide) Syntheses to Study Human Coronary Artery Smooth Muscle Cell Interactions. *Biomacromolecules*. **12**, 2475-2487 (2011).
- (7) Knight, D. K., Stutchbury, R., Imruck, D., Halfpap, C., Lin, S., Langbein, U., Gillies, E. R., Mittler, S. & Mequanint, K. Focal Contact Formation of Vascular Smooth Muscle Cells on Langmuir-Blodgett and Solvent-Cast Films of Biodegradable Poly(ester amide)s. *ACS Appl. Mater. Interfaces*. **4**, 1303-1312 (2012).
- (8) Karimi, P., Rizkalla, A. S. & Mequanint, K. Versatile biodegradable poly (ester amide) s derived from α -amino acids for vascular tissue engineering. *Materials*. **3**, 2346-2368 (2010).
- (9) John, G. & Morita, M. Synthesis and Characterization of Photo-Cross-Linked Networks Based on L-Lactide/Serine Copolymers. *Macromolecules*. **32**, 1853-1858 (1999).
- (10) Guo, K. & Chu, C. C. Controlled release of paclitaxel from biodegradable unsaturated poly (ester amide) s/poly (ethylene glycol) diacrylate hydrogels. *J. Biomater. Sci. Polymer Edn*. **18**, 489-504 (2007).
- (11) Helder, J., Kohn, F. E., Sato, S., van den Berg, J. W. & Feijen, J. Synthesis of poly [oxyethylidenecarbonylimino-(2-oxoethylene)][poly (glycine-D, L-lactic acid)] by ring opening polymerization. *Makromol. Chem., Rapid Commun*. **6**, 9-14 (1985).
- (12) John, G., Tsuda, S. & Morita, M. Synthesis and modification of new biodegradable copolymers: Serine/glycolic acid based copolymers. *J. Polym. Sci., Part A: Polym. Chem*. **35**, 1901-1907 (1997).
- (13) Feng, Y., Knufermann, J., Klee, D. & Hocker, H. Enzyme-catalyzed ring-opening polymerization of 3(S)-isopropylmorpholine-2,5-dione. *Macromol. Rapid Commun*. **20**, 88-90 (1999).
- (14) Feng, Y., Knufermann, J., Klee, D. & Hocker, H. Lipase-catalyzed ring-opening polymerization of 3(S)-isopropylmorpholine-2,5-dione. *Macromol. Chem. Phys*. **200**, 1506-1514 (1999).
- (15) Mohamed, A. A., Salhi, S., Abid, S., El Gharbi, R. & Fradet A. Random polyesteramides based on ϵ -caprolactone and glycine. *J. Appl. Polym. Sci*. **131**, 40573 (2014).
- (16) Mohamed, A. A., Salhi, S., Abid, S., El Gharbi, R. & Fradet A. Random and quasi-alternating polyesteramides deriving from ϵ -caprolactone and β -alanine. *Eur. Polym. J*. **53**, 160-170 (2014).
- (17) Qian, Z., Li, S., He, Y., Li, C. & Liu, X. Synthesis and thermal degradation of biodegradable polyesteramide based on ϵ -caprolactone and 11-aminoundecanoic acid. *Polym. Degrad. Stab*. **81**, 279-286 (2003).
- (18) He, Y., Du, Y. & Liu, X. Synthesis, characterization and properties of polyesteramide based on ϵ -caprolactone and 6-aminohexanoic acid. *Adv. Mater. Res*. **1581**, 287-290 (2011).
- (19) Katsarava, R., Beridze, V., Arabuli, N., Kharadze, D., Chu, C. C. & Won, C. Y. Amino acid-based bioanalogous polymers. Synthesis, and study of regular poly(ester amide)s based on bis(α -amino acid) α,ω -alkylene diesters, and aliphatic dicarboxylic acids. *J. Polym. Sci., Part A: Polym. Chem*. **37**, 391-407 (1999).
- (20) Guo, K. & Chu, C. C. Synthesis, Characterization, and Biodegradation of Novel Poly(ether ester amide)s Based on L-Phenylalanine and Oligoethylene Glycol. *Biomacromolecules*. **8**, 2851-2861 (2007).
- (21) Deng, M., Wu, J., Reinhart-King, C. A. & Chu, C. C. Synthesis and Characterization of Biodegradable Poly(ester amide)s with Pendant Amine Functional Groups and In Vitro Cellular Response. *Biomacromolecules*. **10**, 3037-3047 (2009).
- (22) Pang, X. & Chu, C. C. Synthesis, characterization and biodegradation of functionalized amino acid-based poly(ester amide)s. *Biomaterials*. **31**, 3745-3754 (2010).
- (23) Pang, X., Wu, J., Reinhart-King, C. & Chu, C. C. Synthesis and characterization of functionalized water soluble cationic poly(ester amide)s. *J. Polym. Sci., Part A: Polym. Chem*. **48**, 3758-3766 (2010).
- (24) Song, H. & Chu, C. C. Synthesis and characterization of a new family of cationic amino acid-based poly(ester amide)s and their biological properties. *J. Appl. Polym. Sci*. **124**, 3840-3853 (2012).

- (25) Deng, M., Wu, J., Reinhart-King, C. A. & Chu, C. C. Biodegradable functional poly(ester amide)s with pendant hydroxyl functional groups: Synthesis, characterization, fabrication and in vitro cellular response. *Acta Biomaterialia*. **7**, 1504-1515 (2011).
- (26) Wu, J., Mutschler, M. A. & Chu, C.C. Synthesis and characterization of ionic charged water soluble arginine-based poly(ester amide). *J Mater Sci: Mater Med*. **22**, 469-479 (2011).
- (27) Paredes, N., Rodriguez-Galan, A., Puiggali, J. & Peraire, C. Studies on the biodegradation and biocompatibility of a new poly(ester amide) derived from L-alanine. *J. Appl. Polym. Sci.* **69**, 1537-1549 (1998)
- (28) Rodriguez-Galan, A., Pelfort, M., Aceituno, J. E., Puiggali, J. Comparative studies on the degradability of poly (ester amide) s derived from L-and L, D-alanine. *J. Appl. Polym. Sci.* **74**, 2312-2320 (1999).
- (29) Rodriguez-Galan, A., Fuentes, L. & Puiggali, J. Studies on the degradability of a poly (ester amide) derived from L-alanine, 1, 12-dodecanediol and 1, 12-dodecanedioic acid. *Polymer*. **41**, 5967-5970 (2000).
- (30) Armelin, E., Paracuellos, N., Rodriguez-Galan, A., Puiggali, J. Study on the degradability of poly (ester amide) s derived from the α -amino acids glycine, and l-alanine containing a variable amide/ester ratio. *Polymer*. **42**, 7923-7932 (2001).
- (31) Puiggali, J. & Subirana, J. A. Synthetic polymers containing α -amino acids: from polyamides to poly (ester amide) s. *J. Pept. Sci.* **11**, 247-249 (2005).
- (32) Paredes, N., Rodriguez-Galan, A. & Puiggali, J. Synthesis and characterization of a family of biodegradable poly (ester amide) s derived from glycine. *J. Polym. Sci., Part A: Polym. Chem.* **36**, 1271-1282 (1998).
- (33) Paredes, N., Casas, M. T. & Puiggali, J. Poly (ester amide) s derived from glycine, even-numbered diols, and dicarboxylic acids: Considerations on the packing. *J. Polym. Sci., Part B: Polym. Phys.* **39**, 1036-1045 (2001).
- (34) Paredes, N., Casas, M. T. & Puiggali, J. Packing of sequential poly (ester amide) s derived from diols, dicarboxylic acids, and amino acids. *Macromolecules*. **33**, 9090-9097 (2000).
- (35) P. Karimi , A. S. Rizkalla et K. Mequanint, Versatile biodegradable poly (ester amide) s derived from α -amino acids for vascular tissue engineering. *Materials*. **3**, 2346-2368 (2010).
- (36) Montane, J., Armelin, E., Asin, L., Rodriguez-Galan, A. & Puiggali, J. Comparative degradation data of polyesters and related poly (ester amide) s derived from 1, 4-butanediol, sebacic acid, and α -amino acids. *J. Appl. Polym. Sci.* **85**, 1815-1824 (2002).
- (37) Asin, L., Armelin, E., Montané, J., Rodriguez-Galan, A. & Puiggali, J. Sequential poly(ester amide)s based on glycine, diols, and dicarboxylic acids: Thermal polyesterification versus interfacial polyamidation. Characterization of polymers containing stiff units. *J. Polym. Sci., Part A: Polym. Chem.* **39**, 4283-4293 (2001).
- (38) Casas, M. T., Gestí, S., & Puiggali, J. Structural data on regular poly (ester amide) s derived from even diols, glycine, and terephthalic acid. *Cryst. Growth Des.* **5**, 1099-1107 (2005).
- (39) Botines, E., Rodriguez-Galan, A. & Puiggali, J. Poly (ester amide) s derived from 1, 4-butanediol, adipic acid and 1, 6-aminohexanoic acid: characterization and degradation studies. *Polymer*. **43**, 6073-6084 (2002).
- (40) Ferré, T., Franco, L., Rodriguez-Galan, A. & Puiggali J. Poly (ester amide) s derived from 1, 4-butanediol, adipic acid and 6-aminohexanoic acid. Part II: composition changes and fillers. *Polymer*. **44**, 6139-6152 (2003).
- (41) Mahfoudh, J., Salhi, S., Auguste, A., Delaite, C., Abid, S. & El Gharbi, R. Random Polyesteramides Based on Glycolic Acid and β -Alanine. *J. Macromol. Sci., Pure Appl. Chem.* **54**, 280-285 (2015).
- (42) Abbes, M., Salhi, S., Lefevre, L., Delaite, C., Abid, S. & El Gharbi, R. Poly(ester-amide)s Derived From Adipic Acid, 1,4-Butanediol and β -Alanine: Synthesis and Characterization. *J. Macromol. Sci., Pure Appl. Chem.* **52**, 56-63 (2015).
- (43) Solomon, O. F. & Ciuta, I. Z. Détermination de la viscosité intrinsèque de solutions de polymères par une simple détermination de la viscosité. *J. Appl. Polym. Sci.* **24**, 683-686 (1962).
- (44) G. Seretoudi, D. Bikiaris, C. Panayiotou, Synthesis, characterization and biodegradability of poly (ethylene succinate)/poly (ϵ -caprolactone) block copolymers. *Polymer*. **43**, 5405-5415 (2002).

Quartz sand beneficiation using magnetic and electrostatic separation to glass industries

Ben Fradj Manel¹, Gallala Wissem² and Abdeljaouad Saadi¹

¹ *Geology Department, Faculty of Sciences, Tunis-El Manar University, Tunisia.*

² *Higher Institute Of Fine Arts, University of Sousse, Tunisia.*

bf.manel@hotmail.fr

Received date: May 06, 2016; revised date: June 28, 2016; accepted date: June 28, 2016

Abstract

Quartz sand of Fortuna formation was assigned to the Oligo-Miocene. This formation outcrops in Central Tunisia, particularly in the Ain Bou Morra area. The grain particle size ranges from fine to medium. The morphoscopic analysis shows that the useful fraction (100-630 μ m) consists essentially of transparent quartz grains. The mineralogical study of samples after separation in heavy liquid indicates that they contain a small amount of heavy minerals such as: tourmaline, zircon and staurotide. The X-ray diffraction analysis of the total rock revealed that quartz is the major mineral constituent of sand. Chemical analysis shows high content of SiO₂. Coloring elements (Fe₂O₃) and (TiO₂) are slightly elevated. The study aim was to remove impurities from silica sand, in order to upgrade quartz sands and to produce material that has a higher potential value for industrial manufacturing processes. Several processing physical techniques (attrition, gravity, magnetic and electrostatic separation) have been developed. The obtained material after treatment was characterized using Atomic Absorption Spectroscopy (AAS) and Inductively Coupled Plasma Atomic Emission Spectroscopy (ICP-AES). Chemical results through the combined techniques show a significant increase of impurities (such as Fe, Ti, Cr ...) and a significant increase of SiO₂. The final concentrate achieved 99.99 % SiO₂, 8 ppm Fe₂O₃ and 6 ppm TiO₂ was obtained, at the optimum operating conditions, from an ore containing about 98.8% SiO₂, 0.16% Fe₂O₃ and 0.05% TiO₂. The treated sand has been found to be a satisfactory material conforms to the requirements of optical glass, crystallaboratory glass and photovoltaic cells.

Keywords: Attrition, Electrostatic and magnetic separation. Quartz sand.

1. Introduction

Silica sand industry in Tunisia has been growing rapidly due to increased demand from civil engineering, pharmaceutical practices, chemical, foundries, glass, ceramic, electronics and photovoltaic industries. However, the glassmaking is an important component in the glass production accounting for around 65 to 70% wt of total raw material input.

The specifications made on glassmaking sands (Harben and Kuzvart 1997) are defined essentially by their chemical composition (SiO₂, Al₂O₃, Fe₂O₃ and TiO₂) and by the useful granulometric fraction (0.1 to 0.6 mm). A high content of SiO₂ which is more than 98% is combined with low impurities (%Fe₂O₃ must be

lower than 0.2%). This kind of raw sand, called extra-siliceous sand is very abundant in Tunisia, especially in Oligocene and Miocene outcrops. Different authors have been studied the characterization of these sand deposits (Griffiths 1987; El Maaoui 1993; Jourirou 1981; Louhaichi 1981; Trabelsi 1988; Jamoussi 1991; Added 2005; Ben Fradj 2010). However, few works carried out on the purification and beneficiation process (Aloui, 2010; Gallala et al. 2009; Gallala 2010; Gaied & Gallala 2011)

Depending on the degree of purification described can hold two treatment schedules, which were tested in this study.

- The first schema contains the size classification before and after attrition followed by a dry magnetic separation.

A wet screening on 1.7 to 1mm before attrition to remove large and mid-large quartz coated tablets which can cause mechanical problems within the attrition cell.

A classification after attrition ranging from 0.1 to 0.63 mm was used, in order to recover the useful fraction and remove the fine fraction below 0.1 mm. The latter has contents in harmful elements significantly higher than the coarse fractions.

This scheme allows the preparation of purified sands with iron contents of about 300 to 400 ppm and a 68% weight yield for Aquitania sand from Ain Bou Morra.

- The second scheme includes more gravity separation, between the attrition operation and high intensity magnetic separation wet and still followed by electrostatic separation. This scheme was applied on three composite samples of sand Ain Bou Morra helped prepare sands much more refined, with iron content in the order of 9ppm and a weight of 76% yield.

2. Geological Setting

The study area is located in the region of Ain Bou Morra. It is 20 Km from west of Sbikha village

(governorate of Kairouan, central Tunisia.).

The site is located east of the sub-meridian structure Boudabouss. The area is covered by the geological Djebibina map.

In this region the series show outcrop of Tertiary age deposits .These deposits are affected by sub-meridian direction of wrinkles. The sands studied belong to the upper Fortuna formation of Aquitanian age.

The series are composed of three lithological units from the bottom to the top (Figure 2):

- Lower unit: it shows 30 m thick sand-clay alternations covered by a large mass of misclassified sand that exceeds 70 m thick. Indeed, this basal series is in the form of consolidated sandstone rock benches with a general rate of granular decreasing sequences stratified sandstones.

- Middle unit: with 200 m thick, it is characterized by medium particle size sand with cross-stratification.

- Upper unit: with 345 m thick, it is characterized fine sand very ranked well.

The sands are organized in decreasing size sequences with coarse sand quartz at the bottom and finer sand at the top of each sequence.

The sequences are intercalated by centimetric clay layers

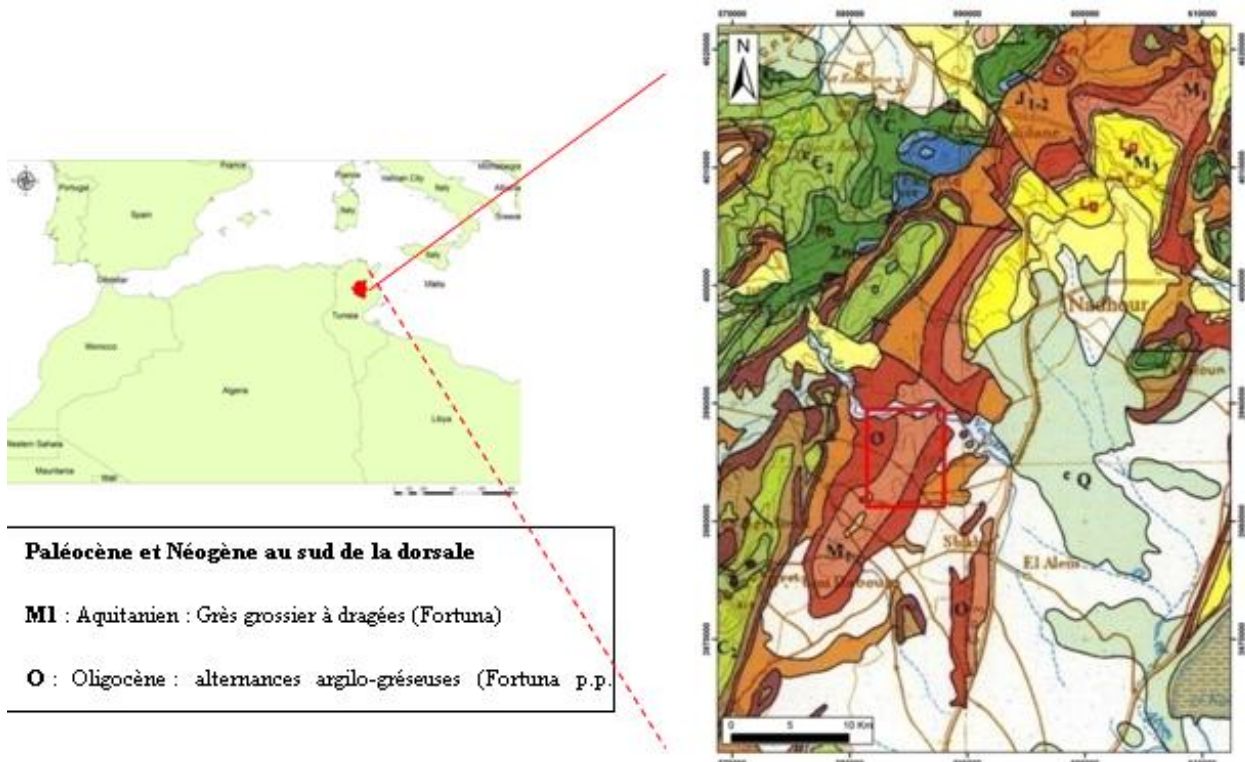
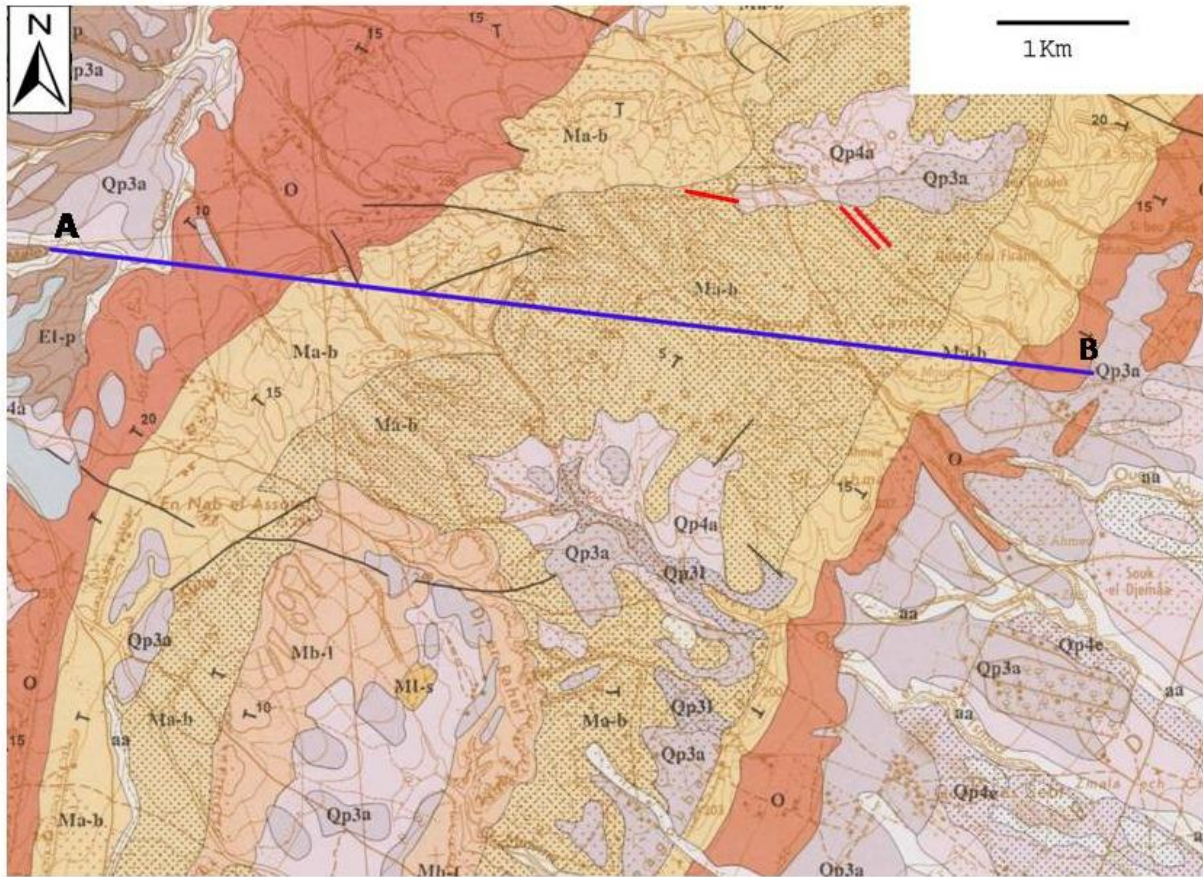


Figure 1 : Location of the study area on an extract of the geological map 1/500 000 of Tunisia



— Location of the studied samples.

MI - s : Langhien - Serravallien, Clay interbedded of sands (MAHMOUD). **Mb -I : Burdigalien supérieur - Langhien**, Sandy limestone with bioplaste (AIN GRAB). **Ma -b : aquitanien - Burdigalien** a- coarse sandstone with quartz dragees (EL HAOURIA higher), b- Alternating sandstone and clay (EL HAOURIA lower). **O : Oligocène** Clay interbedded with sands and limestones

Figure 2 : Location of the study site at the geological map Djebibina of 1:50 000.

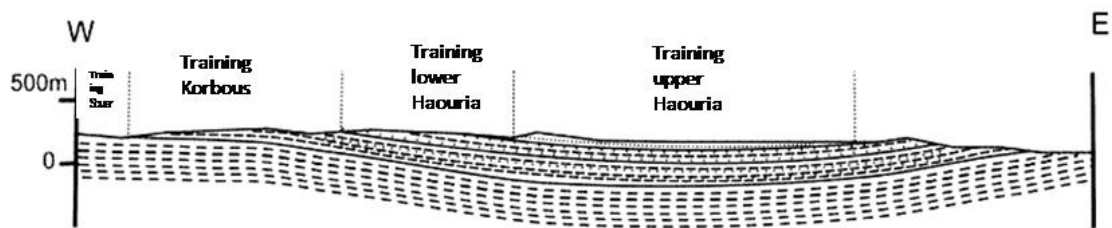


Figure 3 : Geological section in the region of Ain Bou Morra

3. Material and methods

Sand samples were collected by making grooves perpendicular to the outcrops and after etching the

surface. The samples were mixed to prepare a fairly representative sample of each faces. The obtained sample has undergone several quartages to obtain similar samples with equal amount for analytical processing.

The representative ore sample is obtained from Ain Bou Morra Province, Tunisia. For the determination of granulometric distribution, standard sieves from the series "AFNOR" were used.

Major elements were analyzed by Atomic Absorption Spectrophotometer (AAS) "Perkin Elmer" 3300. In addition for monitoring minor and trace elements, the Inductively Coupled Plasma Atomic Emission Spectrometer (ICP-AES) (ULTIMA-C) was employed. The mineralogical analysis was carried out using stereomicroscopy, petrographic microscope and X-ray diffraction "X' Pert Pro MPD PANalytical" using Cu K α radiation operating at 40KV and 20mA were used.

The heavy minerals separation was carried out by the standard tetrabromoethane technique (specific gravity 2.96). In this case, the attrition was done using Wemco cell (sand scrubber).

This process consisted of conditioning the sample at 70% solids during 15min. Size fractions from +0.1 to 0.63 mm were used for gravity separation by shaking table. Dry magnetic separator (15000 Gauss), wet high intensity magnetic separator (20,000 Gauss) and electrostatic separator (25 to 30KV) from Carpc were respectively used for magnetic separation and

electrostatic separation tests as well. These two tests were carried out at the laboratory of Liege University.

4. Results and discussion

4.1 First method of treatment

The first method includes three stages: the classification (screening) before and after attrition followed by a dry magnetic separation.

4.2 Raw Sand characterization

4.2.1 Mineralogical analysis

The observation under a binocular microscope shows transparent grains with irregular shape. About 99% of the grains are formed by small quartz grains.

The raw samples under the binocular microscope, X-ray diffraction analysis: were conducted XRD reveals the dominance of quartz phase (3.34 Å) for the analysis of medium sand samples.

However XRD analysis for the fraction > 2 μ m identified the presence of kaolin and illite clay.

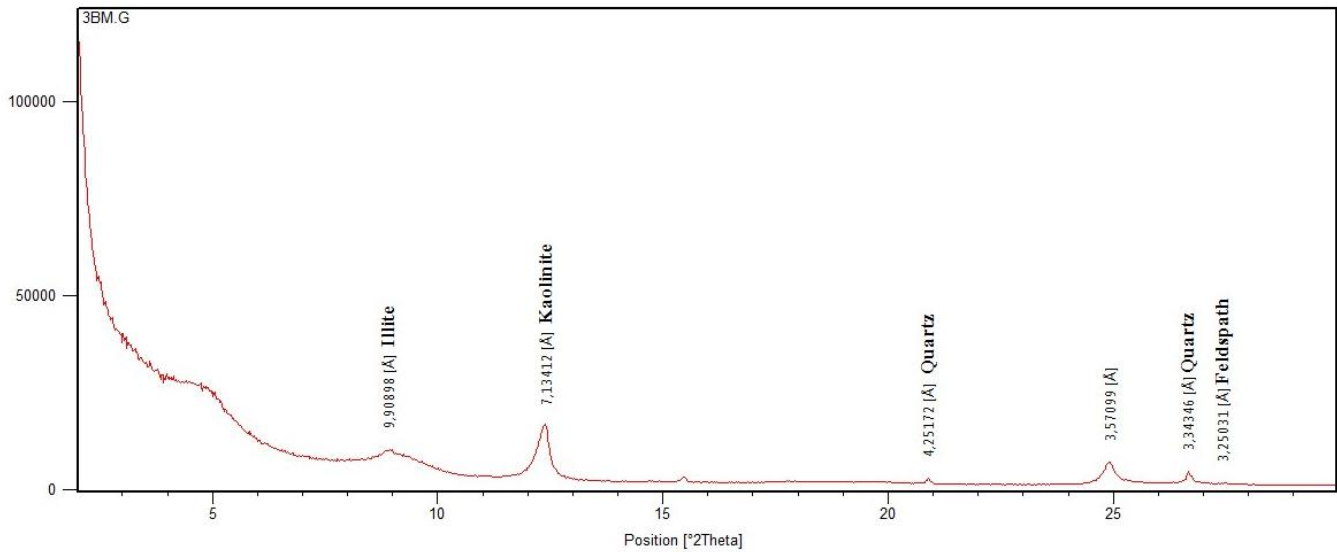


Figure 4 : X ray diffractogram clay treated with ethylene glycol

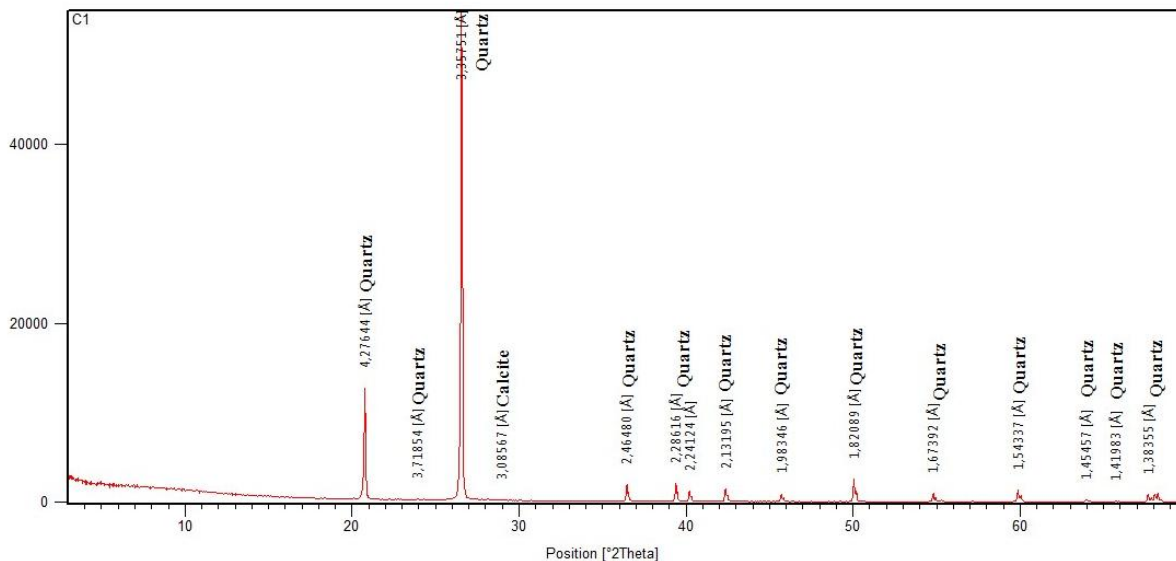


Figure 5 : X ray diffractogram of clay heated at 550°C

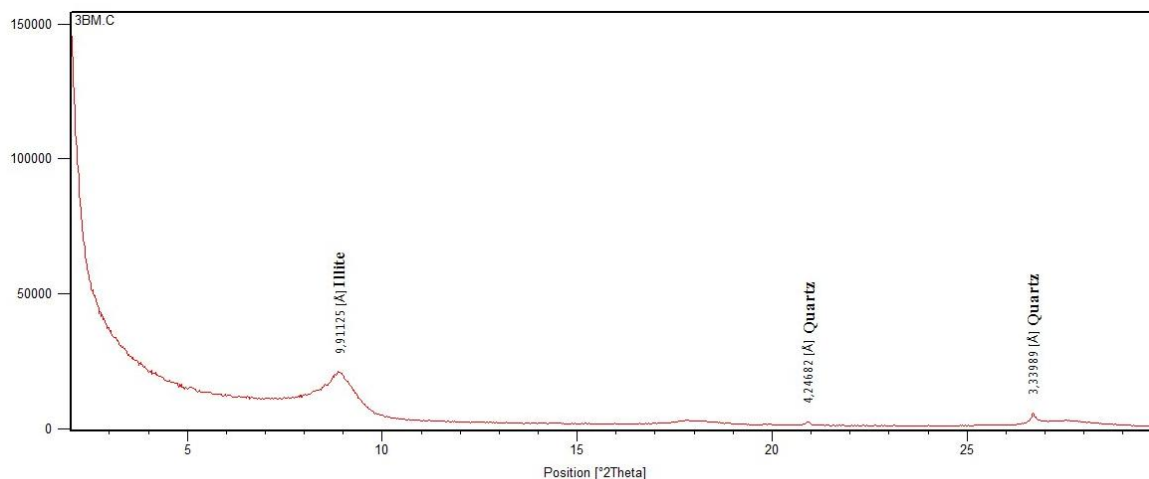


Figure 6 : X ray diffractogram powder of raw sample 1

4.2.2 Chemical and grain size analysis

Results of chemical analyses (Table 1) reveal that quality of silica sand is reasonable but some high impurities make uncertainty to produce high grade glass or photovoltaic cells. Major elements, mainly (SiO₂), ranges from 98.69 % to 99.55wt% which gives an extra siliceous character for the sand (Table 1).

Although contents, in some samples, of Al₂O₃ (0.25 to 0.47 wt %), Na₂O (0.012-0.017 wt%), K₂O (0.11-0.17 wt%) are not tolerable, but it is possible to remove or decrease .

These elements which are concentrated in the clay fractions. Major impurities, qualified as penalizing agent in the glass industry, mainly Fe₂O₃ and TiO₂ range respectively from 0.12 to 0.17 wt% and from 0.033 to 0.08 Wt%. These contents are outside the specifications for high grade glass. In order to obtain satisfactory product, it is primordial to upgrade the raw materials.

Table 1 : Chemical analysis of raw sand samples

Sample	SiO ₂ %	Al ₂ O ₃ %	CaO %	Fe ₂ O ₃ %	K ₂ O %	MgO %	Na ₂ O %	TiO ₂ %	Cr (ppm)	Cu (ppm)
Sample 1	99.39	0.25	0.07	0.12	0.11	0.010	0.012	0.033	9	8
Sample 2	99.17	0.29	0.09	0.15	0.13	0.015	0.017	0.04	10	9
Sample 3	98.69	0.47	0.11	0.17	0.17	0.07	0.016	0.08	9	9

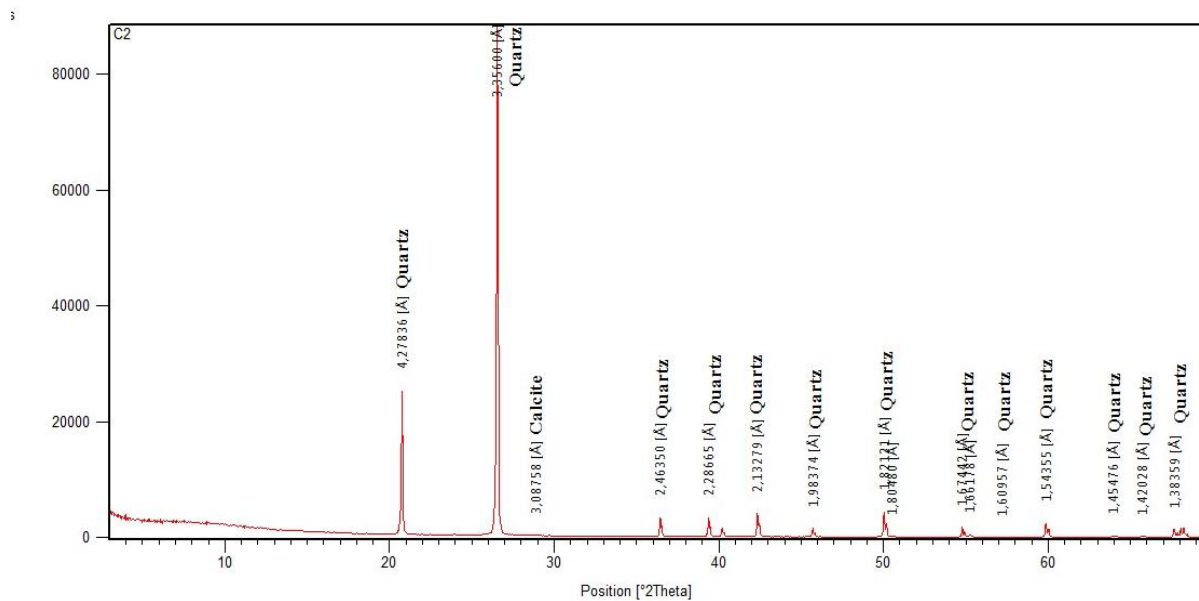


Figure 7 : X ray diffractogram powder of raw sample 2

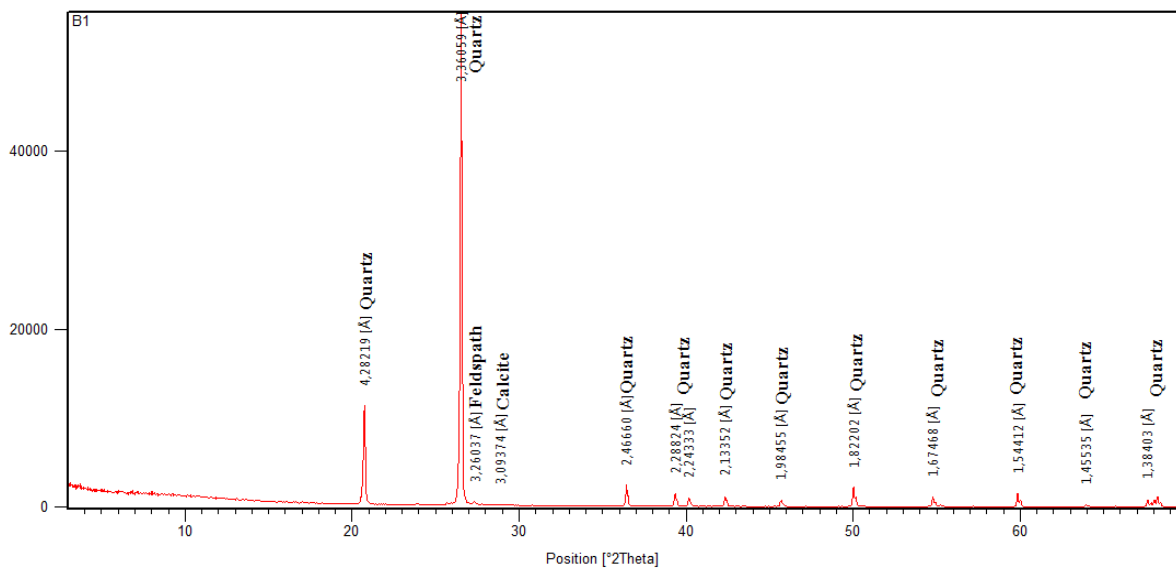


Figure 8 : X ray diffractogram powder of raw sample 3

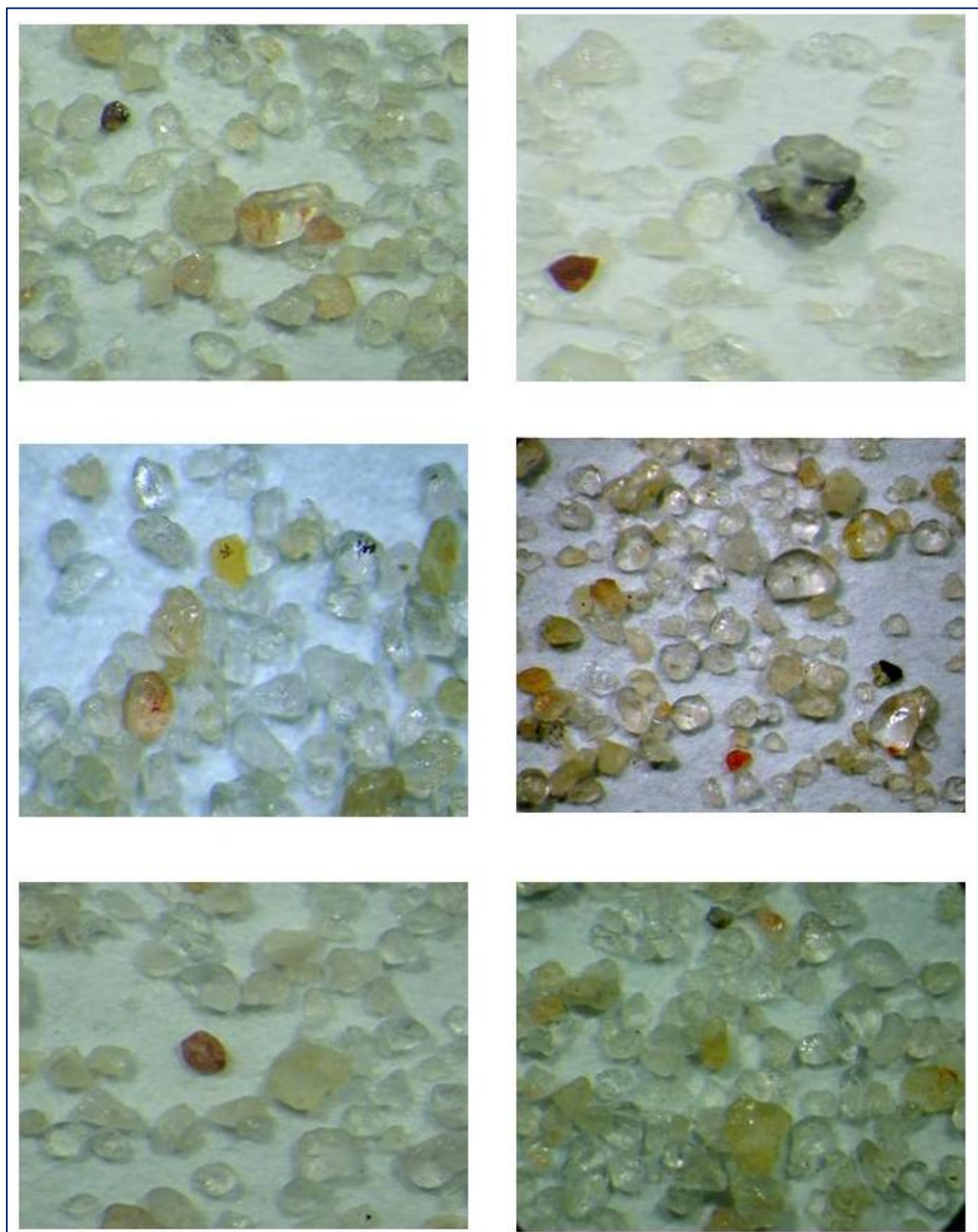


Plate 1 : photos of Mineralogical identification of the conductive portion of Fortuna sand Ain Bou Morra

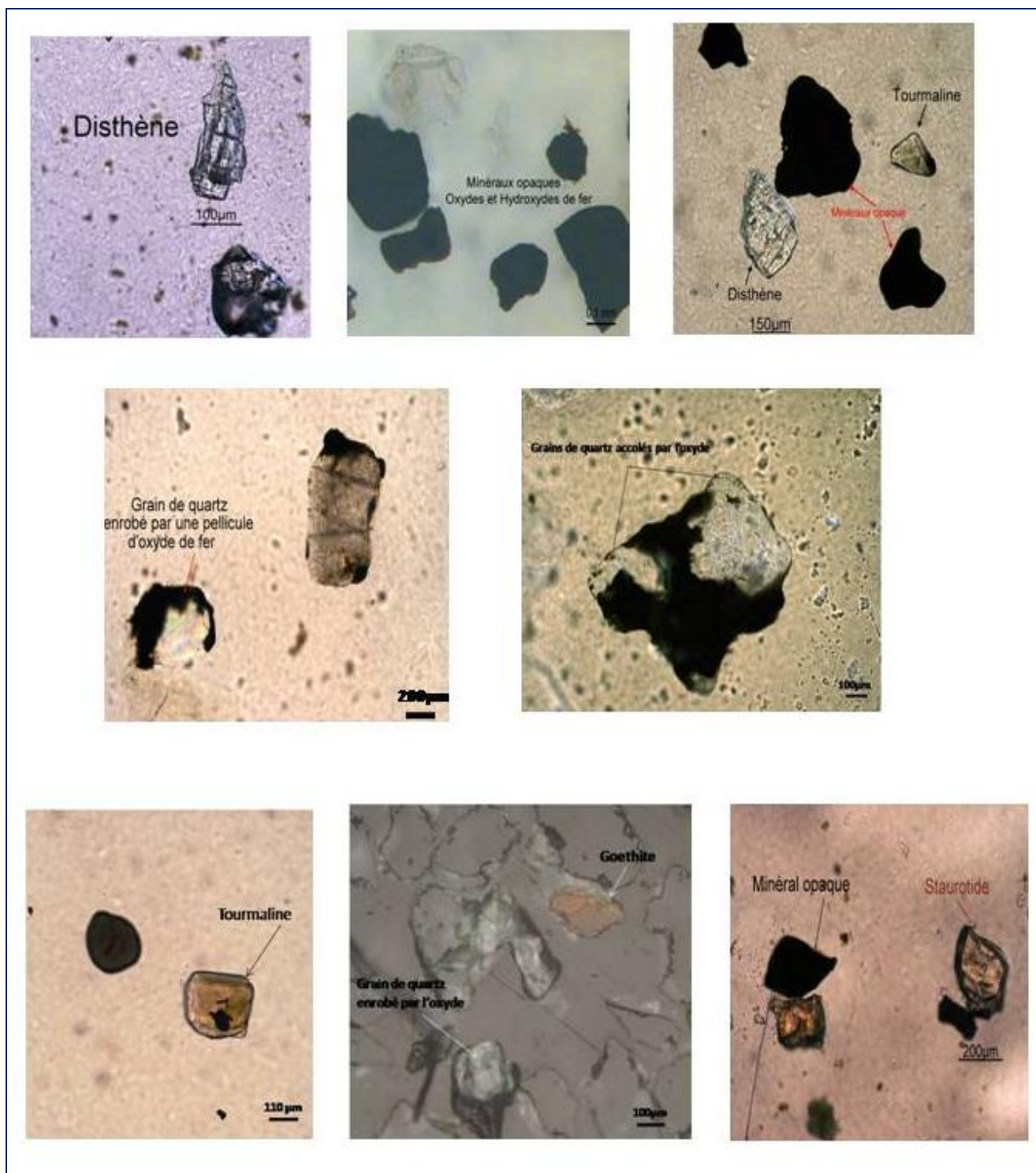


Plate 2 : Mineralogical identification of the dense fraction of Fortuna sand from Ain Bou Morra

4.2.3 Physical treatments

The raw fraction (-0.63+0.1mm) is suitable for the manufacture of flat glass and other types of white glass. However, to make high-grade silica sand an additional

physical treatment is necessary comprising the following successive stages:

The first schema contains the size classification before and after attrition followed by a dry magnetic separation attrition and electrostatic separation. The results of the final product are (Table 2):

Table 2 : results of chemical analysis of the final product after treatment by attrition and dry magnetic separation

Sample	SiO ₂ %	Al ₂ O ₃ %	CaO %	Fe ₂ O ₃ %	K ₂ O %	MgO %	Na ₂ O %	TiO ₂ %	Cr (ppm)	Cu (ppm)
Sample 1	99.51	0.14	0.03	0.031	0.11	0.0072	0.013	0.01	nd	nd
Sample 2	99.39	0.12	0.05	0.029	0.10	0.0061	0.012	0.012	nd	nd
Sample 3	99.36	0.11	0.026	0.022	0.09	0.0073	0.015	0.01	nd	nd

nd: not detected

For the three studied samples, the purified fraction after attrition and dry magnetic separation is the available size fraction between 0.1et 0.63mm.

Purified samples show silica content of 99.36%.

The contents of the most harmful impurities decreased after treatment and may have an iron content between 0.02 and 0.031%, a content of 0.11 to 0.14% for alumina, a content of 0.01 % of titanium; chromium being not detected.

The second scheme includes more gravity separation, between the attrition operation and wet high intensity magnetic separation (WHIMS) and followed by electrostatic separation.

To reach the requirements of high-quality sand industry, the sand should be further purified with silica grains devoid of other minerals or any contaminants. The final product must include a total contaminant level <10 ppm (Outotec, 2007). In order to reach this specification the high voltage electrostatic separation was applied.

Practically, the separator with different voltage value is used. The results are given in table 3.

Table 3 : Variation of% weight and the% of Fe2O3 of the fraction non-conductive fraction

VOLTAGE KV	% Weight of non-conductive fraction	% Fe2O3
10	42	0.028
15	72	0.019
20	87	0.003
28	99	0.0009
30	82	0.007

Table 4 : distribution of weight and the% of Fe2O3 according to the fraction not conductive voltage variation (%)

VOLTAGE KV	% Weight of non-conductive fraction	% Fe2O3
10	40	0,03
15	71	0,025
20	89	0,0028
28	98	0,0001
30	79	0,0025

Table 5 : distribution of weight and the% of Fe2O3 according to the fraction not conductive voltage variation (%)

VOLTAGE KV	% Weight of non-conductive fraction	% Fe2O3
10	37	0,029
15	66	0,023
20	81	0,004
28	94	0,0001
30	80	0,002

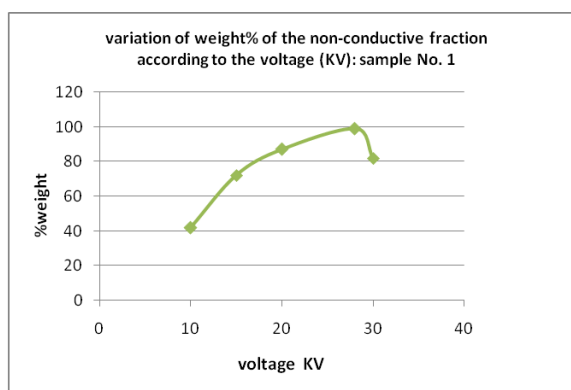


Figure 9. Curve of variation of the weight% of the non-conductive portion in function of the voltage (kV): case of the average sample Aml.

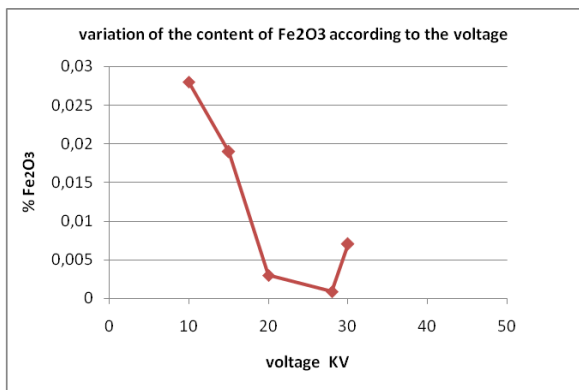


Figure 10. Variation curve of the Fe₂O₃ content in function of the voltage (kV) If the average sample AM1.

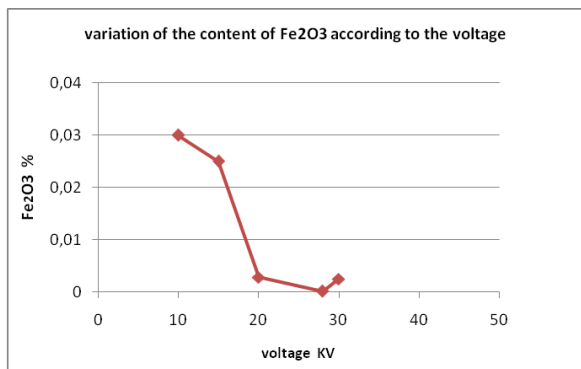


Figure 12. Variation curve of the Fe₂O₃ content in function of the voltage (kV) If the average sample AM2.

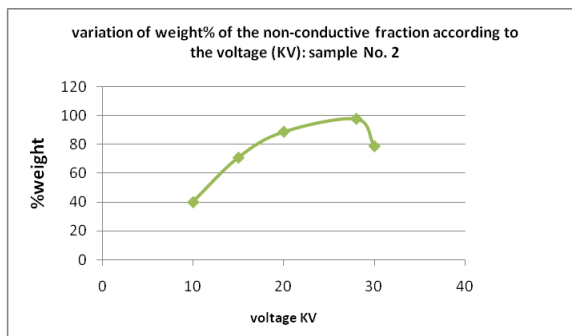


Figure 11. Curve of variation of the weight% of the non-conductive portion in function of the voltage (kV): case of the average sample AM2.

The best yield weight is obtained with 28 kilovolts. If the voltage exceed this threshold the result becomes less efficient.

Indeed, by applying a voltage higher than 28 kilovolts a double failure is present: firstly the manifestation of a very intense electrical discharge and secondly the substantial decrease of the weight of non-conductive fraction yield (Example AM1 sample the% weight decreases from 99 to 82%). The voltage of 28 kilovolts is the ideal voltage for efficient separation while maintaining the other parameters constant. The results of chemical analyses of the non-conductive fraction are represented in table 6.

Table 6 : Results of chemical analyses of the final product after attrition treatment, gravity separation, wet high intensity magnetic separation and electrostatic separation.

Sample	SiO ₂ %	Al ₂ O ₃ %	CaO %	Fe ₂ O ₃ %	K ₂ O %	MgO %	Na ₂ O %	TiO ₂ %	Cr (ppm)	Cu (ppm)
Sample 1	99.99	0.008	0.005	0.0009	0.009	0.002	0.003	0.001	nd	nd
Sample 2	99.97	0.01	0.009	0.0010	0.009	0.004	0.003	0.002	nd	nd
Sample 3	99.94	0.03	0.011	0.0013	0.01	0.003	0.004	0.004	nd	nd

nd: not detected

It is shown that the depletion of iron oxide (0.0009% Fe₂O₃) and titanium oxide (0.001 %TiO₂) in the non conductive fractions (Table 6) was successfully conducted.

This proves that the adopted treatment approach decrease the potential of contamination for the final product of quartz sand. Therefore, the obtained product could be used in high technology industries such as the manufacture of silicon for photovoltaic cells manufacture, optical fibers and electronic chip.

This type of testing has also been undertaken with only attrition of sands. The beneficiation of the sand is less effective.

These induce that gravity and wet magnetic separation and electrostatic separation, were needed to make an efficient recovery process.

The processing steps are illustrated in summarized flow-sheet.

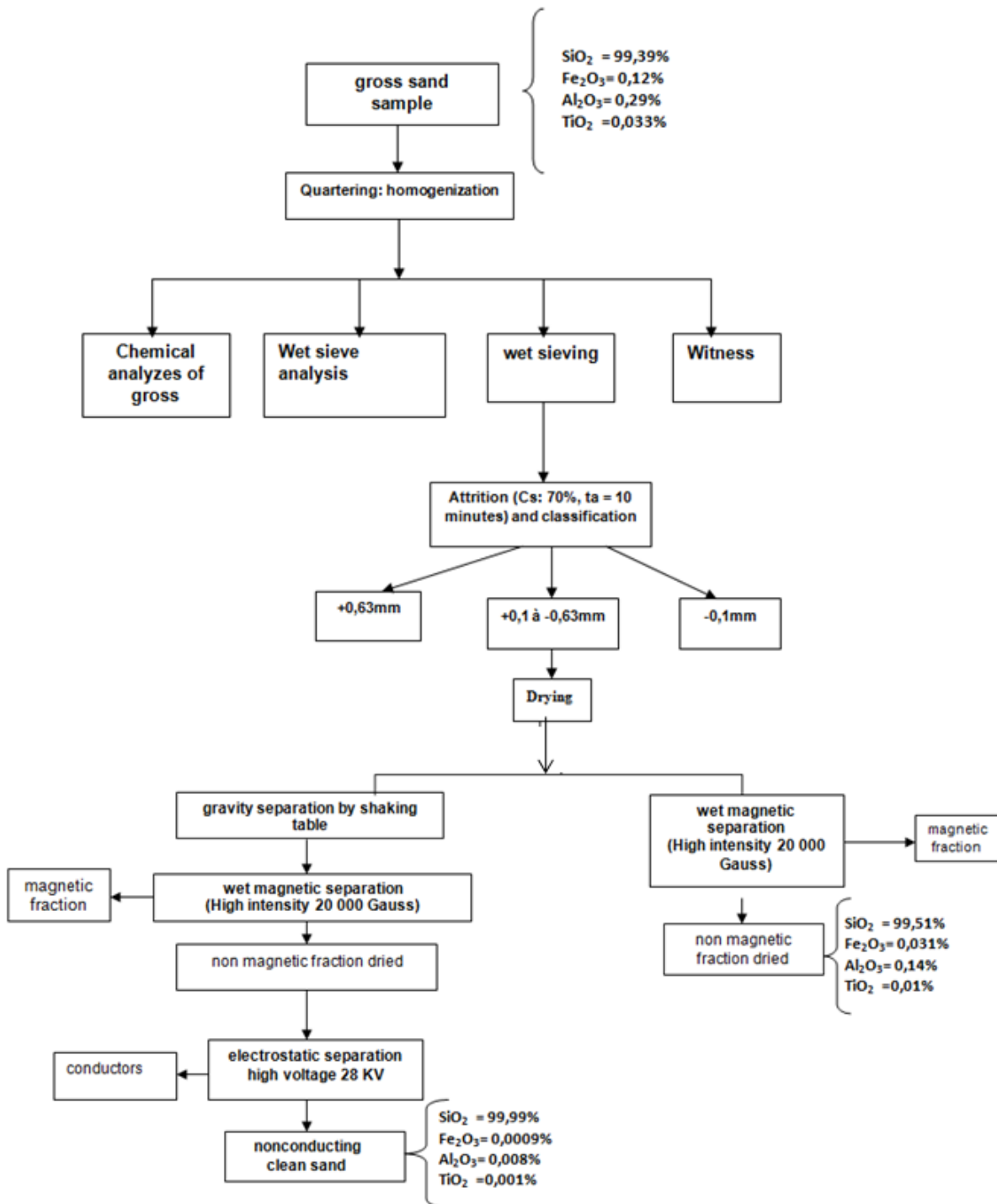


Figure 13: Flowsheet of the two presented schemes

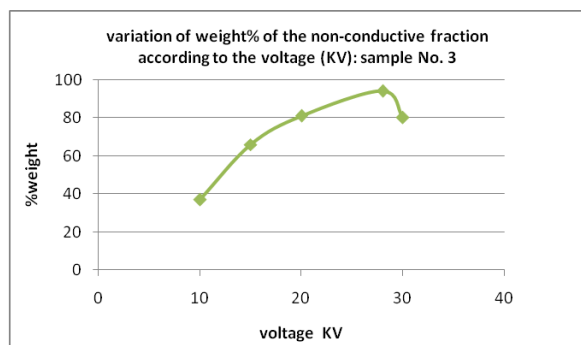


Figure 4 Curve of variation of the weight% of the non-conductive portion in function of the voltage (kV): case of the average sample Am3

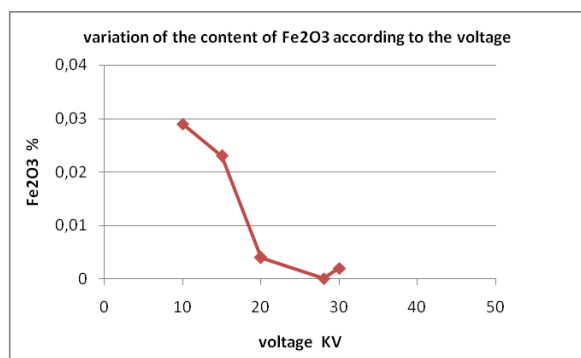


Figure 5. Variation curve of the Fe2O3 content in function of the voltage (kV) If the average sample AM3.

Conclusion

Mineralogical and chemical studies carried out on silica sand samples from Ain Bou Morra area shows that the main impurities are iron, titanium and feldspar minerals. Most of the impurities are distributed in the finer fraction (flat glass, optical glass, glass white, half white glass, glass wool and glass brick) and also for the chemical industry (silicate manufacturing soda).

While under the second scheme, prepared sands can be used even for the manufacture of crystal glass as raw material for silicon production which is the main element used for the manufacture of photovoltaic solar cells and electronic chips.

Acknowledgments

The authors would like to express their sincere thanks to Stoyan Gaydardzhiev, associate Professor, at the University of Liege for access to laboratory and collaboration in microscopic analysis. We also acknowledge David Bastin for his assistance in the physical and chemical analysis.

References

- Added M., 2005. Impact de la qualité des granulats sur les caractéristiques physico-mécaniques des mortiers et des bétons. Thèse Doc. Univ. Tunis El Manar. Faculté des Sciences de Tunis.175p.
- Aloui T., 2010. Etude sédimentologique et intérêt économique des sables d'âge barrémien (formation Sidi Aich) Tunisie Centro-méridionale. Thèse Doc. Univ. Tunis II, Tunisie. 287p.
- Ben Fradj M., 2010. Etude minéralogique, chimique et minéralurgique des sables de Menzel Mhiri et de Ain Bou Morra. Mémoire de Mastère. Univ. Tunis El Manar. Faculté des Sciences de Tunis. 131p.
- Ben Haj Ali, M., Jedoui, Y., Ben Salem, H., Memmi, L., 1985. Carte géologique de la Tunisie : 1/500 000. Office National des Mines, Service Géologique.
- Gaied M.S., 1991. Géologie des matériaux utiles de la région d'El Gnater (Tunisie Centrale). Mémoire de DEA. Univ. Tunis El Manar. Faculté des Sciences de Tunis. 118p.
- Gaied M. E, Gallala W., 2011. Beneficiation of feldspar ore for application in the ceramic industry: Influence of composition on the physical characteristics. Arabian Journal of Chemistry, V.8, 2, p186-190.
- Gallala, W. (2010). Les sables quartzofeldspathiques de la Tunisie centro-méridionale: sédimentologie, minéralogie, minéralurgie et applications industrielles, PhD Thesis, Faculty of Sciences Sfax, Tunisia.
- Gallala W, Gaied M. E., Montacer M., 2009. Concentration of Potassium Feldspar from Low-grade Sidi Aïch Sand in Tunisia for Industrial Applications. Silicates industriels, no 5-6, p. 125-130.
- Griffiths J., 1987. Silica. Is the choice crystal clear. Industrial Minerals, n° 235. Pp 25-43.

- El Maaoui M., 1993. Chimie pratique du verre. Rapport, CTMCCV.
- Harben, Peter W., Kužvart, M., 1997. Industrial minerals: a global geology. Metal Bulletin.
- Jamoussi F., 1991. Etude géologique et géotechnique des substances minérales utiles de la région de Gafsa. Thèse de spécialité. Faculté des Sciences de Tunis. 298p.
- Jouirou M., 1981. Etude géologique et géochimique des sédiments de la région d'El Kef (NW de la Tunisie). Thèse Doc. Univ. de Bordeaux. 146p.
- Louhaichi M.L., 1981. Etude géologique et géotechnique de la partie nord-occidentale du gouvernorat de Kairouan (Tunisie) application à la recherche et à la cartographie des matériaux utiles. Thèse Doc. Univ. Franche-Comté. Faculté des sciences et des techniques. 146p.
- Ounis M.S., 2004. Contribution à l'étude du sable Oligocène de Oueslatia application aux domaines de l'industrie. Diplôme de mastère en géologie, Faculté des sciences de Tunis. 67p.
- Trabelsi, H., 1989. Les matériaux utiles de la région de Feriana (Tunisie centrale) (cadre géologique et potentialités). Thèse de doctorat, Nice.